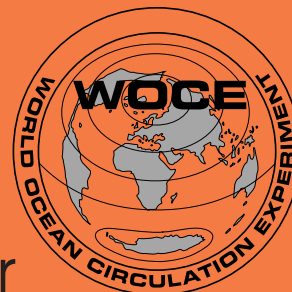


# International **WOCE** Newsletter



Number 29

December 1997

## IN THIS ISSUE

### ❑ News from the IPO

- The Conference Approaches *W. John Gould and Roberta Boscolo* 2

### ❑ Southern Ocean

- Two-Year Long Current Time Series from the Southwest Indian Ocean *Raymond Pollard and Jane Read* 3

- Deep Inflow into the Mozambique Basin *J. F. Read and R. T. Pollard* 7

- Tracer Studies in the Southern South Atlantic Within WOCE *Christine R  th, et al.* 11

- Hydrography and Baroclinic Transport between Africa and Antarctica on WHP Section I6 *Young-Hyang Park and Edwige Charriaud* 13

- Repeated Observations of the ACC on WOCE SR1b *Marc A. Garcia et al.* 16

- High Resolution XBT/XCTD Measurements Across Drake Passage *Janet Sprintall, et al.* 18

- What Drives Mid-Latitude Convection and the Formation of Subantarctic Mode Water? *Joachim Ribbe* 20

- On the Climatic Variability of Deep Waters in the Pacific Antarctic *Alexander Yu. Goldin, and Mikhail N. Koshlyakov* 27

- Subantarctic Mode Water Formation by Air-Sea Fluxes *Kevin Speer, et al.* 29

- The Sub-Antarctic Flux and Dynamics Experiment (SAFDE) *Douglas S. Luther and the SAFDE Pls* 32

- Estimates of Diapycnal Mixing Using LADCP and CTD data from I8S *Kurt L. Polzin and Eric Firing* 39

- Norwegian Physical Oceanographic Activities in the Weddell Sea *Ole Anders N  st* 42

### ❑ Miscellaneous

- WOCE Helps to Assess the Quality of Historical Hydrographic Data: A New Validated Data Set for the Southern Hemisphere *Victor Gouretski and Kai Jancke* 35

- Surface Flux Climatology (Version 1.1) available at SOC 10

- Errata (C. Andri   et al. article in WOCE Newsletter No. 28) 10

- Global Directory of Marine Science Institutions and Scientists (GLODIR) 19

- Adjoint Model Compiler 31

## The Conference Approaches

*W. John Gould and Roberta Boscolo, WOCE IPO*

With October's Newsletter we mailed the WOCE Conference Announcement and since then the IPO and many other people particularly in Canada have been busy with Conference preparations. After a few teething problems the appropriate WWW sites for registration and abstract submission are operating successfully. The abstract deadline of 15 December is rapidly approaching so please make sure that we hear about YOUR science! We are hoping for an avalanche of submissions. I visited the Conference venue in Halifax in October: it is impressive and Halifax will be a very pleasant and convenient location.

### The WOCE SSG

The SSG held its 25th meeting at the end of September at NCAR, Boulder Colorado USA – in the foothills of the Rockies. It was the first time I had visited there and I was struck by its spectacular and beautiful location.

Our meeting was very productive and in particular we had the benefit of NCAR being Kevin Trenberth's (CLIVAR SSG Co-Chair) home laboratory. Some considerable time was spent discussing issues of interest to both WOCE and CLIVAR. The projects will co-sponsor the August 1998 workshop on Ocean Modelling and WOCE will be re-submitting to the CLIVAR SSG an outline of key ocean observations that we believe need to be maintained.

The SSG also confirmed the N. Atlantic Workshop for Kiel, Germany in August 1999. Workshops will be a key element of the AIMS phase and the SSG set in motion the planning for new ones in the areas of "The use of tracers", "The representativeness of the WOCE data set" and "Ocean data assimilation". This last topic had been identified by the Synthesis and Modelling Working Group. Since the SSG meeting, discussions have been carried out with a number of other groups interested in Data Assimilation to try to avoid duplication. An announcement of the scope, location and time of the Assimilation meeting will be made shortly.

The SSG has further considered WOCE's oversight and concluded that, following the publication (in December) of the "WOCE AIMS Strategy Document", the SMWG should disband and its responsibilities be shared between a somewhat-expanded SSG and the ad-hoc workshop committees. Similarly the Hydrographic Programme Planning Committee held its last meeting this October and will now be subsumed into the Data Products Committee.

This "slimming down" in no way reflects a reduction

in WOCE activity and indeed the number of papers being submitted to the Newsletter is indicative of how many new and exciting results are being produced and shared.

### A summary of WOCE observations

Last year we published a WOCE Data Guide 1997. It was very well received and has been much used. Now that observations have ended, the IPO together with the DIU will be assembling a comprehensive document (primarily electronic) that will summarise – What observations were made in WOCE? Where? and By whom? We expect that this will become a standard WOCE reference document and thus we will work hard to make sure that it will be comprehensive and, above all, accurate. What this means is that we will probably be contacting many people over the next few months to ensure that the information we have is correct.

### From the editor

This is the fifth WOCE Newsletter of this year, and I would like to thank all the contributors for their collaboration. This has been an exceptional year for the number of issues produced, each of them full of good scientific articles and remarkable research. It would not have been possible without the co-operation of the authors and their enthusiasm gave great pleasure to me.

I thank all of you who I approached and invited to write an article as well as everyone who spontaneously chose to publish their preliminary results in the Newsletter. The number of scientists who offer to submit their articles to us is increasing and this is a sign that WOCE science is now, more than before, delivering answers to the questions posed at the beginning of WOCE project. This has been a great source of encouragement for me.

Next year we are planning to produce four issues. The schedule and theme for each issue will be roughly as follows:

Issue	Publication	Submission Deadline	Theme
30	February	15 December '97	Instrumentation
31	May	1 March '98	General science
32	August	1 June '98	Modelling
33	November	1 September '98	Indian Ocean

# Two-Year Long Current Time Series from the Southwest Indian Ocean

Raymond Pollard and Jane Read, George Deacon Division, Southampton Oceanography Centre, UK. [raymond.pollard@soc.soton.ac.uk](mailto:raymond.pollard@soc.soton.ac.uk)



A line of moorings was deployed between the Agulhas Plateau and the Crozet Islands (Fig. 1, page 21) as part of SWINDEX (SouthWest INdian ocean EXperiment), a UK contribution to WOCE Indian Ocean Special Survey area 1 (ISS1). Five moorings (A, B, D, F and G) were recovered after a 21 month deployment (April 1993 to January 1995). There were several reasons for choosing this line. It spans the southern entrance to the Mozambique Basin, which is closed to the north below 3000 m. We wished to quantify the deep, presumably near-zero, inflow of bottom water from the south. The mooring line spans the region where large scale dynamic topography (e.g. Gordon et al., 1978) shows streamlines from the ACC tending to turn northeast and cross the Del Caño Rise, and we wished to refine this picture. Finally, all the moorings were set in the low eddy energy region between the Agulhas Return Current to the north and the ACC to the south. We shall consider each of these three aspects in this article. As an introduction to the data, mean and eddy kinetic energies (EKE) for the 16 current meters are given in Table 1. EKE values were indeed low, no higher than  $50 \text{ cm}^2 \text{ s}^{-2}$ , but there is an interesting increase in EKE in deep trenches, which we describe first. Then we quantify the deep flow into the Mozambique Basin, and finally the ACC transport across the Del Caño Rise.

## Enhanced abyssal energy

Three of the moorings were set in channels or deep trenches between ocean basins. Mooring G was in the 5900 m deep trench connecting the Agulhas and Mozambique Basins. Mooring F was in the Prince Edward Fracture, which joins the Enderby Basin directly to the Mozambique Basin. Mooring A was in the relatively wide, 3000 m deep gap between the Crozet Islands and the Del Caño Rise. At all three moorings, the bottom current meter, 90 m off the bottom, had significantly higher EKE than current meters at mid-depth. The difference is most striking at the two deep moorings F and G (Fig. 2), where the mid-depth spectra are about ten times less energetic (Fig. 2a) than the bottom spectra for periodicities between about 2 to 20 days.

Rudnick (1997) has suggested that internal resonance in channels, similar to organ pipe waves, could be the cause of bottom enhanced energies. In our case, the density jump across the stratified zone above the bottom boundary layer lies in the range  $0.05 - 0.1 \text{ kg m}^{-3}$  and the height of the boundary layer lies between about 200 and 1000 m. Thus the phase speed of shallow water waves is  $0.3 - 1.0 \text{ m s}^{-1}$ . Resonance occurs at a frequency for which the length of a channel (closed at one end) is one quarter wavelength, which gives a range of possible channel lengths from 13 km (2 day period,  $0.3 \text{ m s}^{-1}$  phase speed) to 430 km (20 day

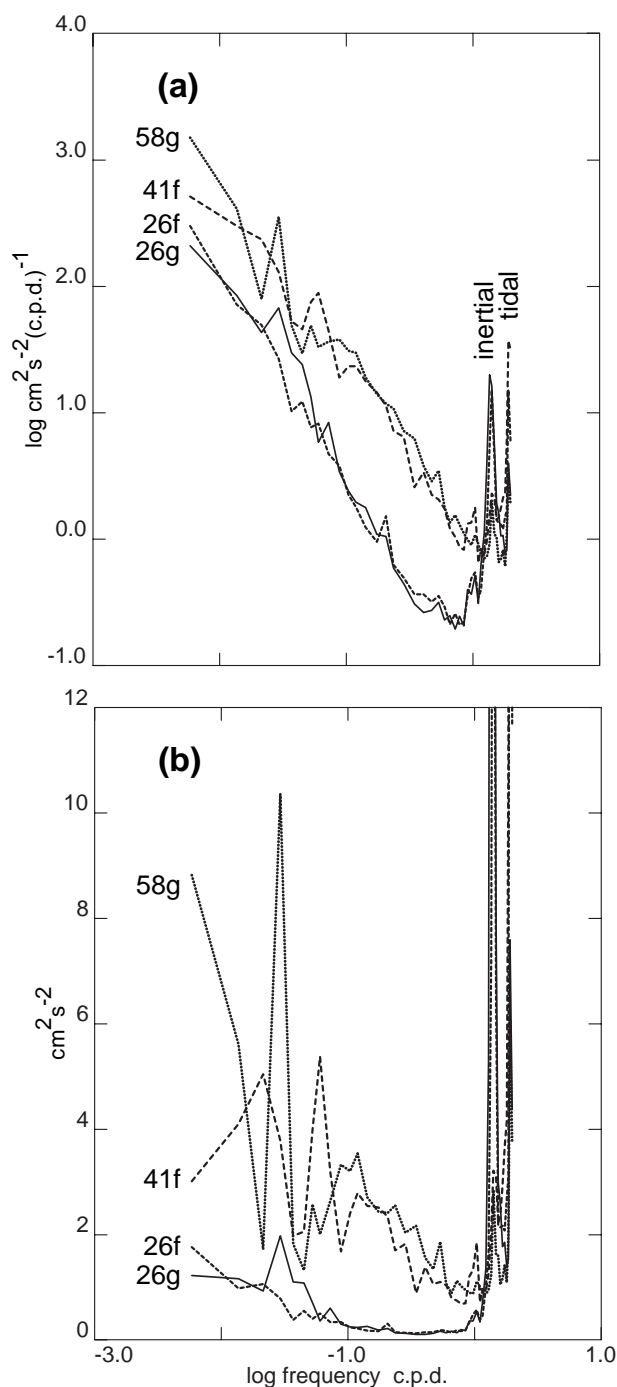


Figure 2. Spectra from the two deepest current meters on each of moorings F and G are shown in (a) log-log and (b) log-linear (energy proportional to area) form. Numbers give the instrument depths in hundreds of metres. The Nyquist frequency is 2 cycles per day (c.p.d.), just large enough to prevent aliasing of the 12.42 hour tide.

period,  $1.0 \text{ m s}^{-1}$  phase speed). This range is plausible, as there may well be local constrictions in the channels on 10–20 km scales, and the Prince Edward Fracture extends from about 43–48°S, over 500 km.

The importance of the bottom enhanced EKE may be its role in mixing. Our hydrographic data (Read and Pollard, this issue) show evidence of strong mixing. Enhanced mixing near rough topography is beginning to be well documented (e.g. Toole et al., 1994) but the prime candidate contributing to the small-scale shear field is considered to be internal tides. While tides are present in our data at all depths, they are not the major contributor to abyssal energies (Fig. 2b). The SWINDEX data indicate that in some instances low frequencies including the mean are sufficient to drive mixing. Indeed, if we estimate shear by taking the one-day mean speeds 90 m off the bottom and linearly decreasing them to zero at the bottom, and then calculate a Richardson number using the stratification from the CTD casts, the Richardson number is frequently less than critical. Thus we expect at least the bottom 100 m to be fully turbulent much of the time in the two deep trenches.

## Deep flow into the Mozambique Basin

The Mozambique Basin (Fig. 1) is bounded to the west by South Africa and the Mozambique Ridge and to the east by the Madagascar and Southwest Indian Ridges. The deepest point to the east is that at the intersection of the two ridges, at about 36°S, 45°E, where the depth reaches about 3400 m, as confirmed by the survey in February 1995. North of this saddle the ridge rises up towards the island of Madagascar. To the south the ridge is broken by various gaps but nowhere does the ridge allow any through flow deeper than about 3000 m. North of the Mozambique Basin is a relatively shallow channel between Africa and Madagascar with a depth of only 2500 m in places. Thus the only entrance to the Mozambique Basin deeper than 3000 m is along the southern boundary (which is over 5000 m deep in places). Mooring G was sited in the deep trench between the Agulhas and Mozambique Basins.

For bottom water from the Weddell Gyre to reach the Mozambique Basin, it has to cross the Southwest Indian Ridge, the lowest point of which lies around 50°S just west of the Del Caño Rise. The deep trenches which fracture this Ridge are poorly resolved even by modern bathymetric data sets, so Fig. 1 shows the “predicted topography” developed by Smith and Sandwell (1994; 1997) from Geosat

and ERS-1 gravity anomalies constrained by ship soundings. The resolution of their data provides a much more detailed picture of the topography than previously available. In particular, trenches that were assumed to be blocked in interpolated data sets are open below 4000 m in the higher resolution data set.

Only two paths are available for bottom water to travel from the Enderby Basin to the Mozambique Basin. One goes via the gap in the Southwest Indian Ridge at 50°S, 30°E into the Agulhas Basin and thence via the trench past Mooring G to the Mozambique Basin. The second path is via the easternmost trench, the Prince Edward Fracture Zone (PEFZ), which is open below 4000 m and extends directly into the southern end of the Mozambique Basin. The PEFZ is shown to be blocked by conventional published bathymetry, but we surveyed the supposedly shallow area during mooring recovery and found the trench to be 4200 m deep and 11 km wide at that point, confirming the predicted topography of Fig. 1. Mooring F was set at the northern end of the PEFZ in a depth of 4262 m.

Progressive vector diagrams from the current meter located 90 m off the bottom in each trench are shown in Figs. 3a and 3b. Record 58g, at 5812 m depth, shows northward flow with a remarkably large, 21 month mean speed of  $12 \text{ cm s}^{-1}$ . The actual speed varied from 0–20  $\text{cm s}^{-1}$  but the direction of flow was constant along

*Table 1. Mean and Eddy Kinetic Energy and summary statistics*

Data name	Depth (m)	Eddy KE ( $\text{cm}^2/\text{s}^2$ )	Mean KE ( $\text{cm}^2/\text{s}^2$ )	mean speed (cm/s)	mean direction degrees	good data duration days
<b>Mooring A</b>	<b>2864</b>					
acmsw03a	330	53	202	20	-15	434
acmsw05a	533	31	157	18	-16	270
acmsw06a	634	39	185	19	-17	655
acmsw13a	1360	10	77	13	-6	655
acmsw22a	2223	12	78	13	-13	655
acmsw28a	2818	27	41	*9	-23	655
<b>Mooring B</b>	<b>1614</b>					
acmsw03b	311	29	13	5	-61	618
acmsw06b	612	22	11	5	-74	657
<b>Mooring D</b>	<b>2710</b>					
acmsw03d	335	14	1	1	-58	657
acmsw13d	1364	4	4	3	-83	658
<b>Mooring F</b>	<b>4262</b>					
acmsw06f	382	14	11	5	94	657
acmsw13f	1391	5	1	1	102	657
acmsw26f	2661	6	0	1	150	657
acmsw41f	4174	18	4	3	14	657
<b>Mooring G</b>	<b>5900</b>					
acmsw26g	2681	6	2	2	16	657
acmsw58g	5812	22	69	12	31	657
*This value is low because of rotor dropouts.						

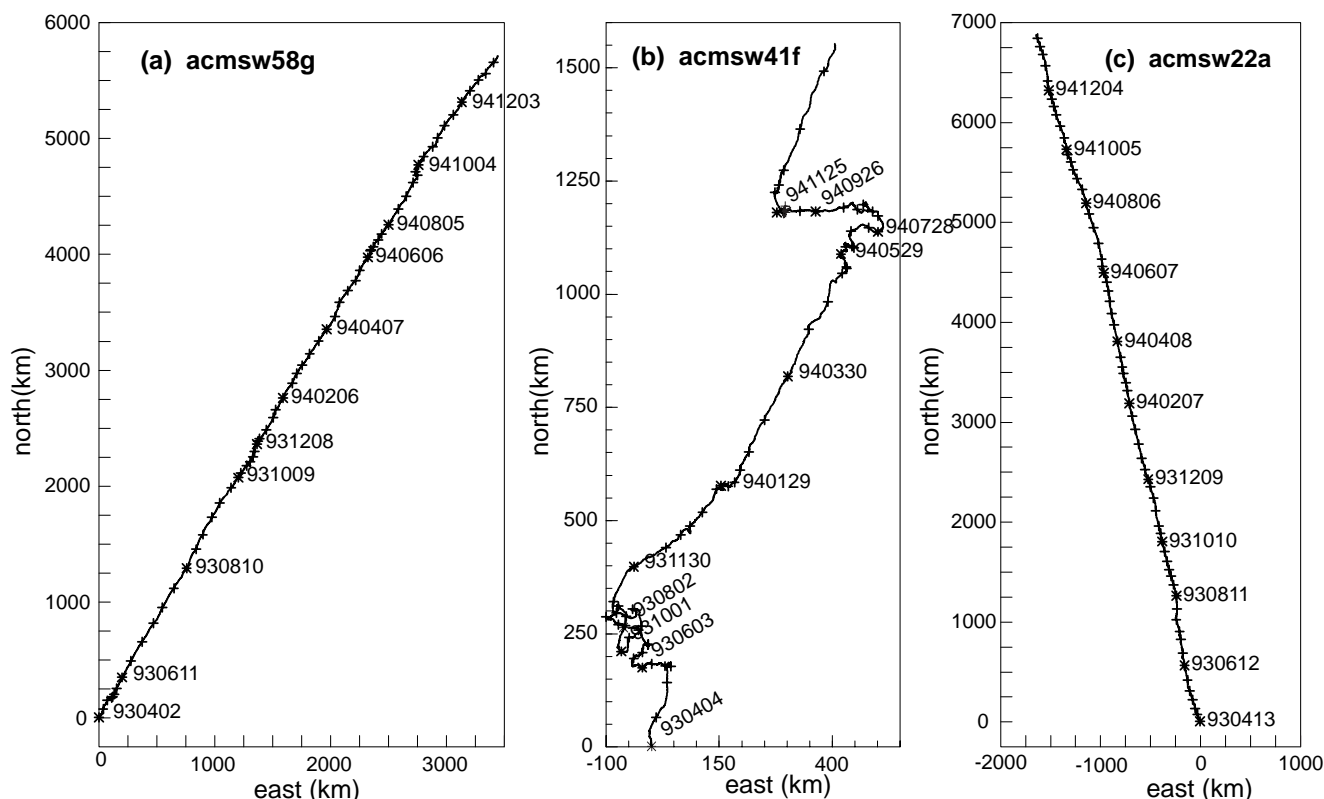


Figure 3. Progressive vector diagrams for deep current meters from moorings G, F and A. Crosses are marked every 10 days and the date (YYMMDD) is added every 60 days. Note the different scales for each sub-figure.

the axis of the trench. This record confirms the deep, bottom intensified inflow inferred by Read and Pollard (this issue) from which they calculated 1 Sv inflow of bottom water.

The mean current at 41f (Fig. 3b) was  $2.8 \text{ cm s}^{-1}$  northward. Speeds varied between  $0 - 20 \text{ cm s}^{-1}$  but with a tendency for westwards movement when the speeds were very low. The record begins with a period of northward flow which dies away within a few weeks of deployment at the end of April 1993. A second burst of northward flow begins in November 1993 and continues until early May 1994, and a third period of northward flow begins in November 1994. This is suggestive of annual inflow during the Austral summer. Taking the mean depth of the Fracture as 4230 m with a width of 12.2 km, we can estimate the northward transport of the layer of bottom water below 4000 m. For the 21 month mean, the transport is only 0.08 Sv, but this rises to 0.3 Sv or more during periods of a month or more during which the mean flow is greater than  $10 \text{ cm s}^{-1}$ . This transport is not taken into account by Read and Pollard (this issue), and will act to increase their estimates of upwelling velocities.

### ACC transport west of Crozet

Dynamic topography from observations and models (Gordon et al., 1978; Park and Gamberoni, 1995) shows the ACC crossing  $30^\circ\text{E}$  south of  $45^\circ\text{S}$ , with several streamlines then turning northeast or north to cross the Del Caño Rise.

At  $33^\circ\text{E}$ , Read and Pollard (1993) found much of the transport of the ACC (138 Sv) concentrated at and south of the Polar Front at  $48^\circ\text{S}$   $33^\circ\text{E}$ . Thus one of the objectives of SWINDEX was to quantify how and where the ACC crosses the topographic barrier of the Del Caño Rise.

The moorings A, B, D and F span the Del Caño Rise, though unfortunately other moorings were lost. Comparing the mean flows given in Table 1 with the bathymetry (Fig. 1), one's impression is that the upper layer flows split to pass round the Del Caño Rise to the west (F) and east (A and B), following the bathymetry (B) and avoiding the centre of the Rise (D). A significant branch of the ACC appears to flow north between the Del Caño Rise and Crozet (A). The hydrographic data confirm this assessment. Perhaps 20 Sv is turned north by the Southwest Indian Ridge, flowing along the line of the PEFZ towards Mooring F. The majority of the transport (80–90 Sv) continues eastwards in a broad flow south of the Del Caño Rise.

It is of interest to quantify the volume and nature of the transport which flows north to the west of Crozet. This we can do by combining the mooring data at A with the hydrographic survey in 1993 and the repeat section in 1995. The current meters show a strong barotropic (Table 1), persistent (Fig. 3c) flow. The current speeds and directions vary little with depth throughout the water column (Table 1), so we have calculated a depth-averaged mean speed by interpolating between adjacent current meters with constant extrapolation at the top and bottom. The resulting depth



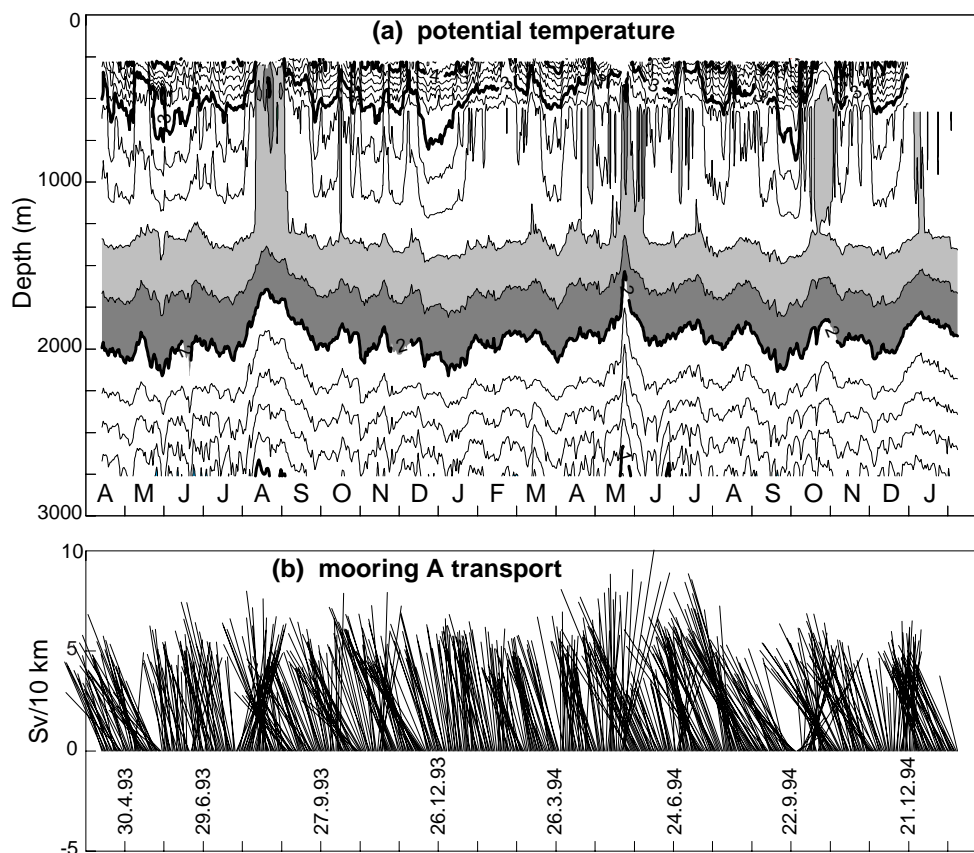


Figure 4. A thermistor chain between 332–432 m and current meters between 330 and 2818 m (Table 1) have been used to derive (a) contours of potential temperature against time and depth, (b) vertically integrated transport, shown as Sv through a section 10 km wide. Contours are 0.2°C apart in (a), with integer degrees shown bold. Exact dates are shown on (b), approximate months on (a).

averaged mean speed is  $14.9 \pm 3.5 \text{ cm s}^{-1}$ , where  $3.5 \text{ cm s}^{-1}$  is the standard deviation of daily means. Corresponding transports for a 10 km wide section are  $4.3 \pm 1.0 \text{ Sv}$ , shown as daily means in Fig. 4b.

To obtain an estimate of total transport, the barotropic and baroclinic components were investigated separately. The baroclinic flow is defined by taking the level of no motion as the deepest common level between each pair of CTD casts. West to east hydrographic sections in both 1993 and 1995 each show a broad band of northward flow (Table 2), transporting about 15 Sv, and extending 60 km east and 60 to 140 km west of A, as far as Mooring B in 1995.

The width of the barotropic current was estimated by comparing the hydrographic sections with the moored potential temperature contour plot (Fig. 4a). In the gap west of Crozet, isotherms rise from west to east by several hundred metres, with the 2.4°C and warmer isotherms rising dramatically about 30 km east of the mooring and descending to about 1350–1400 m 10 km west of A. These depth changes are clearly seen in the thermistor data. Thus strong barotropic currents are seen at all times

as the front shifts from east to west past the mooring. We infer that the current is at least 40, possibly 70 km wide, confined to the western side of the gap west of Crozet and much narrower than the region of baroclinic flow.

Minimum and maximum barotropic transports were calculated using these widths and bottom currents of 13 and  $11 \text{ cm s}^{-1}$  respectively (Table 2). The  $13 \text{ cm s}^{-1}$  bottom current is taken from 13a and 22a (Table 1). The  $11 \text{ cm s}^{-1}$  bottom current was chosen to bring the baroclinic transport density (1.1 Sv/10 km) more closely in line with the hydrographic estimates. Combining the barotropic (13–26 Sv) and baroclinic (15 Sv) transports, we obtain 28–41 Sv total transport. Note that the baroclinic transports bracketed in Table 2 for Mooring A are only for the restricted widths of the barotropic calculation.

Read and Pollard (1993) calculated 150 Sv transport in the Subantarctic and Polar Frontal Zones at 33°E relative to deep bottom reference levels. We have estimated 20 Sv turning northwards along the PEFZ west of Marion Island and a further 25–40 Sv west of Crozet. In the latter case, in water depths of only 3000 m, there is a significant barotropic component. Thus we can account for 30–40% of the ACC transport crossing from south to north of the Del Caño Rise west of Crozet Island. The majority of the ACC transport

Table 2. Transport between Crozet and Del Caño Rise

	Width (Km)	Baroclinic Transport (Sv)	Barotropic Transport (Sv)	Baroclinic Transport (Sv/10 km)
<b>From CTDs</b>				
1993	118m	14.6v		1.2
1995	197m	15.7		0.8
<b>From mooring A</b>				
Max ( $u_B = 13 \text{ cm/s}$ )*	70	(4.2)	25.9v	0.6
Min ( $u_B = 11 \text{ cm/s}$ )*	40m	(4.4)	12.8	1.1
* $u_B$ is the bottom velocity used to calculate the barotropic transport				

does not shift north nor combine with the Agulhas Return Current until east of Crozet, at 50°E.

Finally, what is the front just east of Mooring A, that crosses the mooring position several times? In August 1993 (Fig. 4a) a subsurface potential temperature minimum just less than 2°C can just be seen at about 400 m. In May 1994, the same temperature minimum was reached, with exceptionally strong currents causing mooring knockdown to 400 m (from the varying depth of the shallowest temperature contours in Fig. 4a). On several other occasions the 2.4°C contour shallows to the 600 m current meter. The 2°C temperature minimum is rather too deep for this to be considered the Polar Front, nor are the frontal characteristics right for the Subantarctic Front. Nevertheless, there is clearly a significant (25–40 Sv) branch of the ACC permanently passing through the gap between Crozet and the Del Caño Rise.

## Deep Inflow into the Mozambique Basin

*J. F. Read and R. T. Pollard, George Deacon Division, Southampton Oceanography Centre, UK. jane.read@soc.soton.ac.uk*

The spread of cold bottom water out of the Southern Ocean is, in general terms, well documented (e.g., Mantyla and Reid, 1983, 1995). But many of the specific details remain elusive. Mantyla and Reid (1983) describe abrupt changes from one basin to the next and comment that the changes must be due to “continuous vertical mixing along the path northward with successive warmer and more saline overlying water”. But there are few, if any, published observations or descriptions of this process taking place.

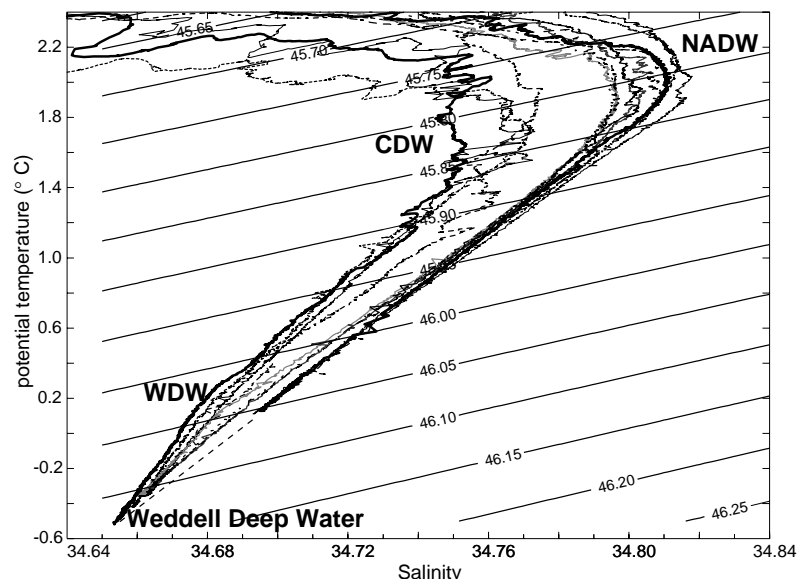
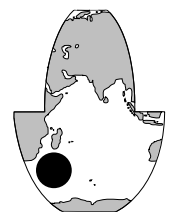


Figure 1. Potential temperature and salinity from the Prince Edward Fracture, with density referenced to 4000 m. NADW - North Atlantic Deep Water, CDW - Circumpolar Deep Water, WDW - Warm Deep Water.

## References

- Gordon, A. L., E. Molinelli, and T. Baker, 1978: Large-scale relative dynamic topography of the Southern Ocean. *J. Geophys. Res.*, 83, 3023–3032.
- Park, Y.-H., and L. Gamberoni, 1995: Large-scale circulation and its variability in the south Indian Ocean from TOPEX/POSEIDON altimetry. *J. Geophys. Res.*, 100, 24911–24929.
- Read, J. F., and R. T. Pollard, 1993: Structure and transport of the Antarctic Circumpolar Current and Agulhas Return Current at 40°E. *J. Geophys. Res.*, 98, 12281–12295.
- Rudnick, D. L., 1997: Direct velocity measurements in the Samoan Passage. *J. Geophys. Res.*, 102, 3293–3302.
- Smith, W. H. F., and D. T. Sandwell, 1994: Bathymetric prediction from dense altimetry and sparse shipboard bathymetry. *J. Geophys. Res.*, 99, 21803–21824.
- Smith, W. H. F., and D. T. Sandwell, 1997: Global seafloor topography from satellite altimetry and ship depth soundings. *Science* April 7, submitted.
- Toole, J. M., K. L. Polzin, and R. W. Schmitt, 1994: Estimates of diapycnal mixing in the abyssal ocean. *Science*, 264, 1120–1123.



Yet the modification of bottom water in its spread northward through the oceans basins is important to our understanding of the thermohaline circulation.

A different problem is posed by the estimated overturning of the Indian Ocean. Using a section along 32°S Toole and Warren (1993) found that a surprisingly vigorous overturning was required to satisfy the flux constraints. In particular, their data across the northern end of the Mozambique Basin required a mean vertical velocity of order  $2 \times 10^{-4} \text{ cm s}^{-1}$ , which they considered “unbelievably large”. They comment that “the deep Mozambique Basin needs further investigation”.

Deep inflow into the Mozambique Basin through two trenches was monitored for a 21 month period between 1993 and 1995 (Pollard and Read, this issue) as part of the Southwest Indian Ocean Experiment (SWINDEX). CTD surveys made during the deployment and recovery cruises provided detailed information about the hydrographic structure. The circulation of bottom water will be considered first, followed by a brief discussion of transport and upwelling estimates. Pollard and Read (this issue) describe the bottom relief relevant to the discussion.

## Bottom water circulation

Data from four CTD sections are used to describe the circulation of bottom water (Fig. 1, Pollard and Read, this issue). Two sections were worked in 1993, across the northern end of the Agulhas

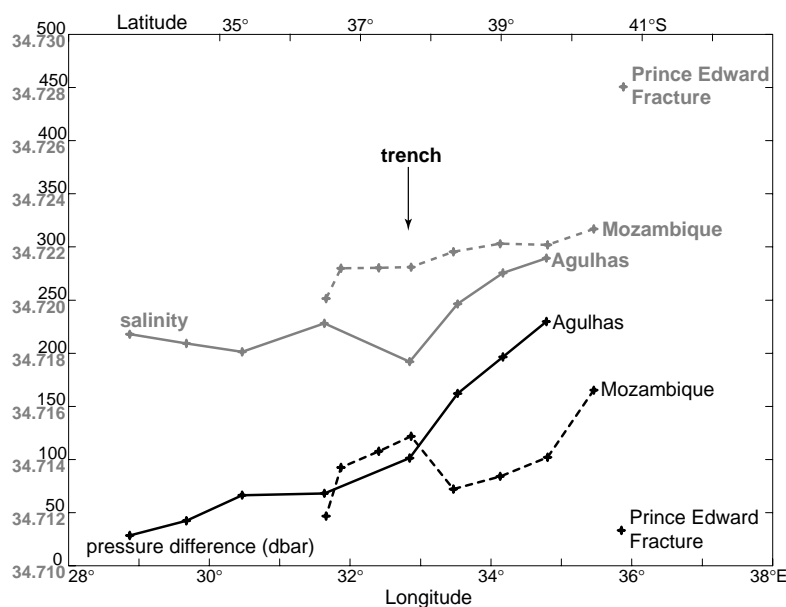


Figure 3. Salinity on the  $\sigma_4 = 46.00 \text{ kg m}^{-3}$  density surface and pressure difference between  $\sigma_4 = 45.995 - 46.005 \text{ kg m}^{-3}$ . The Agulhas section is plotted against longitude and the Mozambique section against latitude. The two are aligned along the axis of the deep trench running through both sections.

Basin and along the Prince Edward Fracture Zone. The other two were worked in 1995 and consisted of a repeat of the Agulhas Basin section and a new section across the Mozambique Basin.

Potential temperature and salinity from the Prince Edward Fracture show the classic division between the fresher Circumpolar Deep Water and more saline North Atlantic Deep Water that occurs at the Polar Front (Fig. 1). The difference is clear down to densities of  $\sigma_4 = 46.00 \text{ kg m}^{-3}$ . Below this the distribution of water masses changes. In the south there is evidence of the remnants of Weddell Gyre Warm Deep Water (as seen at the Greenwich Meridian, Whitworth and Nowlin, 1987) between  $0.2^\circ\text{--}0.3^\circ\text{C}$ . At this point it lies at a depth of about 4000 m, beneath Circumpolar Deep Water and has evidently subducted from the shallower depths, 500–1000 m where it usually appears as a salinity maximum in the Weddell Gyre.

The bottom water under consideration here is not the classic Weddell Sea Bottom Water (defined as  $<-0.7^\circ\text{C}$ ). Water this cold is too dense to leave the Enderby Abyssal Plain. It is the lighter water, formed by mixing between Weddell Gyre Warm Deep Water and Weddell Sea Bottom Water, that spreads northwards as Antarctic Bottom Water. Locally it is termed Weddell Deep Water. It is this water, seen at potential temperatures of about  $-0.4^\circ\text{C}$  at the southern end of the Prince Edward Fracture that can be traced into the Agulhas and Mozambique Basins.

$\theta/S$  profiles at the southern end of the Fracture show Circumpolar Deep Water overlying Weddell Gyre Warm Deep Water over Weddell Deep Water. However, at the northern end of the fracture, the bottom water lies on a

straight line between Weddell Deep Water and NADW. It appears anomalously salty when viewed next to profiles from the south of the fracture. Indeed, the three profiles at the northern end of the Prince Edward Fracture are the most saline of the bottom water profiles of both cruises. This can only be explained by strong direct mixing between NADW and Weddell Deep Water, sufficient to mix away the fresher intermediate characteristics of Weddell Gyre Warm Deep Water and Circumpolar Deep Water.

Profiles along the Prince Edward Fracture show a layer, up to 500 m deep in places, of cold bottom water. Sharp changes in properties mark interfaces with overlying deep water masses. These gradually disappear to the north, demonstrating that mixing is taking place. To arrive at the T/S characteristics at the northern end of the fracture, the bottom water must mix with successively warmer and more saline overlying water, as postulated by Mantyla and Reid (1983).

Potential temperature and salinity from the deep and bottom water of the Agulhas Basin show rather less structure than the Prince Edward Fracture. But below 4000 m there are considerable isopycnal slopes, and changes in isopycnal separation, indicating transport and changes in the bottom water masses through mixing (Fig. 2, page 22). The bathymetric rise at  $32^\circ\text{E}$  marks the southern end of the Mozambique Ridge (Fig. 1, Pollard and Read, this issue, page 21) and divides the section in two, with the Transkei Basin to the west (closed below 4000 m) and the Mozambique Basin to the east (closed below 3000 m). Both west and east of this rise, the density slopes imply movement of bottom water northwards (referenced to any level of no motion above the bottom), in the west and along the scarp above the deep trench. Thus there is inflow of water along their western boundaries into both the Transkei and Mozambique Basins.

For densities greater than  $46.02 \text{ kg m}^{-3}$ , the clear downward slopes to the east imply northward flow increasing with depth. It may also be inferred that these isopycnals slope downwards to the north beneath the deep-extending Agulhas Return Current. Thus the water flowing along these isopycnals has no exit below each basin's sill depth to the north. Rather, the flow must intersect the bottom along the sides of the basins, where turbulent mixing takes place, reducing the stratification and decreasing the density of the bottom water. The effect of this can be seen in the pycnostads between 4200–4700 m and the slight evidence of a reversal of the density slopes. Thus it can be deduced that there is weak cyclonic circulation in each basin consisting of a relatively strong inflow along the western boundaries and a slow re-circulation of the bottom mixed water over the rest of each basin.

Northward flow through the deep trench joining the Agulhas and Mozambique Basins at  $33^\circ\text{E}$  is confirmed by



a 21 month long current record obtained at 5810 m, 90 m off the bottom (Pollard and Read, this issue). The mean speed of  $12 \text{ cm s}^{-1}$  is reasonably consistent with the  $8 \text{ cm s}^{-1}$  calculated by taking 4000 m as a level of no motion.

Evidence of Weddell Deep Water at the mooring site at the northern end of the Prince Edward Fracture (Fig. 2) is strengthened by examination of the moored temperature record. During periods of northward flow the temperature dropped by about  $0.5^\circ\text{C}$  down to  $0.1\text{--}0.2^\circ\text{C}$ , suggesting that Weddell Deep Water flows in each year beneath NADW, raising the thermocline between these two water masses and causing the temperature at 4170 m to fall. The CTD casts were both taken at times when the thickness of the bottom layer of Weddell Deep Water was close to maximum. The profiles worked at the mooring site were separated from adjacent stations by the topography. Density gradients suggest that the water masses were different at the different stations (Fig. 2) so where the ridge peters out to the north the denser Weddell Deep Water in the fracture must spill down the slope to the west, enhancing bottom mixing in the Mozambique Basin.

The repeat section worked across the Agulhas Basin in 1995 showed the same density distribution as the first, from which the same circulation pattern can be inferred and a direct comparison can be made with the section across the Mozambique Basin (worked during the second cruise).

The section across the Mozambique Basin is dominated by a meander in the Agulhas Return Current, which influences isopycnal slopes to over 4000 m depth. However, below this there is a significant decrease in stratification with a west–east (north–south) density gradient. The deep stratification is considerably weaker than that across the Agulhas Basin and the densities are less, all of which re-inforces the hypothesis that there is a weak cyclonic circulation in the deepest part of the basin and friction induced turbulent mixing with overlying water takes place. The circulation may be enhanced by the meanders of the Agulhas Return Current.

The deep CTD salinity data were calibrated to better than 0.002, making it possible to examine very subtle variations in potential temperature and salinity. Extracting salinity on the density surface  $\sigma_4 = 46.00 \text{ kg m}^{-3}$  (Fig. 3) shows that salinities are at their lowest (34.718) in the two regions of inflow at and west of the deep trench on the Agulhas section. However, in the Prince Edward Fracture, the salinity reaches its highest value, 34.728. Across most of the Mozambique Basin section, salinities are at an intermediate value and salinities rise towards this also on the Agulhas Basin section east of the deep trench. The implication is that the inflow of saline water through the Prince Edward Fracture, though small, increases the salinity through much of the Mozambique Basin and the eastern side of the Agulhas Basin section.

Salinity remains low across the mouth of the Transkei Basin (to the west) indicating no admixture of water from the Prince Edward Fracture. This is consistent with cyclonic circulation of bottom water

in the Basin deduced earlier. However, the thickness (a measure of inverse potential vorticity) increases from west to east by a factor of three or more. This confirms that considerable bottom mixing is taking place, reducing the potential vorticity. However, the linearity of the T/S relation means that the mixing does not change the salinity on an isopycnal. Even more mixing is inferred at the northern exit of the Prince Edward Fracture, as the potential vorticity of the bottom water at that station is at least five times higher than that of stations to the north and west of it.

## Transport and upwelling estimates

To obtain transport estimates, the cross-sectional area of the CTD sections was estimated using the bathymetric data collected during the cruises. CTD profiles were extended downwards using the deepest common density gradient and geostrophic velocities were calculated using a reference level of no motion at 4000 m. Comparison with current meter data suggested that the velocities obtained were a slight under-estimate. The calculations were tested by ignoring hydrographic constraints and minimising the flow between each pair of stations by varying the reference level. The transports were reduced but retain the same sign and order of magnitude, indicating that the solutions are fairly robust.

The results (Table 1) show that the flow into the Transkei Basin was variable and probably depends on the location of the Agulhas Return Current. Flow across the entrance to the Mozambique Basin gave similar values for both occupations and was dominated by a 1 Sv flow along the Mozambique Scarp where the current meter data increases confidence in this value. The Mozambique section produced a larger flux than was expected, probably because of the presence of the Agulhas Return Current.

Upwelling velocities were estimated within each area bounded by the section and the 4000 m contour. The figures obtained were all large compared to published values, even when minimised estimates were used. The most robust value was that obtained from the inflow through the Agulhas Section giving an upwelling of  $10 \times 10^{-5} \text{ cm s}^{-1}$ . Toole and Warren obtained an upwelling velocity of  $20 \times 10^{-5} \text{ cm s}^{-1}$  at 2000 m from stations worked across the northern part of the Mozambique Basin and  $7 \times 10^{-5} \text{ cm s}^{-1}$  for their trans-Indian Ocean section along approximately  $32^\circ\text{S}$ .

Table 1. Transport below 4000 m (Sv)

	Agulhas section			
	Discovery 201		Discovery 213	
	ref 4000 m	minimised	ref 4000 m	minimised
	+0.43	+0.18	-0.15	-0.13
	+1.20	+0.72	+1.10	+0.69
Mozambique	Mozambique section			
	+1.75			

It has been shown (Toole, Polzin and Schmitt, 1994) that vertical mixing may be enhanced near ocean boundaries or over rough topography and may be of order  $10^{-3} - 10^{-2}$ . The Mozambique Basin is an area of very complex and rough topography, so may generate upwelling and mixing an order of magnitude greater than that found over the abyssal plains.

## Conclusions

Hydrographic data and current records show that there are at least two sources of bottom water in the Mozambique Basin. Fresher water enters from the Agulhas Basin, saltier water comes from the Enderby Basin, directly via the Prince Edward Fracture. It is reasonable to suppose that the water in the Agulhas Basin originated in the Enderby Basin, since there is no other gap in the topography to the west that is deep enough to allow penetration elsewhere of water of these characteristics. Thus, both types of water in the Mozambique Basin ultimately have the same origin. The different pathways are roughly the same length, so the different characteristics must result from some other aspect of the local hydrography. Comparison of the T/S curves from the Agulhas Basin section with those along the Prince Edward Fracture shows that the former all lie close to transitional curves that display strong mixing between NADW and Weddell Deep Water. Along both paths, the mixing must occur where the Weddell Deep Water crosses the Polar Front and isopycnals slope rapidly down to the north, bringing NADW into direct contact with Weddell Deep Water. However, the water that crosses the Agulhas Basin most likely enters that basin at about  $50^{\circ}\text{S}$  where the water is subject to slightly less intense mixing than that passing through the Prince Edward Fracture, accounting for the small differences in T/S properties between them.

Transport and upwelling estimates are higher than expected, with a transport of order 1 Sv into the Mozambique Basin concentrated along the deep trench at the foot of the Mozambique Scarp. This implies an upwelling velocity of  $10 \times 10^{-5} \text{ cm s}^{-1}$  over the Mozambique Basin. Enhanced mixing over the complex topography is inferred from the reduction in stratification of bottom water where the isopycnals intersect the sea bed.

## References

- Mantyla, A. W., and J. L. Reid, 1983: Abyssal characteristics of the world ocean waters. *Deep-Sea Res.*, 30(8A), 805–833.
- Mantyla, A. W., and J. L. Reid, 1995: On the origins of deep and bottom waters of the Indian Ocean. *J. Geophys. Res.*, 100(C2), 2417–2439.
- Toole, J. M., and B. A. Warren, 1992: A hydrographic section across the subtropical South Indian Ocean. *Deep-Sea Res.*, 40(10), 1973–2019.
- Toole, J. M., K. L. Polzin, and R. W. Schmitt, 1994: Estimates of diapycnal mixing in the abyssal ocean. *Science*, 264, 1120–1123.
- Whitworth, T. III, and W. D. Nowlin, Jr, 1987: Water masses and currents of the Southern Ocean at the Greenwich Meridian. *J. Geophys. Res.*, 92(C6), 6462–6476.

## Surface Flux Climatology (Version 1.1) available at SOC

A new global monthly mean air-sea heat flux, wind stress and precipitation climatology which has been produced at the Southampton Oceanography Centre (SOC) may now be accessed via the SOC public ftp site. The fields have been derived from the COADS1a (1980–93) dataset enhanced with additional metadata from the WMO47 list of ships. Ongoing work is being carried out to identify areas where improvements can be made to the climatology and we strongly encourage users to read the discussion of its strengths and weaknesses in the readme file at the ftp site.

The ftp procedure is:

- (1) ftp socnet.soc.soton.ac.uk
- (2) login anonymous
- (3) cd pub/sxj/clim/ascii or cd pub/sxj/clim/netcdf depending on choice of format (ASCII or netCDF).

Full details of the fields are given in these directories. The fields are freely available to interested users for non-commercial scientific research. For further information on the climatology see:

<http://www.soc.soton.ac.uk/JRD/MET/fluxclimatology.html>

Contact: Simon A. Josey, Elizabeth C. Kent, or Peter K. Taylor, James Rennell Division, Southampton Oceanography Centre, Empress Dock, Southampton SO14 3ZH, UK. [Simon.A.Josey@soc.soton.ac.uk](mailto:Simon.A.Josey@soc.soton.ac.uk)

## Errata

In the previous issue of the WOCE Newsletter (No. 28) and in the article by C. Andrié et al. (pages 11–13), fig. 2b is incorrect. The caption refers to a north-south component of L-ADCP measurements; instead the figure shows the east-west component of the same measurements (negative values for westward flows in grey).

The correct figure according to fig. 2's caption is shown below.

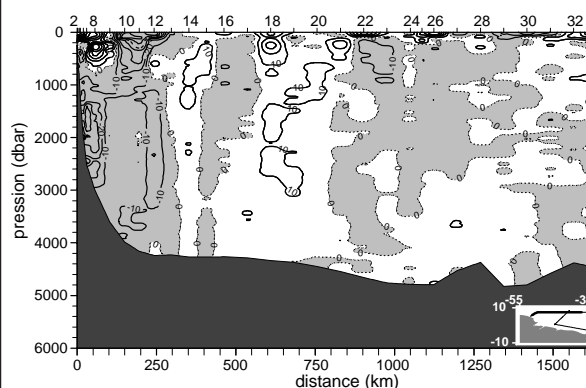
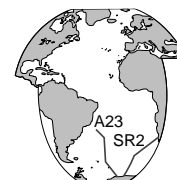


Figure 2b. Vertical sections along  $7^{\circ}30'\text{N}$  during ETAMBOT 1 of the north-south component of L-ADCP measurements (negative values for southward flows in grey).

# Tracer Studies in the Southern South Atlantic Within WOCE

Christine R  th, J  rgen S  ltenfu  , Henning Rose, Alfred Putzka, and Wolfgang Roether,  
Institut f  r Umweltphysik, Universit  t Bremen, Germany. bklein@physik.uni-bremen.de



As examples of our Southern Ocean work, we present tracer data ( $^3\text{He}$ , tritium, CFCs) collected on the WHP sections SR2 and A23 (Greenwich Meridian and 30  W, Fig. 1). While tritium and the CFCs are transient tracers,  $^3\text{He}$  is essentially a steady-state tracer in the Southern Ocean because the tritogenic contribution is small. This is due to low tritium concentrations, which at the same time imply a restricted signal to noise ratio in the tritium data.

## $^3\text{He}$ sections

While in the mixed layer helium approaches a solubility equilibrium with the atmosphere, sources in the interior lead to slightly elevated concentrations there. In the Southern Ocean one finds a prominent  $^3\text{He}$  signal, mostly advected from the Pacific, where the East Pacific Rise

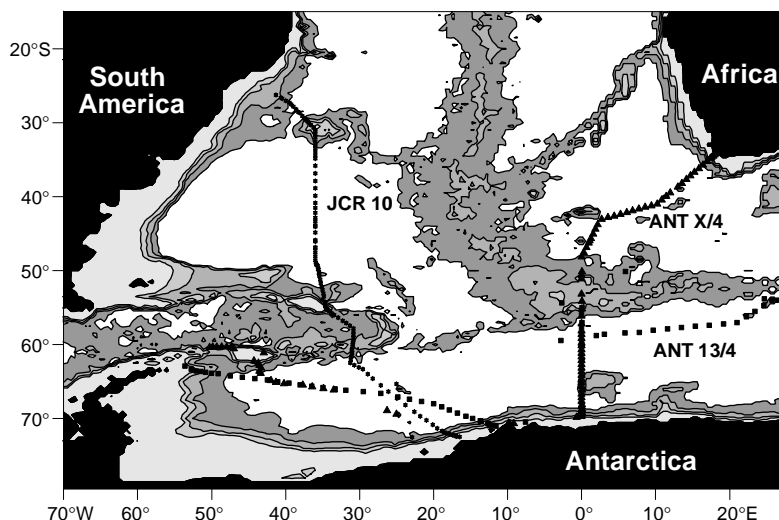


Figure 1. Tracks of JCR cruise 10 (A23, 1995), ANT X/4 (SR2, 1992) and ANT XIII/4 (SR2, 1996).

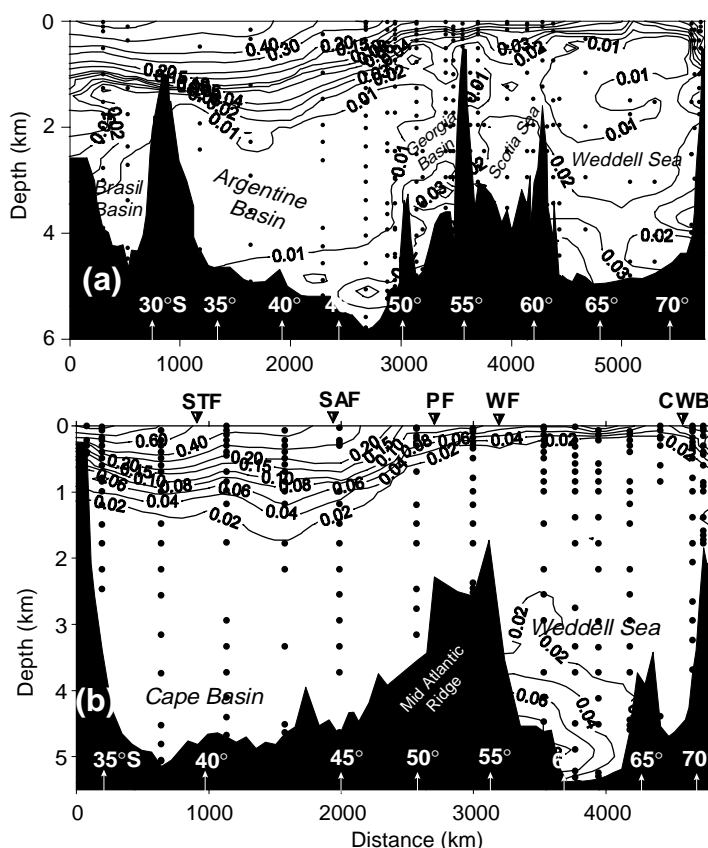


Figure 3. Like fig. 2 (page 23) but for tritium distribution. The values are given in TU. 1 TU represents a tritium/hydrogen ratio of  $10^{-18}$ . The detection limit is 10mTU, and the 1-Sigma measurement error 10mTU for (a) and 20mTU for (b). STF: Subtropical Front, SAF: Subantarctic Front, WF: Weddell Front.

represents a major  $^3\text{He}$  source. Hence the highest  $^3\text{He}$  values in the Atlantic sector are found in the Antarctic Circumpolar Current (ACC), while for all other waters ventilation of  $^3\text{He}$  to the atmosphere prevails so that concentrations are lower.

Fig. 2a (page 23) shows the  $^3\text{He}$  distribution along A23 (30  W, James Clark Ross cruise JCR10), 1995. We find a maximum in  $\delta^3\text{He}$  of 11‰ at 55  S in 1000 m depth, which characterises ACC waters. Evidently Circumpolar Deep Water (CDW) spreads northward encountering low- $\delta^3\text{He}$  North Atlantic Deep Water (NADW, centred near 2500 m depth). The influence of the latter is seen up to 45  S, where also splitting of CDW into its lower and upper part is evident. North of about 50  S, the isolines between about 2 and 5‰ follow the northward descent of Antarctic Intermediate Water (AAIW). CDW in the Weddell Sea is reflected by high  $\delta^3\text{He}$  values in the upper 1000 m of the Weddell Sea, with a maximum of 9‰ in Warm Deep Water (WDW) in about 400 m depth. From here,  $\delta^3\text{He}$  decreases continuously with depth, indicating an increasing contribution of recently ventilated waters. Values in the bottom waters of the Weddell Sea are less than 5‰, with a minimum (<4.5‰) in the north. Surprisingly, the lowest bottom  $\delta^3\text{He}$  values outside the Weddell Sea are found in the Georgia Basin and the southernmost parts of the Argentine Basin ( $\delta^3\text{He}$  <6.5‰), rather than in the Scotia Sea.

Fig. 2b (page 23) displays the distribution along the Greenwich Meridian (SR2; Polarstern cruise ANT X/4), 1992. Like for A23 (Fig. 2a), the highest  $^3\text{He}$



values are found in the ACC. It appears that the  $^3\text{He}$  maximum is only slightly reduced, which means that a dilution of the ACC waters, e.g. by NADW, between the two sections is rather small. Other similarities are a descent of the isolines related to the AAIW, an encounter with NADW, now centred near 3000 m depth, towards the north, and low values in the Weddell Sea bottom waters, which seemingly are even slightly lower than on A23, but again with the lowest values in the north. However, the bottom water in the northern part of the section (north of the Midatlantic Ridge), are higher than in Fig. 2a, indicating a rather lower influence of low- $^3\text{He}$  water from the Weddell Sea. Taking our Weddell Sea surface water average (-0.9%) to represent the ventilated portion, and assuming 9% for the original CDW, it follows that the ventilated portion of the bottom waters (<5%) is at least 40%.

The two sections demonstrate the potential of  $^3\text{He}$  as a water mass tracer, allowing in particular a distinction between ACC waters and the more ventilated ones leaving the Weddell Sea (CDW vs. Weddell Sea Deep Water).

### Tritium sections

The same sections but showing tritium are in Figs. 3a and b. In both sections, the surface water concentrations exhibit a pronounced southward drop across the ACC. This contrasts with a southward increase in the atmospheric input of tritium (which occurs via water vapour exchange and precipitation). Evidently, the tritium dilution by mixing with low-tritium subsurface waters is far faster in the south. As is well known, this interplay of input and dilution renders assessments of the tritium source function difficult. However a benefit is that the actual spatial pattern is much different from that of the common CFCs, for example (cf. Fig. 4).

In the thermocline north of 50°S a closer look reveals nearly constant concentrations along isopycnals, and furthermore in the AAIW range a little higher tritium concentrations on the more eastern section (Fig. 3b), indicative of a tritium input from the Indian Ocean. The values in the deeper water column are in many places below detection limit. Exceptions are the near-bottom waters in the Weddell Sea with a rather strong signal at the base of the northern slope, the Scotia Sea, and the Georgia and Argentine Basins (Fig. 3a); like for  $^3\text{He}$ , it appears that the signal is more pronounced in the latter two regions than in the Scotia Sea. There is also a clear signal in upper NADW in the north (about 2000 m depth), and in the Antarctic Coastal Current. An interesting feature is significant tritium adjoining the southern slope of the Weddell Sea in the A23 section (Fig. 3a) but only an indication of it in the SR2 section (Fig. 3b), possibly partly due to a concentration increase between 1992 and 1995 and to sampling limitations in the Polarstern section. However, the data in Fig. 3b had a slight contamination problem, so that this and several other features appear as less pronounced compared to Fig. 3a. The tritium signal at the southern slope is well correlated with a CFC-11 signal

(cf. Fig. 4), confirming a westward deep flow of waters ventilated further east (Locarnini et al., 1997).

### CFC sections

The distributions of CFC-11 across the Weddell Sea from two occupations of SR2 (Polarstern ANT X/4 and XIII/4), 1992 and 1996, are shown in Fig. 4. The deep interior is fully resolved due to the more sensitive CFC-11 measurement compared to that of tritium. A very clear feature is minimum concentrations between several hundred and approximately 2500 m depth, with absolute minima in about 1000 m near mid-section, i. e. below the centre of the CDW, and distinctly higher values over the entire water column towards both the southern and northern slopes. The deep high-CFC-11 core in the north reflects young waters advected from the sources in the south-west of the Weddell Basin, but the higher concentrations further up indicate addition of newly formed water over the entire water

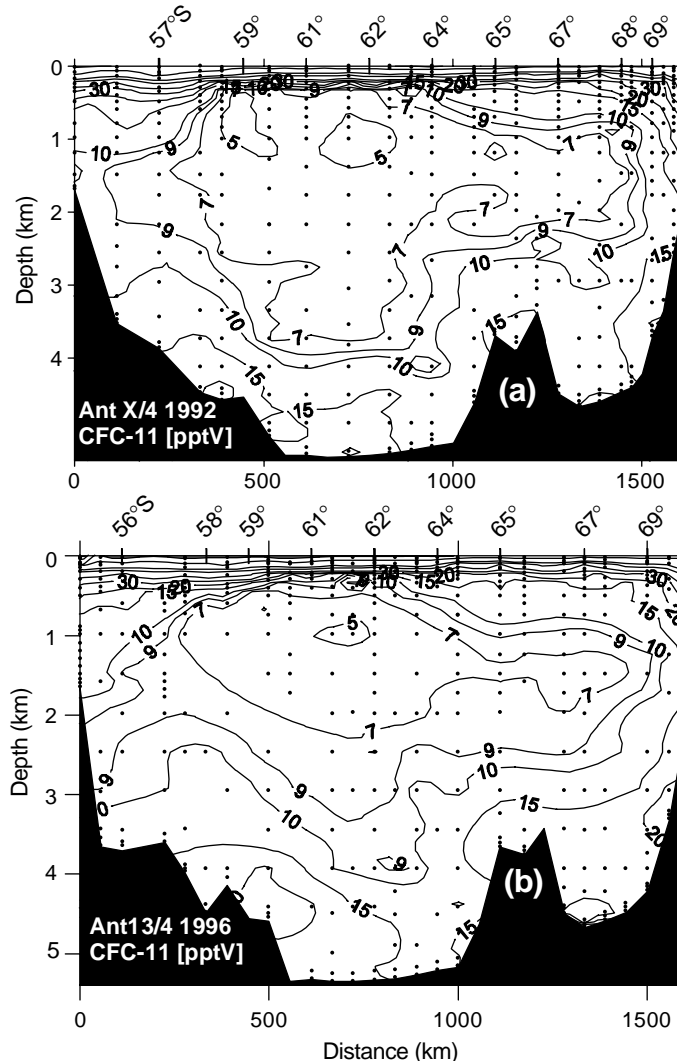


Figure 4. CFC-11 section for two occupation of SR2, Weddell Sea sector, i.e. ANT X/4, 1992 (upper diagram), and ANT XIII/4, 1996 (lower diagram). The values are given as equivalent partial pressures (pptv). Note that in contrast to Figs. 2–3 the Antarctic continent is to the left.



column. The high values in the south are to be ascribed to the mentioned source further east. The general doming of the isolines is in keeping with the well-known cyclonic gyre circulation (Fahrbach et al., 1995). Noteworthy is the general consistency in the pattern of the two CFC-11 sections repeated several years apart. There is furthermore a reflection of the transient character of the CFCs, evident for example in a shrinking of the regions enclosed by the 7 and 5 pptv isolines, and in an expansion for the 15 pptv isoline in the near-bottom waters.

## Conclusion

The examples presented should convey a feeling that the tracer data available are sufficient to resolve the water mass structure in considerable detail, and that they can yield useful information on mixing within, and renewal of, the Southern Ocean waters. The emphasis in tracer work is generally on the CFCs, but we hope that the sections shown caution one that tritium and  $^3\text{He}$  should not be ignored. It is true that particularly in the Southern Ocean the tritium distribution cannot be resolved as well as those of the CFCs. But, except in the rather old waters, non-redundant information is obtained due to the distinctly different

source functions of these tracers.  $^3\text{He}$ , being essentially a steady-state tracer, is all different, and is resolved well enough to represent a powerful water mass tracer. The details of all this remain to be worked out.

## Acknowledgements

We acknowledge funding by the Bundesministerium für Bildung und Forschung, the DFG and the University of Bremen (FNK). Gerhard Fraas and Klaus Bulsiewicz carried out the helium isotope and CFC measurements. We are grateful to the P. Lemke, E. Fahrbach, and K. Heywood, chief scientists, and to the masters and crews of the Polarstern and James Clark Ross cruises for a fruitful and pleasant cooperation.

## References

- Fahrbach, E., M. Schröder, and A. Klepikov, 1995: Circulation and Water Masses in the Weddell Sea. Berichte aus dem Fachbereich Physik; Report 65; Alfred Wegener Institut, Bremerhaven.
- Locarnini, R. A., K. A. Van Scoy, A. J. Watson, M. P. Meredith, K. J. Heywood, and B. A. King, 1997: Direct Evidence of Ventilation of the Weddell Gyre by Multiple Sources of Deep Water. J. Geophys. Res. (sub.)

## Hydrography and Baroclinic Transport between Africa and Antarctica on WHP Section I6

*Young-Hyang Park and Edwige Charriaud, Laboratoire d'Océanographie Physique, Muséum National d'Histoire Naturelle, Paris, France; and Alain Poisson, Laboratoire de Physique et Chimie Marines, Université Pierre et Marie Curie, Paris, France.*  
park@mnhn.fr



From February to March 1996 WHP section I6 between Africa and Antarctica at 30°E has been occupied during the CIVA-2 cruise from the RV Marion Dufresne II. This cruise was a reoccupation of the section in its totality, completing the partially occupied section (44°S–Antarctica) during the 1993 CIVA-1 cruise. The Chief Scientist was Alain Poisson and the PI of CTD work was Young-Hyang Park.

The section started from a point at a bottom depth of 150 m (33°S, 28°E) on the continental shelf SW of Durban, directed to the SE, cutting the Agulhas Current perpendicularly as far as St. 14 (35°S, 30°E), then continuing south along 30°E until encountering the pack ice (69°S, 30°E) on the continental shelf off Antarctica. It included a total of 94 full-depth CTD stations, with station intervals varying from 20 nm near fronts to 40 nm south of 53°S, and stations every 500 m of depth on the continental slopes at each end of the section. A Neil-Brown CTD with 24 Niskin bottle rosette was used. Water samples at a maximum of 48 levels were taken for analysis of salinity, oxygen, nutrients, CFC, alkalinity, and dissolved inorganic carbon on all stations. Helium, carbon 13 and 14, tritium, oxygen 18, barium, and neodymium were sampled on selected stations.

Here we present some preliminary results from the analysis of CTD data only.

The section is located near the boundary between the Atlantic and Indian sectors of the Southern Ocean which are connected by three distinct circulation systems of different origins: the Agulhas Current system to the north, the Antarctic Circumpolar Current (ACC) in the central part, and the Weddell Gyre to the south. This area is characterised also by the presence of prominent topographic reliefs such as the Agulhas Plateau, the Mozambique Plateau within the Agulhas Current system, and the SW Indian Ridge with its complicated deep fractures centred at about 50°S in the ACC regime. The main purpose of the physical component of the cruise was to document the inter-basin exchange and modification of different water masses, and to quantify the partition of volume transport in the three different circulation systems just mentioned.

Fig. 1 shows full depth temperature and salinity sections. The cumulative baroclinic transport relative to the bottom, integrated from the African coast, is shown on the top panel of Fig. 1, which will be discussed later in this note. The most remarkable finding from the property sections is an abrupt jump in property isolines within the whole

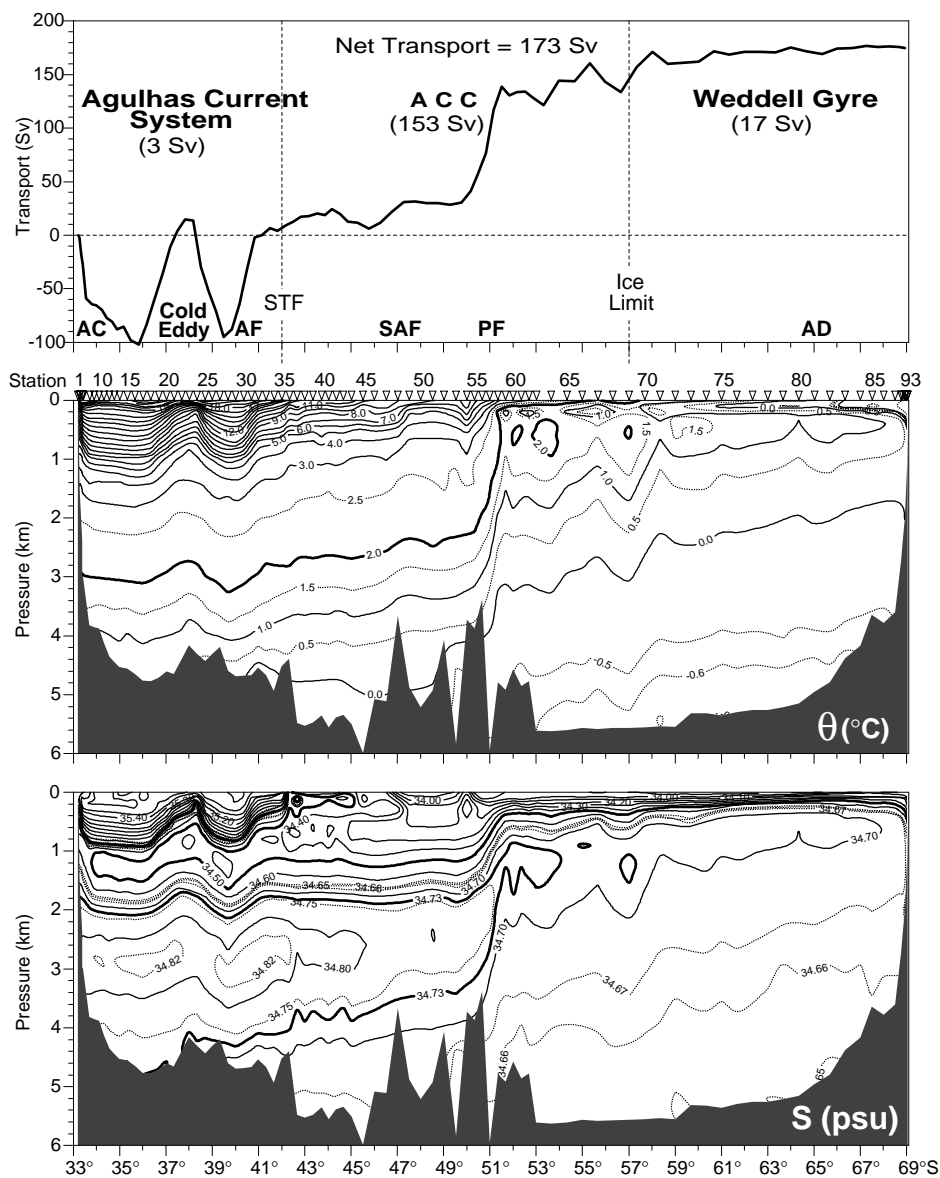


Figure 1. Potential temperature and salinity along WOCE section I6 at 30°E. Also shown in the upper panel is the cumulative baroclinic transport relative to the bottom, integrated from the African coast. Major fronts are: Agulhas Current front (AC), Agulhas Return Current front (AF), Subtropical Front (STF), Subantarctic Front (SAF), Polar Front (PF), Ice Limit, and Antarctic Divergence (AD).

water column immediately south of the summit of the SW Indian Ridge, forming a veritable wall between the Agulhas Basin to the north and the Weddell-Enderby Basin to the south. The Polar Front (PF) was observed precisely at this bottom-reaching discontinuity at 51°S. The high salinity North Atlantic Deep Water (NADW) fills the deep layer below 2000 m of the Agulhas Basin, with increasing salinity toward the Agulhas Current system, indicating the major entry point of the water there. Considering the maximum salinity of 34.73 in Drake Passage, the deep water below 2000 m in the Weddell-Enderby Basin is completely sheltered from the influence of NADW. However, in the intermediate layer centred at 1300 m there is evidence that the NADW influence penetrates to the

south of the ridge as far as 57°S, as suggested by isolated patches of relatively saline and warm water ( $>34.73$ ,  $>2^{\circ}\text{C}$ ) located to the south of the PF. Such patches, which are a commonly observed feature in the area (Jacobs and Georgi, 1977; Gouretski and Danilov, 1993), indicate that the southward penetration of saltier deep water may occur as a result of some regional eddy activities. TOPEX/POSEIDON altimetry reveals relatively high eddy activity just downstream of the deep fracture zone of the SW Indian Ridge (Park and Gambéroni, 1995); Gouretski and Danilov (1993) showed from a simple inertial-jet model that the current-topography interaction in the area is responsible for the generation of meanders and southward displacement of the eddies. The deep fracture zone also permits the northward spread of Antarctic Bottom Water which is the modified Weddell Sea Deep Water, advected from the western Weddell Basin along the foot of the mid-ocean ridge.

During the cruise, the Agulhas Current system was composed of (1) the SW-flowing Agulhas Current whose core was tightly attached to the continental slope within 30 km from the shelf break; (2) its eastward retro-flection or the Agulhas Return Current which was identified at 41°S; (3) and a vigorous cyclonic cold eddy centred at 38°S in between the two opposing currents. Examination of water

characteristics indicates that the eddy must have been detached from the frontal zone, causing the intrusion into the subtropical zone of cooler, fresher Subantarctic water originating from the south of the Subtropical Front (STF). This area is known as the strongest eddy activity zone in the world's oceans. The quasi-permanent occurrence of topographically-generated powerful meanders and eddies has been well documented (Gründlingh, 1978; Lutjeharms and Van Ballegooyen, 1984; Weeks and Shillington, 1994).

The ACC on the section covers the area between the STF (42°S) and the northernmost extent of sea ice in winter (hereafter, Ice Limit), although the current during the cruise was mostly concentrated at the PF. The Ice Limit has been observed at 57°S during the two CIVA cruises and can

be identified by the northern end of a well-defined band of the surface salinity minimum in summer section. This limit constitutes a natural boundary between the ACC and the Weddell Gyre. It also serves as a major route of meltwater originating from the Weddell Basin (Park et al., 1997). The Subantarctic Front (SAF), or the beginning of cross-frontal sinking of Antarctic Intermediate Water below 500 m, showed a double structure at 47° and 50°S, probably due to a strong meandering of flow at the moment of our observations. The southern branch of the front was completely merged with the PF, resulting in the strongest PF ever observed in this part of the ocean. The situation during the 1993 CIVA-1 cruise was quite different. The SAF appeared as a single structure at 58°S while the PF revealed a double structure at 50° and 52°S, splitting the ACC vein into two branches. The 1987 RRS Discovery data along 32°30'E (Read and Pollard, 1993) show a complete merging of the PF and SAF into a unique, single structure at 48°S. This information all together indicates a highly time-variable flow regime close to the SW Indian Ridge.

Fig. 2 shows surface geostrophic velocities calculated relative to the bottom between neighbouring stations and corresponding full-depth transport density. The Agulhas Current system was the most energetic current system observed on the section, with surface velocities reaching up to  $1.75\text{ m s}^{-1}$  and flowing alternatively eastward and westward in a meridional interval of 200–300 km. The ACC was strongly channelled through the deep fracture zone, with a peak speed of  $0.7\text{ m s}^{-1}$  at the PF, probably the highest current speed ever observed at this front. In the Weddell Gyre regime, the current was extremely weak ( $< 0.05\text{ m s}^{-1}$ ) and revealed a near-barotropic vertical structure. In this area geostrophy does not show any significant westward current along the Antarctic continental margin, except in the southern-most pair of stations.

The net transport across the entire section amounts to 173 Sv (see the upper panel of Fig. 1). This baroclinic transport is about 40 to 60 Sv greater than the previous estimate of a nearby

area during the Conrad cruises (Jacobs and Georgi, 1977) and also well over the expected range of the total ACC transport (baroclinic + barotropic) through Drake Passage ( $130 \pm 3\text{ Sv}$ ,  $s=10\text{ Sv}$ ) (Nowlin and Klinck, 1986). It is partitioned by 3 Sv in the Agulhas Current system, 153 Sv in the ACC regime, and 17 Sv in the Weddell Gyre regime. The near-zero net transport in the Agulhas Current system results from the contribution of the Agulhas Current (100 Sv south-westward), the Agulhas Return Current (103 Sv eastward), as well as the cyclonic cold eddy (alternating 120 Sv eastward and westward) which is sandwiched between the two near-compensating opposing currents of the system. In the ACC regime about 70% of the transport (109 Sv) was concentrated at the PF, which was exceptionally strengthened in 1996 due to the confluence

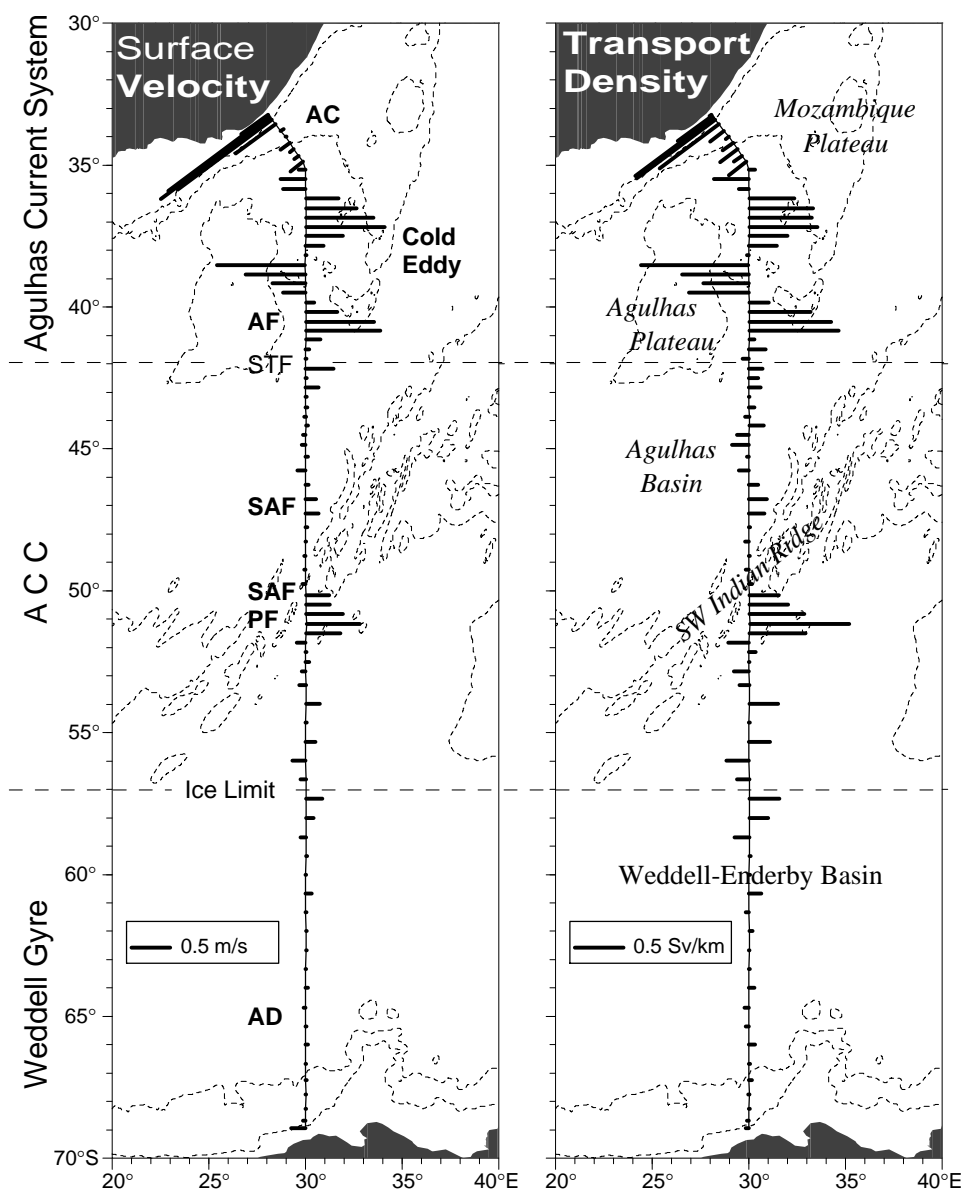


Figure 2. Surface geostrophic velocities relative to the deepest common sample depths between station pairs (left) and corresponding full-depth transport per unit along-section distance (right). Isobaths are 2000 and 4000 m.

with a meandering branch of the SAF. The net transport in the Weddell Gyre regime was far from zero (17 Sv eastward) and did not show any significant westward transport along the Antarctic continental margin, in contradiction to what was expected from previous work with altimetry, numerical model outputs, and historical iceberg tracking (Park and Gambéroni, 1995). This could be due to the inadequacy of the dynamic method in such a highly barotropic regime. If so, this calls for direct current measurements to correctly constrain the ACC flux across the section. Finally, it is worthwhile to stress that the importance of the barotropic current, or near-bottom current, is not restricted to subpolar regions but can be equally important even in highly baroclinic subtropical regions such as the Agulhas Current system. In fact, recent LADCP measurements across the Agulhas Current on the continental slope off Port Edward revealed a strong ( $> 0.2 \text{ m s}^{-1}$ ) near-bottom north-eastward flow underneath the Agulhas Current vein (Beal and Bryden, 1996). In such a case a zero reference level at the bottom would yield a very erroneous geostrophic transport. Our transport estimate for the Agulhas Current (100 Sv) is about 30 Sv greater than that estimated by Beal and Bryden (1996) and should be considered with caution. In conclusion, without any reference to direct current measurements, our estimate of the geostrophic volume transport in this section is possibly much different from the absolute one.

## References

- Beal, L., and H. Bryden, 1996: The water masses, velocity structure and volume transport of the Agulhas Current at 31°S. *International WOCE Newsletter*, 22, 20–27.
- Gouretski, V., and A. I. Danilov, 1993: Weddell Gyre: structure of the eastern boundary. *Deep-Sea Res.*, 40, 561–582.
- Gründlingh, M. L., 1978: Drift of a satellite-tracked buoy in the Southern Agulhas Current and Agulhas Return Current. *Deep-Sea Res.*, 25, 1209–1224.
- Jacobs, S. S., and D. T. Georgi, 1977: Observations on the southwest Indian/Antarctic Ocean. In: *A Voyage of Discovery*, pp43–84. M. Angel, editor, Pergamon Press, Oxford.
- Lutjeharms, J. R. E., and R. C. Van Ballegooyen, 1984: Topographic control in the Agulhas Current system. *Deep-Sea Res.*, 31, 1321–1337.
- Nowlin, W. D., and J. M. Klinck, 1986: The physics of the Antarctic Circumpolar Current. *Rev. Geophys.*, 24, 469–491.
- Park, Y.-H., and L. Gambéroni, 1995: Large-scale circulation and its variability in the south Indian Ocean from TOPEX/POSEIDON altimetry. *J. Geophys. Res.*, 100, 24,911–24,929.
- Park Y.-H., E. Charriaud, and M. Fieux, 1997: Thermohaline structure of the Antarctic Surface Water in the Indian sector of the Southern Ocean. *J. Mar. Sys.*, in press.
- Read, J. F., and R. T. Pollard, 1993: Structure and transport of the Antarctic Circumpolar Current and Agulhas Return Current at 40°E. *J. Geophys. Res.*, 98, 12,281–12,295.
- Weeks, S. J., and F. A. Shillington, 1994: Interannual scales of variation of pigment concentrations from coastal zone color scanner data in the Benguela Upwelling system and the Subtropical Convergence zone south of Africa. *J. Geophys. Res.*, 99, 7385–7399.

## Repeated Observations of the ACC on WOCE SR1b

Marc A. Garcia, Oswaldo Lopez, Joan Puigdefabregas and Joaquim Sospedra,  
Universitat Politècnica de Catalunya, Barcelona, Spain. [garcia1@etseccpb.upc.es](mailto:garcia1@etseccpb.upc.es)



BIO Hesperides occupied the WOCE SR1b repeat section across the Scotia Sea both on 15–20 February 1995 and on 15–20 February 1996. In each cruise (hereafter referred to as DRAKE 95 and DRAKE 96 respectively), the same set of 21 hydrographic stations with characteristic spacing of 20 nm was sampled. On each station, surface-to-bottom CTD casts were performed with a Mk IIIC probe to obtain continuous profiles of temperature, salinity, dissolved oxygen concentration, fluorescence and light transmission, and water samples were collected at 24 levels. In addition, velocity profiles were recorded both en-route and on stations by means of a hull-mounted 150 kHz-Narrow-Band ADCP. The Skyfix station located in the Falkland Islands was used for DGPS positioning.

The results of the two cruises displayed the characteristic zonation of water masses defined by the four ACC hydrographic fronts – the Subantarctic Front (SAF), the Polar Front (PF), the Southern ACC Front (SACCF) and the Continental Water Boundary (CWB). The net geostrophic transport computed with reference to the

common deepest layer of each pair of adjacent stations was similar in both cruises (about 140 Sv in DRAKE 95 and 131 Sv in DRAKE 96). However, closer comparison of the February 1995 and February 1996 results revealed changes in the structure of the ACC which in principle could be attributed either to the interannual variability of the ACC regime or to the current mesoscale activity. AVHRR imagery screened for us and provided kindly by the University of California at San Diego's AARC has further shown that the main observed differences were related to the ACC mesoscale variability.

Fig. 1 shows the vertical distributions of potential temperature on SR1b derived from the DRAKE 95 and DRAKE 96 data sets respectively using the same interpolation method (kriging with Surface Mapping System v. 5.00). Adopting the criteria proposed by Deacon (1933) and by Peterson and Whitworth (1989) to locate the core of the SAF and the PF in those distributions, we conclude that the SAF was approximately at 56°08'S in DRAKE 95 and at 55°52'S during DRAKE 96. A similar northward shift



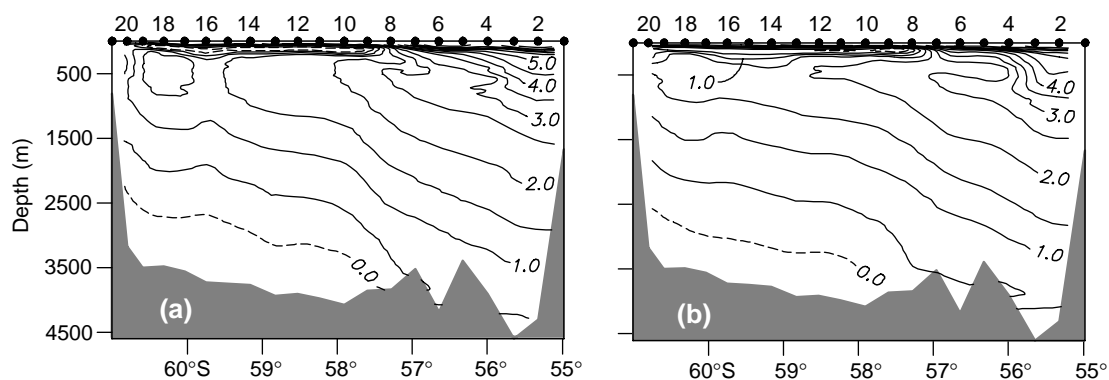


Figure 1. Observed vertical distribution of potential temperature on WOCE SR1b during DRAKE 95 (a) and DRAKE 96 (b). Units are °C.

was observed in the case of the PF, the front core being at 57°17'S in 1995 and at 56°56'S in 1996. In contrast to that, the hydrographic signature of the SACCF defined according to Orsi (1993) was some 40 nm further to the south in DRAKE 96 with respect to its position during DRAKE 95.

Another remarkable feature is the dome-like structure centred on 59°30'S in Fig. 1a, which is related to the discontinuity of the 1.5°C isotherm observed south of the SACCF in DRAKE 95. A similar structure was observed by King and Alderson (1994) on board RRS James Clark Ross in November 1993, but no such feature was observed in DRAKE 96. The DRAKE 95 ADCP data evidence that the previous feature was linked to a cyclonic circulation pattern (Fig. 2). Fig. 3 (page 23) shows an AVHRR image of the Scotia Sea and Drake Passage acquired by NOAA-12 on 14 February 1995 at 10.06 GMT (i.e. roughly at the start of the DRAKE 95 cruise. Unfortunately no cloud-free images were available between 15 and 20 February). The image displays intense mesoscale activity of the ACC in the PF and Antarctic Zones including dramatic meandering north of Elephant Island. The sharp ACC meander located in that area at the time of the image acquisition drifted eastwards subsequently, which explains that we did not observe any significant current reversal in DRAKE 95 north of 59°S. As for the cyclonic pattern mentioned above, our conclusion is that in February 1995 we steamed across the eastward-shifting cyclonic eddy which can be traced in the image north-west of Elephant Island at 59°30'S. The available cloud-free AVHRR images contemporary to the

DRAKE 96 cruise (not shown here) display less energetic ACC meandering and smaller, anticyclonic eddies which we missed in the survey.

Bottom-reaching cyclonic eddies as the one Hesperides steamed across at the southern Scotia Sea in February 1995

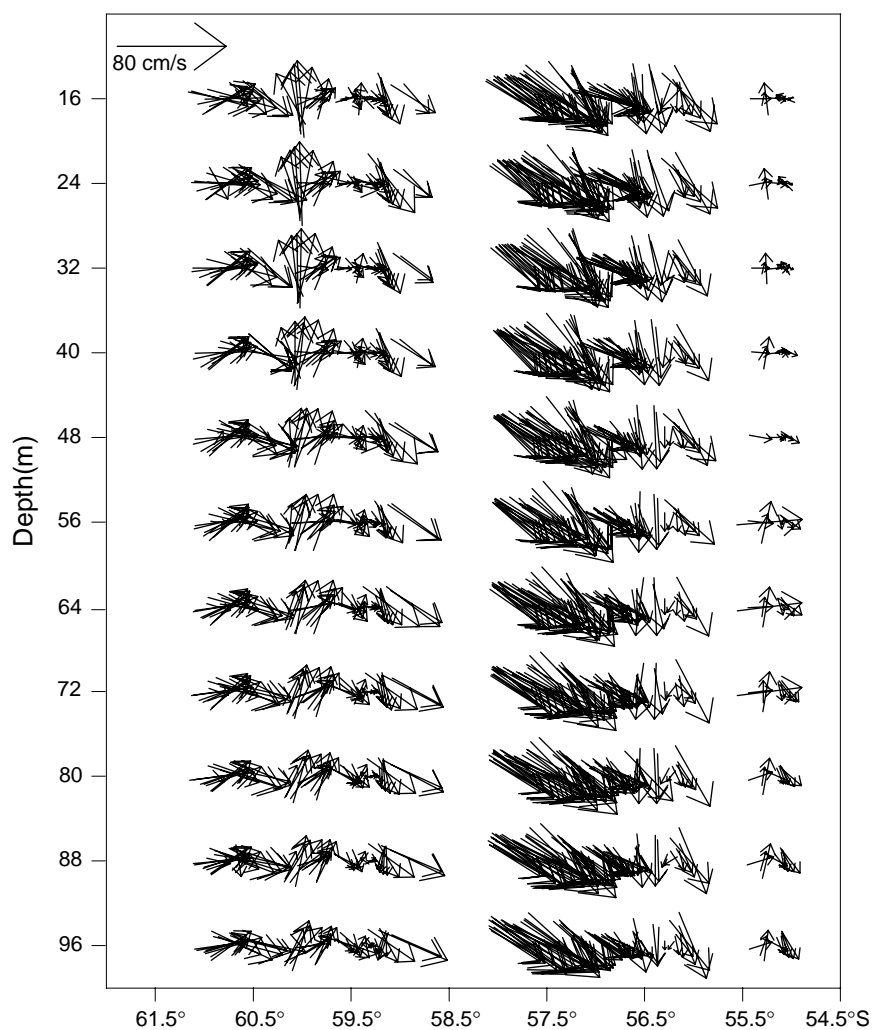


Figure 2. DRAKE 95 cruise. ADCP current velocity distributions on SR1b at depth layers from 16 to 96 m. "Blanks" are due to lack of data.

can play a crucial role in the export of Antarctic Bottom Water (AABW) to lower latitudes. The cold core adjacent to the ACC meander observed north of Elephant Island in Fig. 3 might be a remnant of such a cyclone after being “sucked” by the ACC jet related to the SACCF and moved to lower latitudes, bringing a large volume of AABW with it. Comparison and integration of the different data sets obtained from the several occupations of SR1b during WOCE, as planned in the July 1997 WOCE Southern Ocean Workshop, should allow better understanding of the deep exchanges between the Antarctic Zone and the global ocean across the Scotia Sea.

## Acknowledgements

We acknowledge the support of the crew of BIO Hesperides during the DRAKE 95 and DRAKE 96 cruises. We also

thank UCSD's AARC for providing us with NOAA/AVHRR imagery useful to improve our understanding of the DRAKE 95 and DRAKE 96 data sets. This study has been partially funded by the Spanish Comision Interministerial de Ciencia y Tecnologia, grant No. AMB94-0436.

## References

- Deacon, G. E. R., 1933: A general account of the hydrology of the South Atlantic Ocean. *Discovery Reports*, 7, 171–238.
- King, B., and Alderson, S., 1994: SR1 Repeat Hydrography/ADCP, Drake Passage, November 1993. *Int. WOCE Newsletter*, 15, 13–15.
- Orsi, A. H., 1993: On the extent of frontal structure of the Antarctic Circumpolar Current. PhD Thesis, Texas A&M University, TX, USA, 74pp.
- Peterson, R. G., and Whitworth III, T., 1989: The Subantarctic and Polar fronts in relation to deep water masses through the Southwestern Atlantic. *J. Geophys. Res.*, 94, 10817–10838.

## High Resolution XBT/XCTD Measurements Across Drake Passage

*Janet Sprintall, Ray Peterson, and Dean Roemmich, Scripps Institution of Oceanography, USA; and Jose Gallo, Instituto Antartico Argentino, Argentina. janet@beqa.ucsd.edu*



In September 1996, we began a high resolution XBT/XCTD sampling programme across the Drake Passage from US Antarctic Supply Vessels travelling from Punta Arenas, Chile to Palmer Station, Antarctica. Six transects have been completed to date, and it is intended to sample from 6–8 cruises on a year-round basis. The purpose of the programme is to monitor seasonal, and eventually interannual changes in upper ocean temperature variability across the Southern Ocean choke point. The Southern Ocean is a critical element in global climate and plays a major role in inter-basin exchange. White and Peterson (1996) suggest that changes in sea surface temperature in the Southern Ocean may originate from El Niño activity in the tropical Pacific Ocean. The observed temperature variability travels completely around the southern hemisphere within the Antarctic Circumpolar Current (ACC), and is most intense within Drake Passage. The subsurface XBT/XCTD temperature measurements will contribute information on the depth to which the climate signals penetrate. This provides a valuable dimension towards understanding the interaction between the upper ocean and the atmosphere, and the role of Drake Passage in transmitting these climate anomalies around the globe. The XBTs are Sippican Deep Blue probes, and return temperature data to depths of 850 m. Typically about 65 XBTs are dropped per cruise, with station spacing of about 6–10 km across the major frontal regions of the passage, and 10–15 km elsewhere. The XCTDs return both temperature and salinity (conductivity) data to depths of around 1000 m. Generally 12 XCTDs are dropped per cruise, again with sampling more closely spaced in the frontal regions. The nature of the supply vessel – to ferry support-personnel and

scientists who conduct research in Antarctic regions – and the abhorrent weather within the passage itself, means that the track is not always exactly repeating (Fig. 1). However, generally sampling begins at Isla de los Estados at the south-east tip of Tierra del Fuego, across Drake Passage, to Smith Island (Palmer Station transits) or to King George

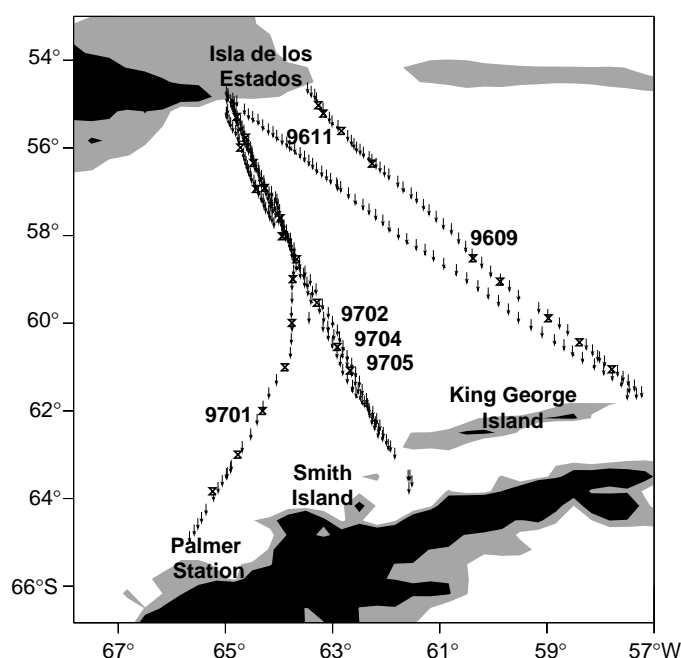


*Figure 1. Location of XBTs (arrows) and XCTDs (crosses) from 6 high density transects across Drake Passage. The 200 m bathymetry is marked in grey.*

Island (COPA Station transits). To ensure all temperature changes occurring within the flow are measured, sampling begins and ends at the 200 m bathymetry line. The Drake Passage crossing generally takes about 2 days to complete. Because of the intense yearly sampling schedule, and the logistical and berthing space limitations of the vessels, this programme relies on the generous assistance of the NSF supported Antarctic Supply Associates and the cruise participants to undertake the sampling. Such assistance is genuinely appreciated and crucial to the continued success of the programme. The XBT profiles were carefully quality controlled to allow expression of the subtle temperature fluctuations within the region. Fine scale structure of interleaving is evident in many of the individual temperatures profiles, although for this brief note we will focus on describing the upper ocean thermal structure in Drake Passage in general terms of frontal positions and dominant features between and within each transect. Temperature sections from six crossings undertaken during September 1996 (9609), November 1996 (9611), January 1997 (9701), February 1997 (9702), and two transects in April 1997 (9704; 9705), are shown in Fig. 2 (page 24). Each temperature section was produced by objective mapping to 10 m depth by 10 km alongtrack. The temperature sections of Fig. 2 illustrate the rich structure and provide a fascinating insight into the temporal evolution of the upper ocean thermal structure within the Drake Passage. The ACC in Drake Passage is characterised by a series of relatively narrow eastward flowing jets, separated by broader bands of flow. Each jet is associated with a sharp temperature front, which forms the boundary between different water masses. The station spacing of the XBT/XCTDs have been designed to resolve these fronts. At the southern end of all the transects except 9701, the isothermal layer of cold water is bordered to the north by a strong subsurface temperature gradient that forms the ACC Southern Front (ACC-SF), or the continental water boundary. In the upper layer, south of the ACC-SF is continental slope water, north of it is the cold Antarctic Surface Water (ASW). The sequential sections of Fig. 2 illustrate how ASW is formed. During the winter (9609) the surface layer is cooled to  $<1^{\circ}\text{C}$  to a depth of around 150 m. With spring (9611) and summer (9701; 9702) heating, the surface layers are warmed, trapping the temperature minimum water. The minimum layer may consist of patches of warmer water that have intruded from above, or from below by the Circumpolar Deep Water (CDW) which has a nearly constant  $2^{\circ}\text{C}$  temperature. With the return to cooler conditions in April (9704; 9705), the alongtrack vertical temperature gradient diminishes as the winter water again begins to form at the surface. The sharp temperature gradient that marks the northern termination of the temperature minimum layer is known as the Polar Front (PF). A definition of the PF as the northern extent of the  $2^{\circ}\text{C}$  isotherm near 200 m depth (Botnikov, 1963), locates the front around  $58^{\circ}\text{S}$  in nearly all sections. North of the PF is the Antarctic Polar Frontal Zone (APFZ), which is limited to the north by the Subantarctic Front (SAF). The SAF, defined as a subsurface temperature gradient in the tem-

perature range of  $3^{\circ}\text{--}5^{\circ}\text{C}$  (Sievers and Emery, 1978), fluctuates greatly in structure and position, hence affecting the width and composition of the APFZ. During the early sections (9609; 9611; 9701) the SAF lies near  $55^{\circ}\text{S}$ . The APFZ is characterised by several temperature inversions occurring throughout the upper layer, just south of the SAF. During 9609 a cold core feature is found near  $56^{\circ}\text{S}$ , which may be either a meander or eddy of the jet of eastward water associated with the PF. The scale of the feature is about 50 km, and is captured by 6 temperature profiles. This highlights the need for closely spaced XBT measurements. With summer warming (9702) of the surface layers to the north, the SAF has migrated southwards towards the PF, narrowing the APFZ. Multiple inversions are still found in the APFZ. The two sections in April, separated by little more than a week, illustrate how rapidly the character and position of the SAF can change. In 9705 the SAF is expressed by a weaker temperature gradient and is further northward compared to 9704. This note has examined time and space variability in the major Southern Ocean fronts across Drake Passage using the temperature structure from six recent XBT/XCTD sections. The closely spaced XBT profiles provide a relatively inexpensive means for monitoring changes in the structure and features of Drake Passage. Additional surveys will enable us to better define the seasonal and year-to-year variability within the passage. Future work will determine a representative structure function between the temperature measurements and dynamic height as determined from recent CTD sections across Drake Passage (e.g. WOCE repeat hydrography section SR1), to infer the surface geostrophic transport associated with the strength and variability of the frontal features, and the associated heat transport.

## References

- Botnikov, V. N., 1963: Geographical position of the Antarctic Convergence zone in the Southern Ocean. Information of the Soviet Antarctic Expedition, 41, 324.
- Sievers, H. A., and W. J. Emery, 1978: Variability of the Antarctic Polar Frontal Zone in the Drake Passage – Summer 1976–1977. *J. Geophys. Res.*, 83, 3010–3022.
- White, W. B., and R. G. Peterson, 1996: An Antarctic circumpolar wave in surface pressure, wind, temperature, and sea-ice extent. *Nature*, 380, 699–702.

## Global Directory of Marine Science Institutions and Scientists (GLODIR)

The GLODIR database contains information on scientists and their scientific interests. The system allows individual scientists to submit (and in future update) information on their scientific activities to enable the marine science community and policy makers to easily identify experts in subjects of their interest. Input is collected on-line, and members of projects, programmes and organisations are invited to input their details.

You can visit the Global Directory search page on:

<http://www.unesco.org/ioc/isisdb/html/glodsearch.htm>

Please input your details onto the on-line input form at:

<http://www.unesco.org/ioc/isisdb/html/glod.htm>

# What Drives Mid-Latitude Convection and the Formation of Subantarctic Mode Water?

Joachim Ribbe, JISAO, University of Washington.  
ribbe@atmos.washington.edu



## Background

During the July WOCE Southern Ocean Workshop in Hobart, the formation of Subantarctic Mode Water (SAMW) and Antarctic Intermediate Water (AAIW) was one of the many topics discussed in detail. One issue that was particularly emphasised, was the likely role of northward-directed Ekman transport across the path of the Antarctic Circumpolar Current (ACC) and a possible contribution made by Antarctic-origin surface water to SAMW characteristics. Rintoul and Bullister (1997) reported some evidence of this contribution along the north-south WOCE SR3 repeat section between Hobart and Antarctica. A northward-directed Ekman transport of Antarctic-origin surface water is likely to explain the local freshening of the mixed layer observed north of the Subantarctic Front (SAF).

The role of northward-directed wind-driven transport of Antarctic-origin surface water across the path of the ACC on the formation process of SAMW has been questioned since McCartney (1977, 1982) reviewed the large scale distribution and formation of mode water. Any cross-frontal exchanges are ruled out and the formation occurs localised in the south-east Indian and Pacific Ocean. In contrast, Piola and Georgi (1982) agree with Sverdrup's et al. (1942) original idea in which SAMW and AAIW formation is considered a circumpolar occurring event.

In addition to recent WOCE observations, further insight into the probable role of Ekman Antarctic-origin surface water transport may be gained from the application of ocean general circulation models (OGCM). In England's et al. (1993) model for example, mid-latitude convection regions are correlated with regions of mid-latitude heat loss. Those overlap with SAMW formation regions and coincide with a region identified as the AAIW formation site in the extreme south-east Pacific Ocean. The findings support primarily McCartney's (1977, 1982) formation concept, although England et al. (1993) imply a likely role of Ekman surface layer transport on SAMW and AAIW temperature and salinity characteristics.

In a diagnosis of the mid-latitude ventilation process carried out for a high resolving OGCM of the Southern Ocean, Ribbe and Tomczak (1997) proposed that SAMW characteristics may indeed be determined by cross-frontal northward directed surface water transport in the Ekman layer. Furthermore, Ribbe and Tomczak (1997) proposed that in addition to determining water mass characteristics, wind-driven northward directed transport of cold and fresh Antarctic-origin surface water may also drive mid-latitude convection. This is in addition to the correlation identified by England et al. (1993) and others since.

In light of these recent discussions, and in particular those conducted during the WOCE Southern Ocean Workshop, it is the intent of this note to report briefly some results obtained from several numerical experiments (see for further details: Ribbe, 1997). These were conducted to investigate Ribbe and Tomczak's (1997) proposal further and reveal the likely role of Ekman transport in driving mid-latitude convection. No quantification of the underlying mechanisms has been attempted to-date.

Within the OGCM applied in this study, two mechanisms are diagnosed (Fig. 1). These lead to buoyancy losses in the surface layer and mid-latitude convection as an adjustment process. Firstly, subtropical-origin surface water advected with the subtropical gyre scale circulation into the higher latitudes (dotted line) loses heat along its eastward path across the ocean (Fig. 1). This results in density instabilities and mid-latitude convection (hatched area). Secondly, northward-directed Ekman transport (solid arrows) of Antarctic-origin surface water across the path of the ACC results in temperature and salinity anomalies. Cold and fresh surface water is advected northward upon less denser sub-surface water. The resulting density instabilities to the north of the Antarctic zone are compensated also by mid-latitude convection. It is the conclusion that SAMW is formed as a result of these mechanisms in the real ocean.

In the following sections, some of the computational results are represented which lead to this new mode water formation concept. Results are shown only for the South Indian Ocean basin of the model. Further details about this particular study, the model employed, and all experiments, can be found in Ribbe (1997).

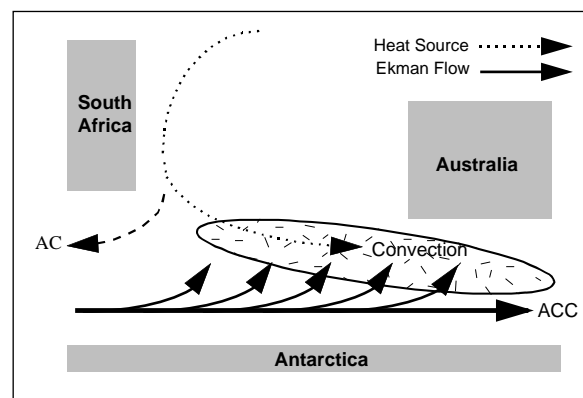
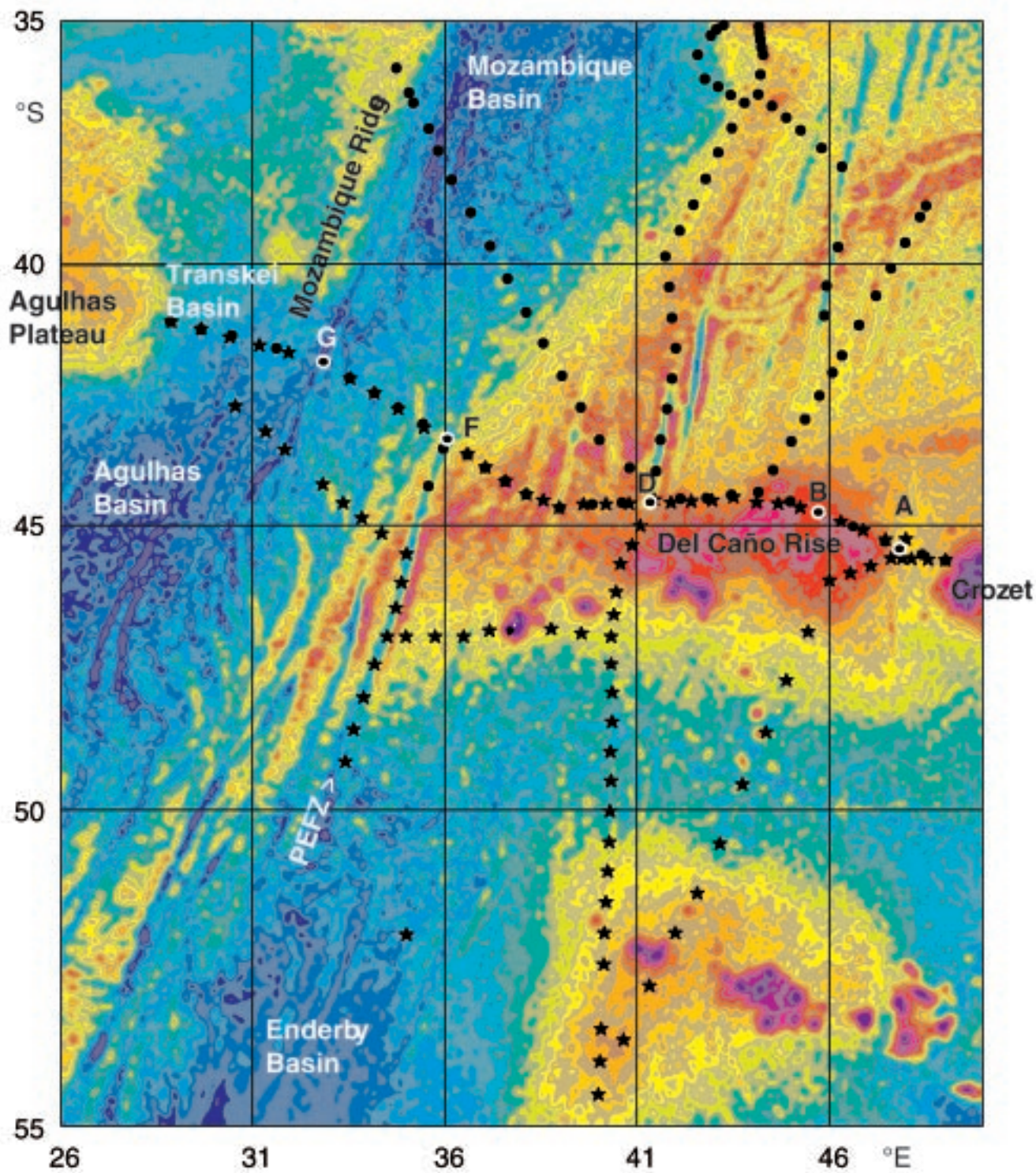
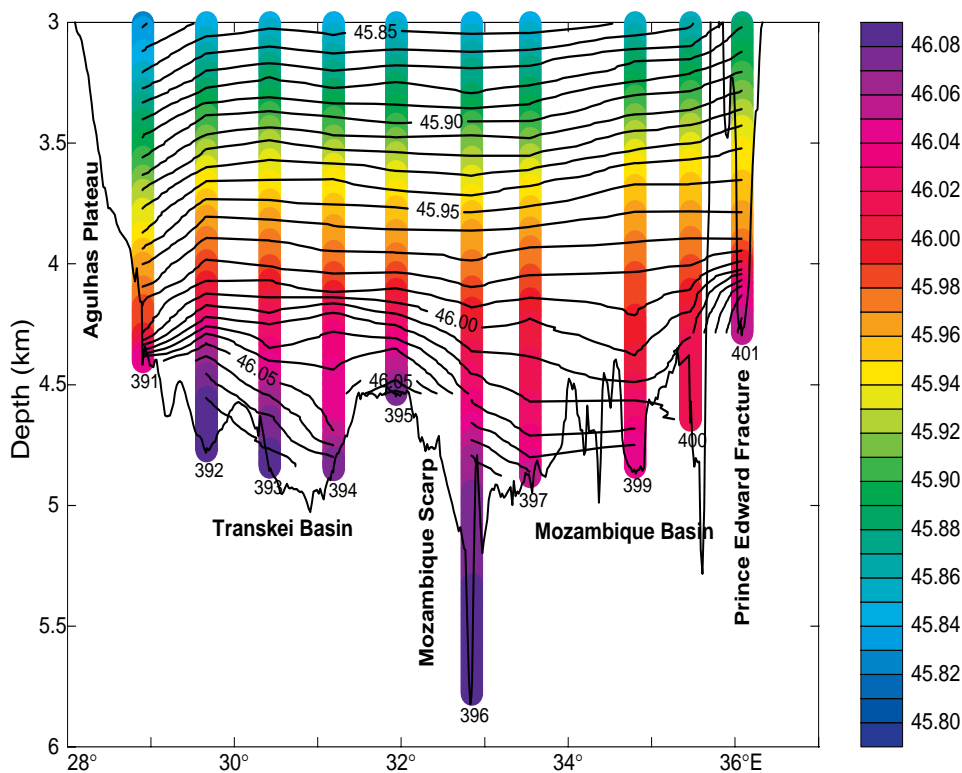


Figure 1. A schematic of the surface circulation presenting the main features which contribute to the generation of mid-latitude convection within in OGCM.



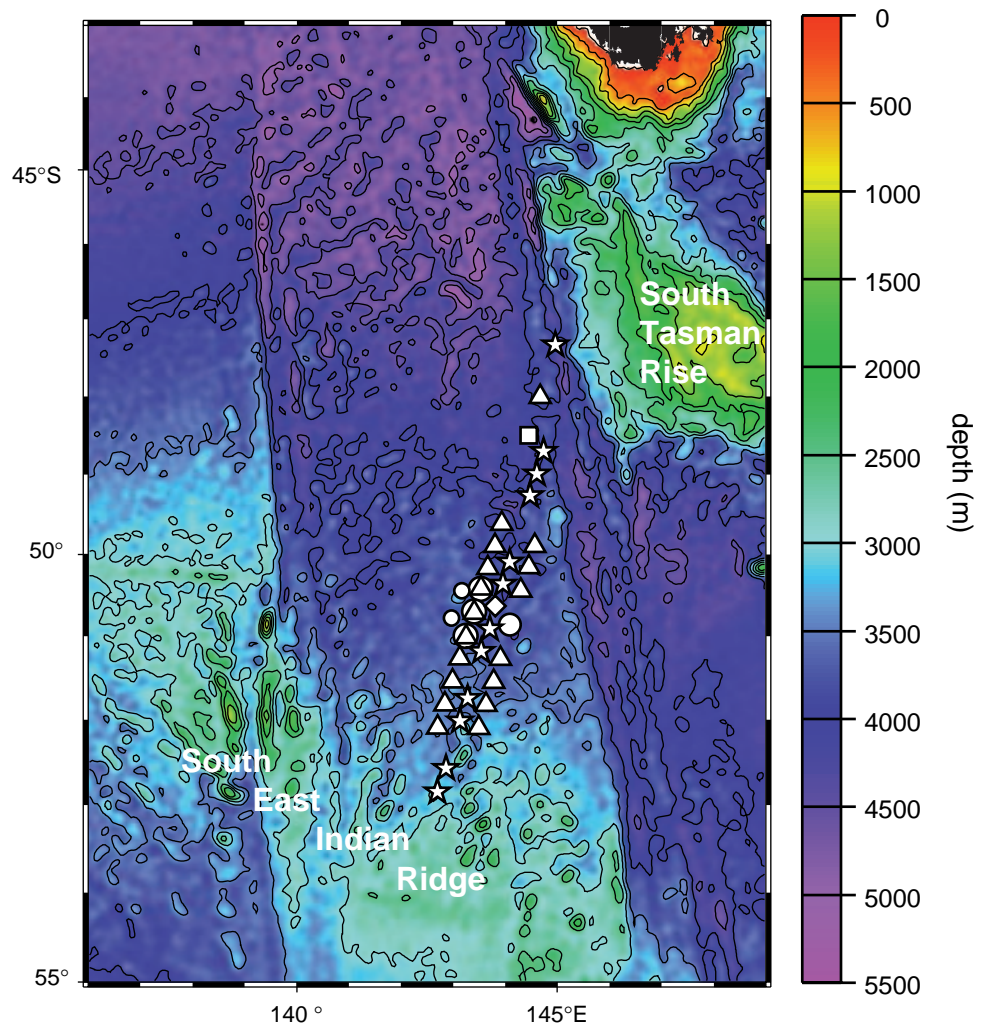


Pollard and Read, page 3, Figure 1. CTD stations occupied in 1993 (black stars) and 1995 (black dots) and moorings (white circles) are shown superimposed on the predicted topography of Smith and Sandwell (1994, 1997). Colour changes occur every 200 m. The clear change from yellow-green to green-blue occurs at 4000 m. Pure yellow spans 3200–3400 m.

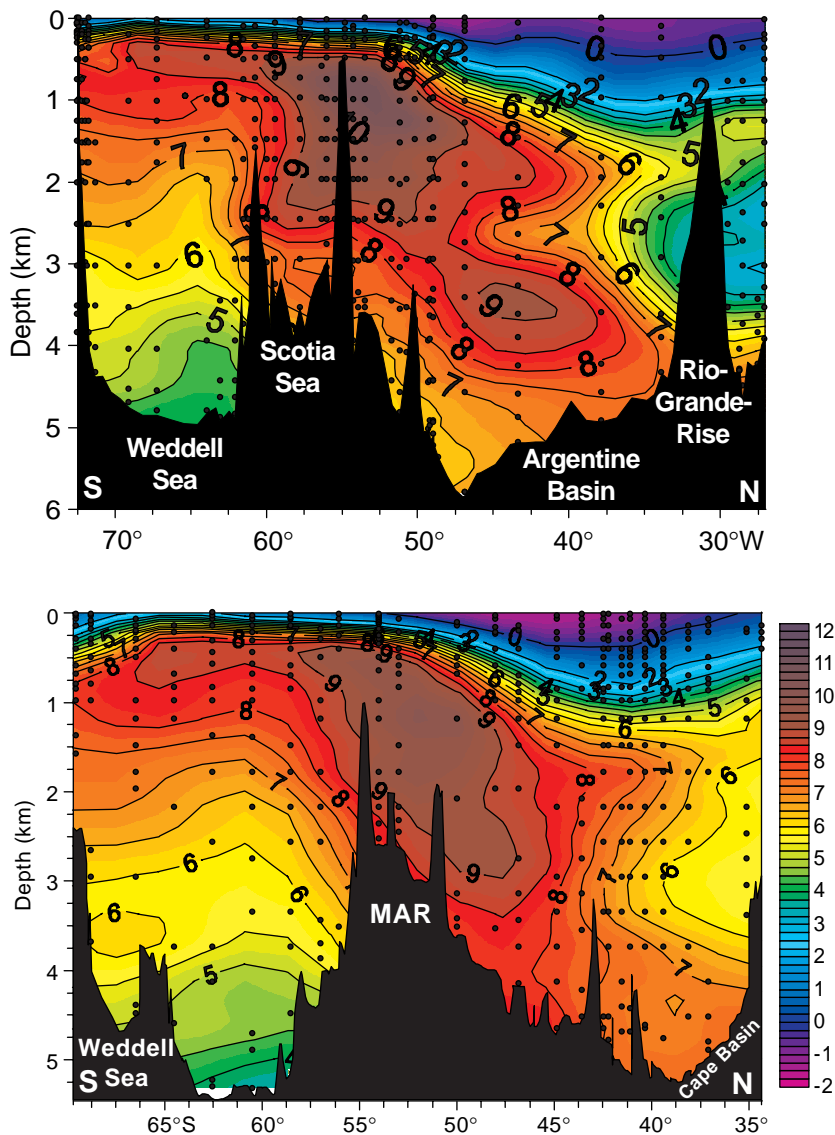


**Read and Pollard, page 7, Figure 2.** Density referenced to 4000 m across the Agulhas Basin in 1993. Data from every 10 m are coloured according to the value, line contours and depth profile are overlaid.

**Luther, page 32, Figure 1.** Locations of most of the recovered SAFDE instruments, overlaid on Smith and Sandwell (1994) topography. Triangles are inverted echo sounders; stars are horizontal electro-meters; large (small) circles are full (partial) moorings; the diamond indicates coincident electrometer and partial mooring; and, the square is a pressure recorder. All locations shown yielded full two-year records, except the pressure gauge which had a one-year record.



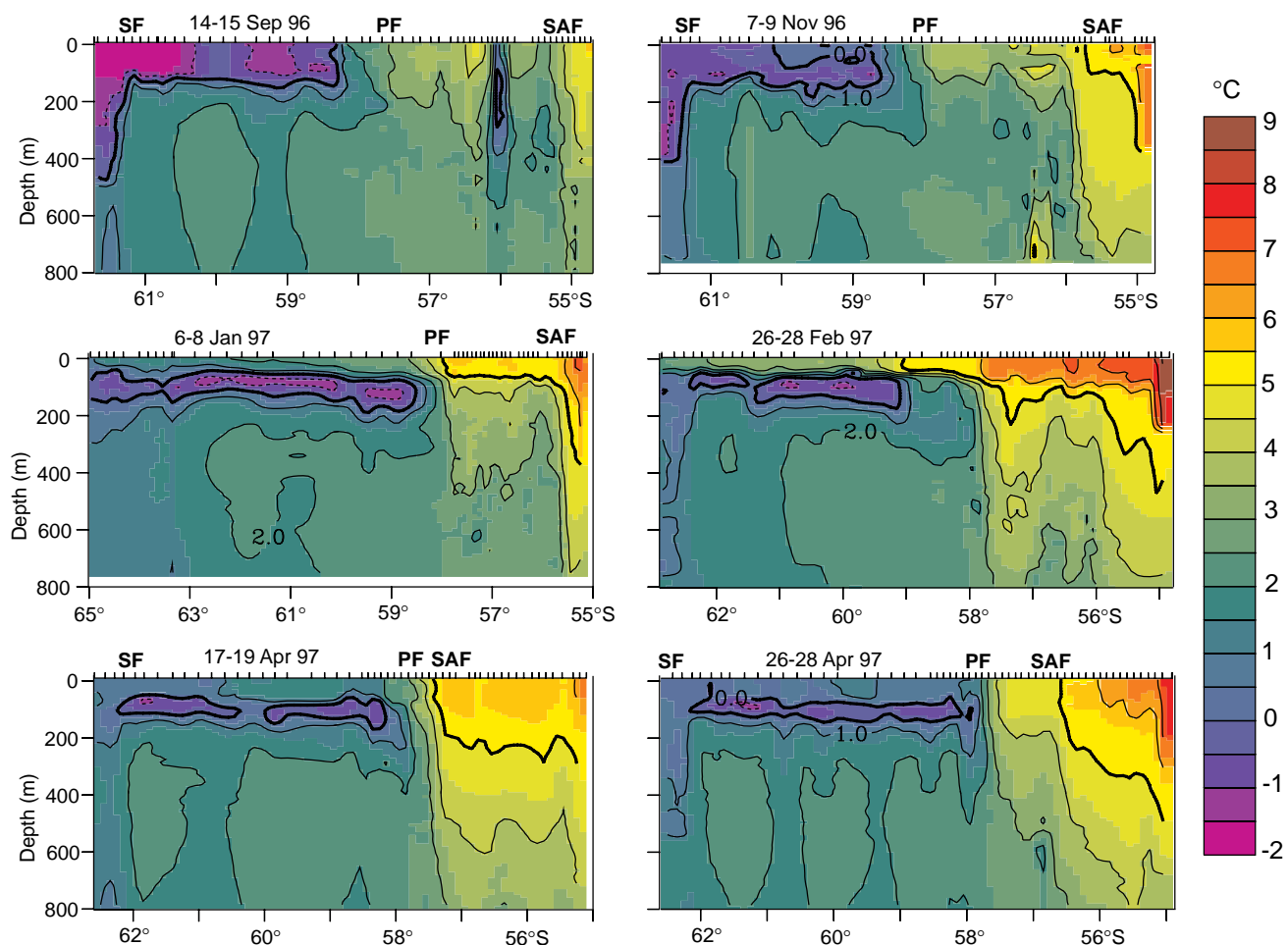




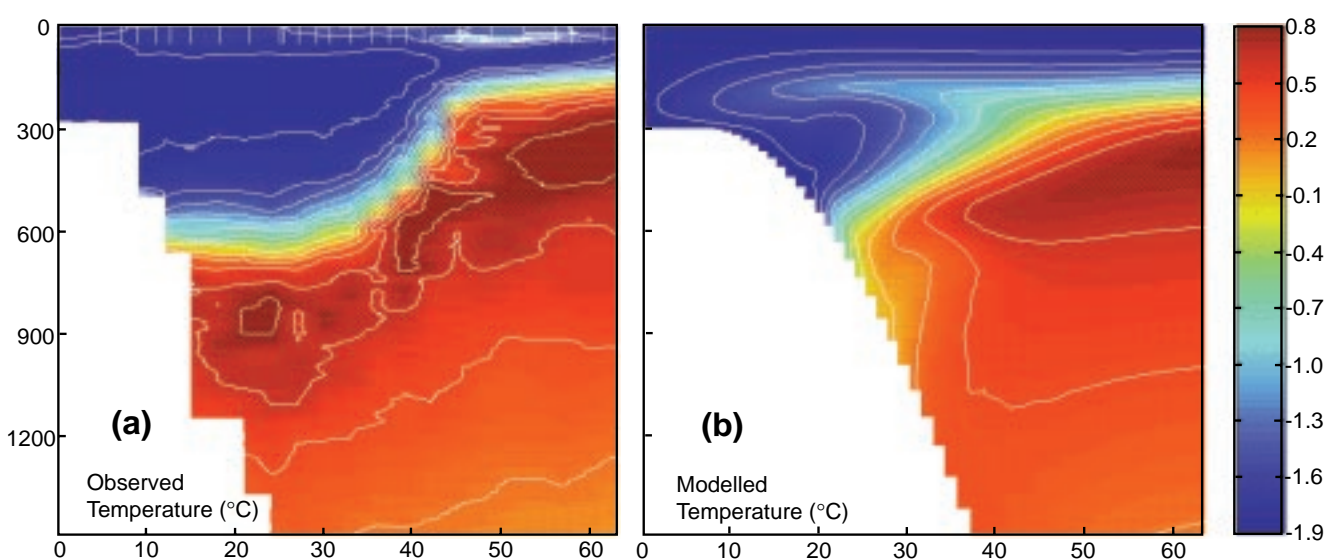
Rüth et al., page 11, Figure 2.  $^3\text{He}$  section for WHPA23 (30°W) (a), and WHP SR2 (Greenwich Meridian) (b). Values are given in  $\delta^3\text{He}$  (in percent), which is the deviation of the  $^3\text{He}/^4\text{He}$  ratio in the sample from that in air.



Garcia et al., page 16, Figure 3. AVHRR image of the Scotia Sea acquired by NOAA-12 on 14 February at 10.06 GMT (kindly provided by UCSD's AARC). Red means warm and blue means cold. Cloud are masked in black. The image projection is orthogonal, being the coordinates of the left upper corner 53°33'S, 73°29'W and of the right lower corner 62°29'S, 48°32'W.



**Sprintall et al., page 18, Figure 2.** Temperature sections from 6 XBT cruises across Drake Passage. The date, station positions, and location of the ACC Southern Front (SF), Polar Front (PF), and the Subantarctic Front (SAF) during each cruise are noted on the top axis.



**Nøst, page 42, Figure 2.** (a) shows a CTD section across the slope at 16°W. The vertical lines at the top of the figure show station positions. (b) shows the modelled temperature field. On shore Ekman transport are inducing downwelling at the coast.



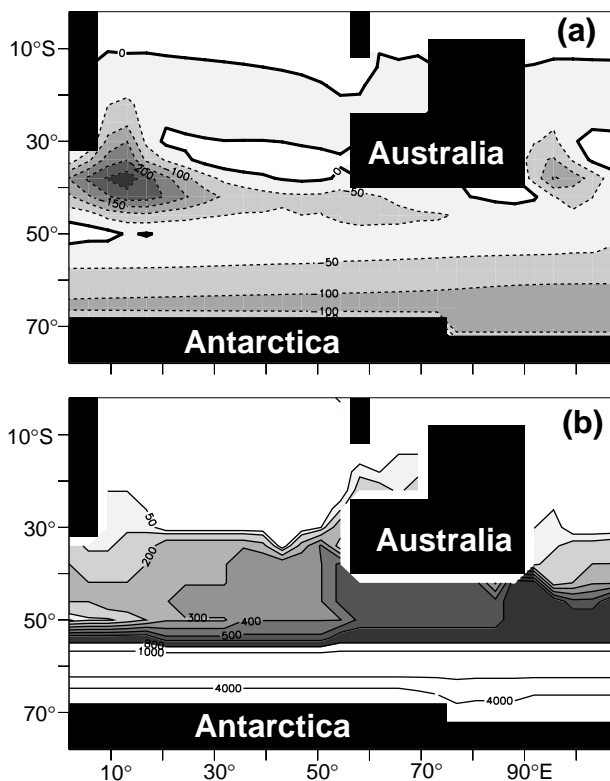


Figure 2. Control experiment: (a) Surface Heat flux [ $\text{Wm}^{-2}$ ]. Regions of heat loss are shaded; (b) depth of convection [m]. Contours: 50, 100, 200, 300, 400, 500, 600, 800, 1000, 2000, and 4000 m. Mid-latitude convective regions are shaded.

## Experiments and results

Four series of computational experiments with an OGCM were conducted to identify the correlation between surface heat flux, northward directed Ekman transport, and mid-latitude convection (Ribbe, 1997). The model is similar to that used by Cox (1989) employing almost identical idealised topography. Surface heat and freshwater fluxes are parameterised by conventionally restoring (Haney, 1971) the modelled temperature and salinity to the observed equilibrium values (Levitus, 1982).

Only results from two experiments are briefly discussed here. Experiment 1 is referred to as the control experiment. With Hellerman and Rosenstein (1983) winds and a restoring time scale of 50 days, the model was integrated until it approaches a state of equilibrium. The final property distribution of this control experiment was used to initialise the model in an enhanced wind experiment, to demonstrate the effect of an increased Ekman transport upon the depth of convection. In this case, the model was integrated for 10 years only. The restoring time scale is also chosen with 50 days. This is in contrast to the computations reported by Ribbe (1997) which employed in all experiments different restoring time scales varying between 150, 75, 25, and 10 days. In this way, it was possible to control the advection of heat within the surface layer. No results from this series of experiments is shown. But it should be noted,

that with a decreased advection of heat, the effect of an enhanced Ekman transport upon the depth of convection becomes increasingly evident with a shortening of the restoring time scale.

## Control Experiment

Surface heat losses are at a maximum in the western boundary current region of the South Indian Ocean basin and in proximity to the Antarctic continent (Fig. 2a; shaded domain). A band of heat loss above  $50\text{m/s}^2$  extends eastward. These surface heat losses drive mid-latitude convection, which to the north of the Antarctic zone extends to depths of about 800 m (Fig. 2b; shaded domain). The model exhibits several deficiencies which have been discussed in the literature previously (e.g. England et al., 1993). One example is unrealistic convection in the proximity of the Antarctic continent (Fig. 2b, non-shaded domain). The sub-surface density stratification in this region is only weak and small heat losses allow the water column to be convectively mixed almost completely. In contrast, the ocean is highly stratified in regions of mid-latitude convection north of about  $50^\circ\text{S}$  which limits the depth of convection to about 800 m. It is the region between about  $30^\circ$ – $50^\circ\text{S}$  which is of interest in this note. This area is separated from the convection region of the higher latitudes by a minimum in surface heat flux between about  $50$ – $60^\circ\text{S}$  (Fig. 2a).

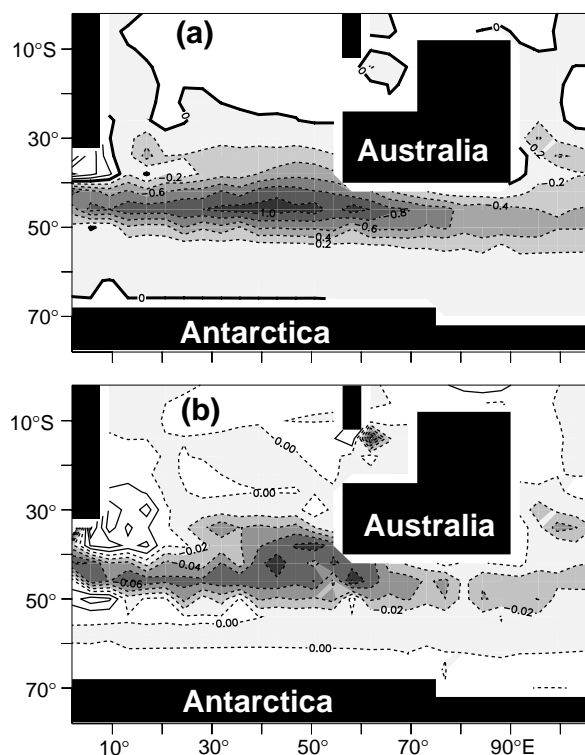


Figure 3. Enhanced wind experiment surface anomalies [positive anomalies are shaded]: (a) Temperature, contour interval is  $0.2^\circ\text{C}$ ; (b) Salinity, contour interval is 0.02. Anomalies are computed as difference between enhanced wind and control experiment data.

## Enhanced Wind Experiment

The enhanced wind stress results in an increased Ekman transport in the model surface layer, which in turn leads to surface temperature and salinity anomalies (Fig. 3). Due to the northward advection of cold and fresh water, these are negative and largest in the south-east Indian Ocean basin. That is, the control experiment is characterised by warmer and saltier surface water in the mid-latitude regions. These temperature and salinity anomalies result in density instabilities, loss of buoyancy in the surface layer and mid-latitude convection (Fig. 4b). A distinct deepening of the convectively-mixed layer is found due to enhanced wind forcing and increased northward directed Ekman transport north of about 50°S. A deepening is especially evident in the south-east of the Indian Ocean and south of Australia.

The effect of an Ekman driven deepening of the convectively mixed layer is likely to be weakened for two reasons. Firstly, the mid-latitude heat loss is reduced (Fig. 4a) which results in shallower convective mixing (compare to Fig. 2a; also see Ribbe, 1997). Secondly, the enhanced northward transport of freshwater produces positive buoyancy which reduces the depth of convection. Despite those two effects, the overall outcome is an increase in the depth of convection. It should be noted that by using a shorter temperature restoring time scale, the effect of wind driven mid-latitude convection becomes more distinct. In this case, the depth of mid-latitude convection increases

from about 300 to 500 m in the south-east Indian Ocean basin (see Ribbe, 1997).

## Conclusion

The reported results of several OGCM experiments provide us with some new insight into the mid-latitude convection process. Firstly, the experiments demonstrate that in addition to the correlation between heat loss and convection, northward directed Ekman transport of cold and fresh water across the path of the ACC results in mid-latitude convection within an OGCM. Secondly, northward directed Ekman transport results in a freshening of the convectively mixed layer in the south-east Indian Ocean. The OGCM results may lead to the conclusion that similar processes are likely to be observed in the real ocean and may contribute to the formation of SAMW. It has not been attempted in these experiments to simulate the exact water mass characteristics. The model would fail in this regard as many of the assumptions made lead to an over-simplification of the real ocean. Nevertheless, the model allowed to clearly identify the physical mechanisms which force mid-latitude convection in an OGCM. Future OGCM studies need not only to verify exact SAMW and AAIW characteristics, but test the sensitivity of the results to parameterisations such as sub-grid scale motion and convection schemes.

## References

- Cox, M. D., 1989: An idealized model of the world ocean. Part I: the global-scale water masses. *J. Phys. Oceanogr.*, 19 (11), 1730–1752.
- England, M. H., J. S. Godfrey, A. C. Hirst, and M. Tomczak, 1993: The Mechanism for Antarctic Intermediate Water Renewal in a World Ocean Model. *J. Phys. Oceanogr.*, 23(7), 1553–1560.
- Haney, R. L., 1971: Surface Thermal Boundary Condition for Ocean Circulation Models. *J. Phys. Oceanogr.*, 1(4), 241–248.
- Hellerman, S., and M. Rosenstein, 1983: Normal monthly wind stress over the world ocean with error estimates. *J. Phys. Oceanogr.*, 13(7), 1093–1104.
- Levitus, S., 1982: Climatological Atlas of the World Ocean. National Oceanic and Atmospheric Administration, 173 pp. and 17 microfiche.
- McCartney, M. S. 1977: Subantarctic Mode Water. In: *A Voyage of Discovery: George Deacon 70th Anniversary Volume*, edited by M. V. Angel, Deep-Sea Res. Suppl., pp.103–119, Pergamon Press.
- McCartney, M. S., 1982: The subtropical recirculation of Mode Waters. *J. Mar. Res. Suppl.*, 40, 427–464.
- Piola, A., and D. T. Georgi, 1992: Circumpolar properties of Antarctic Intermediate Water and Subantarctic Mode Water. *Deep-Sea Res.*, 29(6a), 687–711.
- Ribbe, J., 1997: Southern Ocean Ventilation by Mid-latitude Convection. *J. Phys. Oceanogr.* Submitted.
- Ribbe, J., and M. Tomczak, 1997: On Convection, Subduction and the formation of Subantarctic Mode Water in the Fine Resolution Antarctic Model - FRAM. *J. Mar. Systems*, 13, 137–154.
- Rintoul, S. R., and J. L. Bullister, 1997: A Late Winter Hydrographic Section from Tasmania to Antarctica. *Deep-Sea Res.*, In press.
- Sverdrup, H. U., M. W. Johnson, and R. H. Fleming, 1942: *The Oceans: Their Physics, Chemistry and General Biology*. Prentice Hall, 1087 pp.

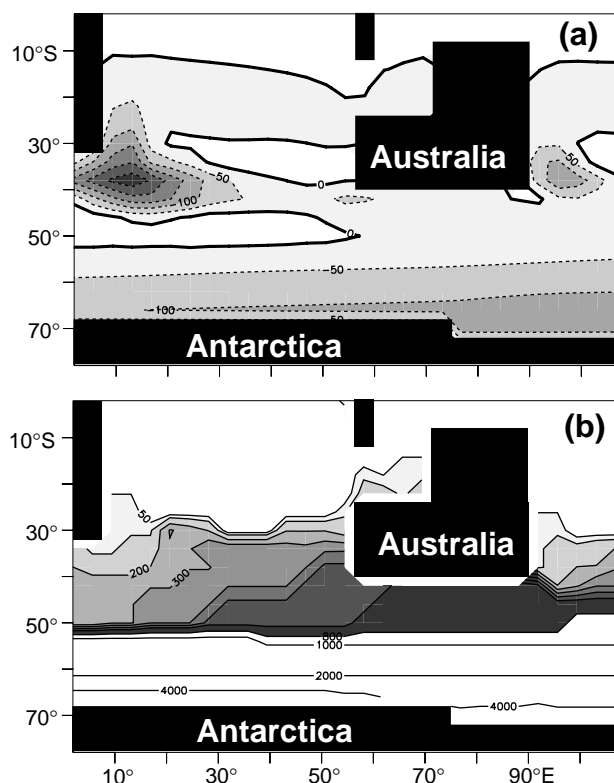
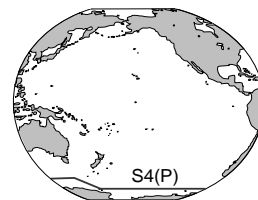


Figure 4. Enhanced wind experiment: surface heat flux and depth of convection as shown in Fig. 2.

# On the Climatic Variability of Deep Waters in the Pacific Antarctic

Alexander Yu. Goldin and Mikhail N. Koshlyakov, P. Shirshov Institute of Oceanology, Moscow, Russia. [koshl@stream.sio.rssi.ru](mailto:koshl@stream.sio.rssi.ru)



Climatic variability of deep and bottom waters in the eastern part of Pacific Antarctic is studied in this article by comparing climatic and recent hydrographic data. CTD data from the WOCE section S4 Pacific (S4P) (Fig. 1), carried out in February–March 1992 along 67°S (Koshlyakov, 1994), are used as the recent data. The data set from the “Hydrographic Atlas of Southern Ocean” (Olbers et al., 1992) is used as the climatic data. The latter data set consists of mean (“climatic”) values of potential temperature  $\theta$  and salinity  $S$  at 42 levels for every integer value of latitude  $\phi$  and longitude  $\lambda$  in the Southern Ocean.

Area under study is limited by 62.5° and 69.5°S in the southern part of quasizonal Antarctic Circumpolar Current between South Polar Front and Antarctic Continental Slope (Fig. 1). This area includes 27 stations from the S4P and 286 grid points of the climatic data set. Climatic  $\theta$  and  $S$  values at these 286 points were obtained by the optimal interpolation of  $\theta/S$  data from 350 historical stations performed in the eastern Pacific Antarctic from the early thirties to the middle of eighties (Olbers et al., 1992).

First of all the vertical distributions of  $\theta$  and  $S$  at the S4P station points were smoothed for the elimination of microstructure. The values obtained in that way were then selected for the levels of the climatic data set. As a result

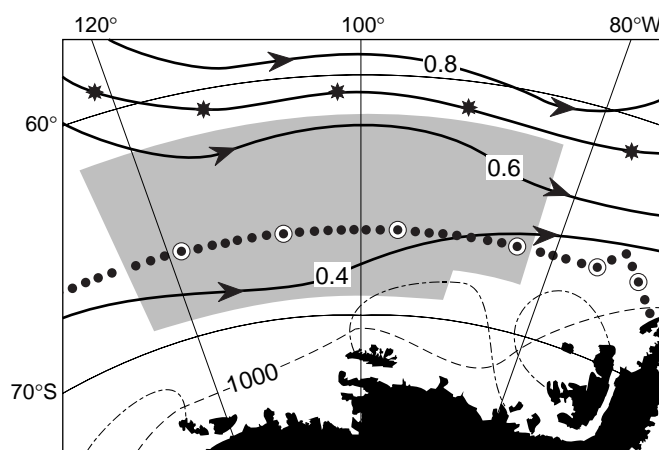


Figure 1. Location of the area under study. Dots indicate stations of the WOCE S4 Pacific section, dots in circles – with additional biological work. Solid lines with arrows are stream lines of the mean surface geostrophic current (Gordon and Molinelli, 1982), line with asterisks – mean position of the South Polar Front. Dashed and dashed-dotted lines show the 1000 m isobath and mean position of sea ice edge in March 1992 respectively.

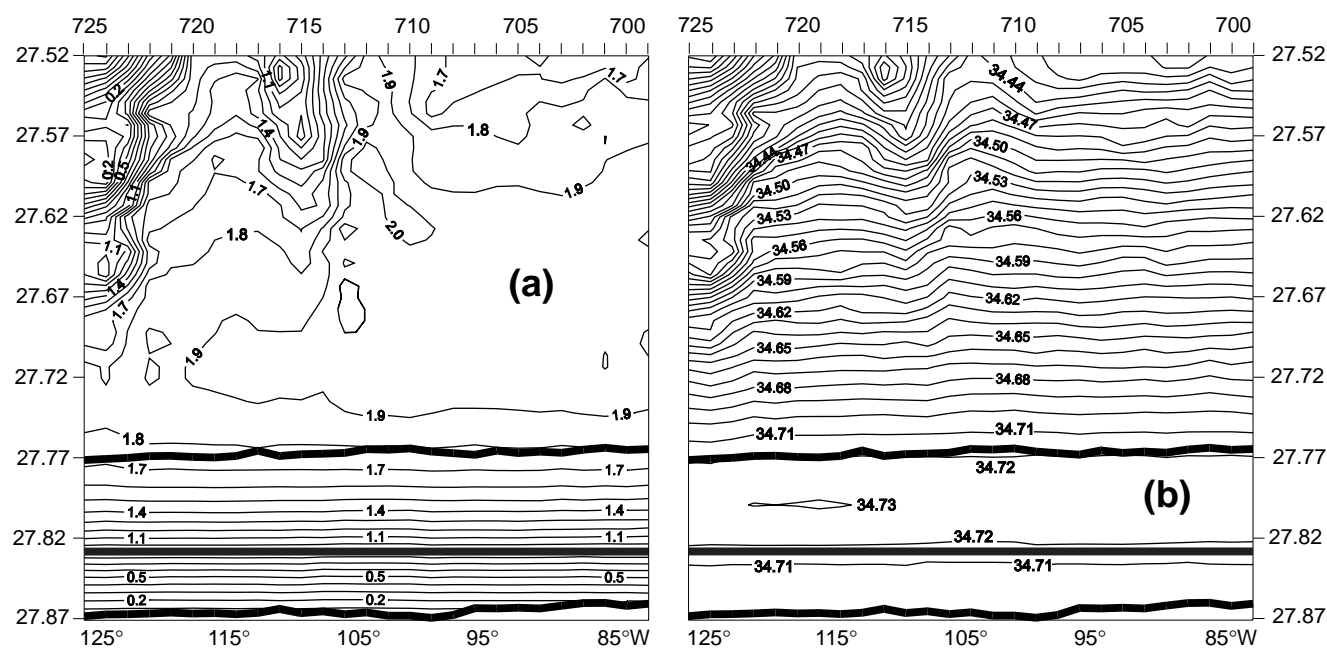


Figure 2. Potential temperature (°C, a) and salinity  $S$  (psu, b) on the deep part of section S4 Pacific on the coordinates western longitude – potential density. Heavy lines indicate the upper and lower boundaries of Lower Antarctic Circumpolar Deep Water and the ocean bottom. Stations position and numbers are shown at the upper edge of the figure.

two data sets – climatic and recent – were obtained for the same ocean levels and then analysed for the ocean climatic variability.

The following water masses are observed in the area under study (Patterson, Whitworth, 1990):

- Antarctic Surface Water with the local minimum of  $\theta$  and  $S$ ;
- Upper Antarctic Circumpolar Deep Water (UAACDW) with the local maximum of  $\theta$ ;
- Lower Antarctic Circumpolar Deep Water (LAACDW) with the local maximum of  $S$ ;
- Antarctic Bottom Water (AABW) with the local minimum of  $\theta$  and  $S$ .

The latter three water masses are clearly visible in Fig. 2. For the analysis of variability of the water mass parameters, it is necessary to fix boundaries between these water masses. For every S4P station and every grid point of the climatic data set, UAACDW/LAACDW boundary was defined as the value of  $\sigma_\theta$  for which vertical increments of  $\theta$  and  $S$  give an equal contribution to the vertical increment of  $\sigma_\theta$  (Fig. 2). These boundary values of  $\sigma_\theta$  were computed by  $\theta$ ,  $S$  and  $\sigma_\theta$  values at three successive levels of the climatic data set.

The LAACDW/AABW boundary was defined as the value of  $\sigma_\theta$  for which gradient  $|dS/d\sigma_\theta|$  reaches its maximum (Fig. 2). In this case boundary values of  $\sigma_\theta$  were computed by  $S$  and  $\sigma_\theta$  values at four successive levels of the climatic data set.

The lower boundary of AABW (“ocean bottom”) was searched only for 66°, 67° and 68°S as an independent of  $\varphi$  feature. For every value of  $\lambda$  this boundary was defined as the uppermost of the three (for 66°, 67° and 68°S) deepest levels of the climatic data set.

The next step of analysis was the plotting of the  $\theta$ ,  $S$  and  $\sigma_\theta$  zonal distributions for the LAACDW and AABW as a whole (mean values of  $\theta$ ,  $S$  and  $\sigma_\theta$  from the upper to the lower boundary of each water mass were plotted in this case), for the cores of UAACDW and LAACDW, for the boundaries between UAACDW, LAACDW and AABW, and for the ocean bottom. These graphs were plotted for 63° to 69°S (66°, 67° and 68°S for the AABW and ocean bottom) by the climatic data and for 67°S by the S4P data. As a result of this plotting, 82 outliers in the  $\theta$ ,  $S$  and  $\sigma_\theta$  zonal runs were eliminated, that is 2.2% of all the  $\theta$ ,  $S$  and  $\sigma_\theta$  values under analysis.

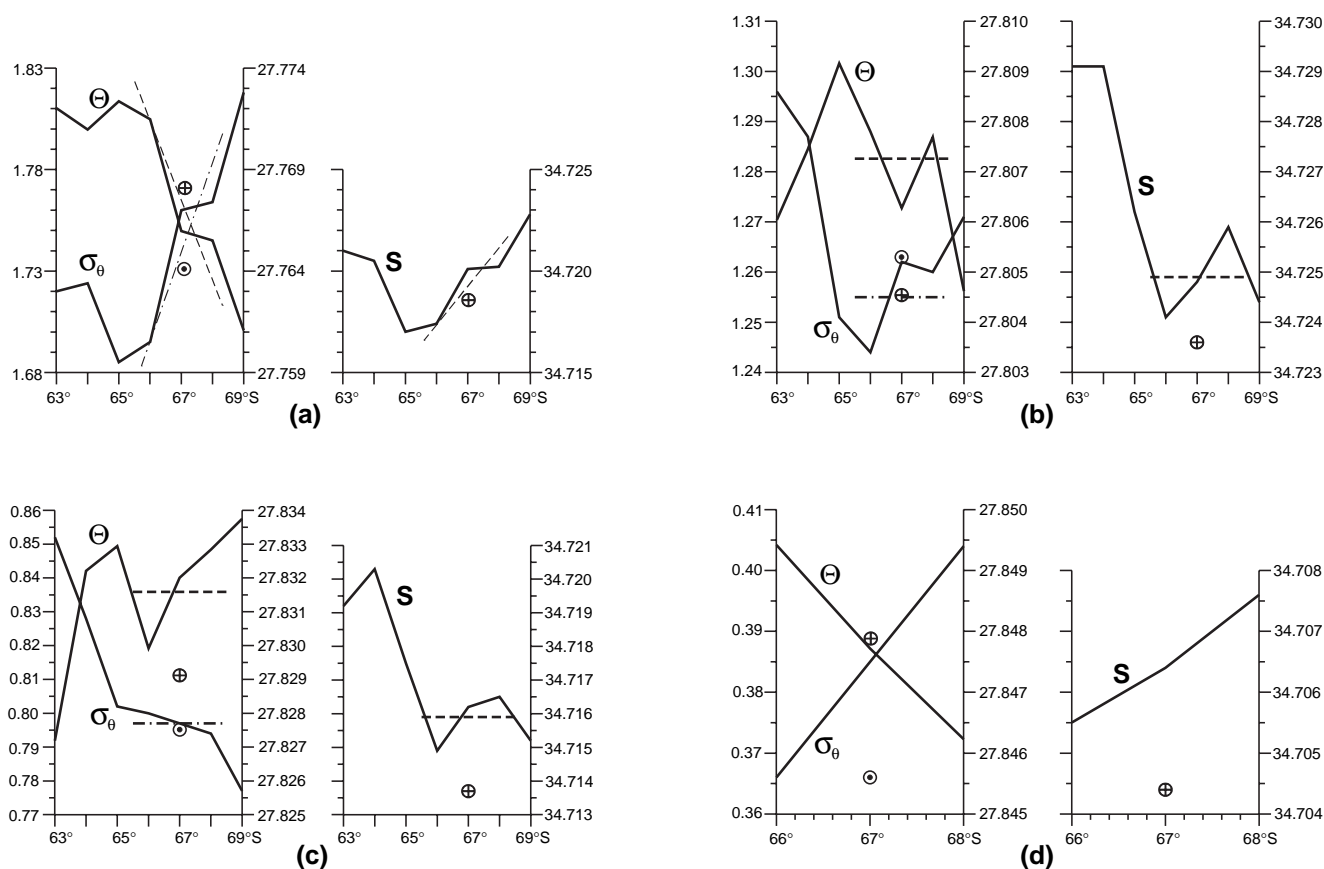


Figure 3. Meridional distribution of averaged potential temperature  $\theta$  (°C), salinity  $S$  (psu) and potential density  $\sigma_\theta$  according to climatic data: (a) for the upper boundary of Lower Antarctic Circumpolar Water (LAACDW), zonal averaging; (b) for the LAACDW, averaging over the vertical zonal section between the upper and lower boundaries of LAACDW; (c) for the lower boundary of LAACDW, zonal averaging; (d) for the Antarctic Bottom Water, averaging over the vertical zonal section between the lower boundary of LAACDW and ocean bottom. Circles with crosses (dots) indicate similar averaged values of  $\theta$  and  $S$  ( $\sigma_\theta$ ) according to the S4 Pacific data. Dashed (dashed-dotted) lines show the approximation of the climatic distributions of  $\theta$  and  $S$  ( $\sigma_\theta$ ) in the interval 65°30'–68°30'S.



Because all the zonal distributions of  $\sigma_\theta$  for the lower boundary of LAACDW turned out to be oscillating near some constant values of  $\sigma_\theta$ , these values were applied to this boundary. On the other hand,  $\sigma_\theta$  values for the upper boundary of LAACDW were retained to be variable along longitude. The obtained position of the upper and lower boundaries of LAACDW and of the ocean bottom by S4P data are shown in Fig. 2.

The last step of analysis consisted of averaging  $\theta$ ,  $S$  and  $\sigma_\theta$  along longitude for all boundaries and layers mentioned above and drawing the meridional distributions of these averaged values for climatic and S4P data (Fig. 3). The scales for  $\theta$ ,  $S$  and  $\sigma_\theta$  in Fig. 3 were chosen to illustrate the partial  $\theta$  and  $S$  contribution to the variability of  $\sigma_\theta$ .

Fig. 3b shows our main result: the mean temperature of LAACDW according to S4P data shows a decrease of  $0.03^\circ\text{C}$  with respect to the climatic data. The fact that all the seven climatic values of  $\theta$  turned to be higher than the S4P one (Fig. 3b) supports the validity of this result. Also, S4P temperature at the lower boundary of LAACDW is  $0.025^\circ\text{C}$  less than climatic temperature at the same boundary in the area between  $66^\circ$  and  $68^\circ\text{S}$  (Fig. 3c).

LAACDW is produced by mixing North Atlantic Deep Water (NADW) with a small amount of deep water from the Weddell Sea (Patterson, Whitworth, 1990). The Weddell Sea is also the main area of AABW formation. Because mean values of  $\theta$  for AABW at  $67^\circ\text{S}$  are the same for S4P and climatic data sets (Fig. 3d), we may suppose that the LAACDW temperature decrease mentioned above is mainly induced by the temperature variations of NADW. In fact it is appropriate to mention that NADW temperature decreased by  $0.03^\circ\text{C}$  at  $24^\circ\text{N}$  from 1957 to 1992 and by  $0.04^\circ\text{C}$  at  $36^\circ\text{N}$  from 1959 to 1993 (Parrilla, 1994; Dobroliubov et al., 1996). Agreement by magnitude of this

temperature variability of NADW and of the  $\theta$  anomaly of LAACDW in 1992 (S4P data) leads to the idea of a very weak mixing of NADW/LAACDW with the surrounding waters along the entire path of this water mass from the northern North Atlantic to the eastern part of Pacific Antarctic. The fact that LAACDW conserves the main NADW characteristics – high salinity and low nutrient concentration – is also in agreement with this conclusion.

Fig. 3 shows that S4P salinity at  $67^\circ\text{S}$  is less than climatic salinity by  $0.001\text{--}0.002$  psu for all the water masses and their boundaries considered here. Taking into account information from Mantyla, 1994, it is reasonable to suppose that this salinity “anomaly” has a technical origin and can most likely be explained by the observational transfer from the brass Nansen bottles in the past to the plastic Niskin bottles at present.

## References

- Dobroliubov, S., B. Tereschenkov, and A. Sokov, 1996: Mass and heat fluxes at  $36^\circ\text{N}$  in the Atlantic: Comparison of 1993, 1981 and 1959 hydrographic surveys. Intern. WOCE Newsletter, No. 22, 34–37.
- Gordon, A. L., and E. J. Molinelli, 1982: Southern Ocean Atlas. Columbia University Press, N.Y.
- Koshlyakov, M. N., 1994: Hydrological research in the Pacific Ocean sector of Antarctica. Oceanology, English Translation, v. 33, No. 4, 549–553.
- Mantyla, A. W., 1994: The treatment of inconsistencies in Atlantic deep water salinity data. Deep-Sea Res., v. 41, No. 9, 1387–1405.
- Olbers, D., V. Gouretski, G. Seif, J. Schröter, 1992: Hydrographic Atlas of the Southern Ocean. Alfred Wegener Inst., Bremerhaven.
- Parrilla, G., 1994: WHP section A5 across  $24^\circ\text{N}$  aboard BIO “Hesperides”. International WOCE Newsletter, No. 15, p.3, 4.
- Patterson, S. L., and T. Whitworth, 1990: Physical Oceanography. In: Antarctic Sector of the Pacific, ed. G. P. Glasby, Elsevier Press, Amsterdam, 55–93.

## Subantarctic Mode Water Formation by Air-Sea Fluxes

Kevin Speer, LPO, IFREMER/CNRS, France; Steve Rintoul, CSIRO Marine Research/Antarctic CRC, Hobart, Australia; and Bernadette Sloyan, University of Tasmania, Hobart, Australia. kevin.speer@ifremer.fr



The framework for the formation of water masses in density classes by air-sea fluxes, including heat and fresh water exchange, Ekman drift, and other effects has been presented in a number of articles; an especially convenient reference here is the one by Tandon and Garrett (1997, WOCE Newsletter No. 28; see also Marshall, 1997). The approach (Walsh, 1982) combines heat and fresh water fluxes with a mass budget in isopycnal layers and leads to a relation between cross-isopycnal advection  $A$ , diapycnal diffusion  $D$ , diapycnal transfers at the base of the mixed layer, and the buoyancy forcing  $F$  on that isopycnal:

$$A_{\text{Ek}} + A_{\text{eddy}} + A_{\text{geost}} = F_{\text{air-sea}} + F_{\text{ML}} - \frac{dD_{\text{eddy}}}{db} - \frac{dD_{\text{int}}}{db}$$

where  $b$  is buoyancy (all variables are functions of buoyancy or density).  $A$  has been divided into Ekman transport, eddy-driven cross-isopycnal transport (mainly) in the surface mixed layer, and the mean geostrophic cross-isopycnal transport. Further divisions may be needed to fully represent various dynamics. The thermodynamic forcing is divided into the air-sea part, which often dominates, and several mixing terms. These terms include mixing associated with the mixed-layer depth evolution, horizontal stirring by eddies, and interior diapycnal mixing. The latter may be negligible except where layers run into rough topography.

Transformation of water from one density class to another by air-sea fluxes in the Southern Ocean provides a critical link in the global overturning circulation, and the water masses thus formed occupy a large fraction of the

world ocean volume. Therefore it is worthwhile to examine the water mass formation rates implied by our present best estimate of these fluxes, despite the fact that the fluxes are poorly known in this region. As a first step, we estimate the formation of water masses driven by air-sea heat flux and Ekman transport south of 30°S. The results show that South Atlantic Mode Water (SAMW) is mostly formed in the Indian Ocean sector, where  $25 \times 10^6 \text{ m}^3 \text{ s}^{-1}$  or 65% of the total formation occurs. Geostrophic transport estimates from an inverse model of the circulation south of 20°S suggest that about 15 Sv of the SAMW formed in the Indian Ocean sector is carried into the Pacific Ocean, while the rest recirculates within the Indian Ocean.

## Climatology and results

Perhaps the first question is whether or not anything at all can be believed about climatological air-sea fluxes in the Southern Ocean. Certainly errors are large, as the authors of climatologies are themselves quick to point out. Systematic biases are likely, especially for flux variables derived from winds, which are thought to be undersampled and underestimated. Careful flux estimates have been produced, however, from ship-based data and from model output, and it seems worthwhile to examine the consequences such fluxes – if real – would have on the ocean. Much information about diapycnal processes and perhaps eddy fluxes is implicit in the sea-surface forcing. We use the DaSilva COADS analysis (available from NODC) of monthly heat flux and SST. Surface salinity comes from the Levitus climatology. In this analysis the flux data is constrained to agree with oceanographic observations at several location, removing to some extent any global systematic bias. The COADS analysis is generally

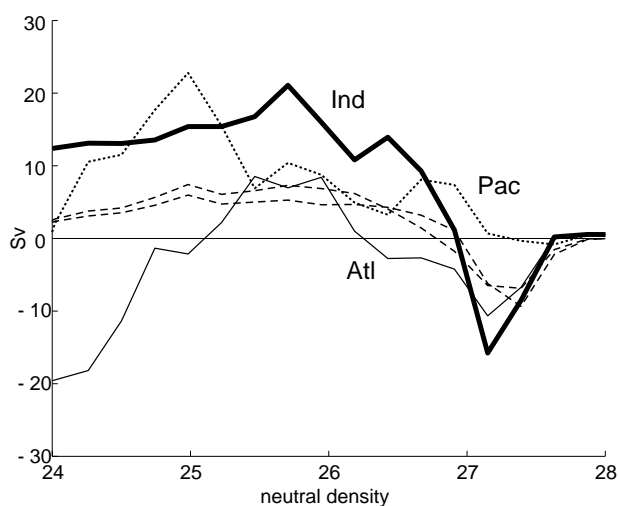


Figure 1. Transformation over the Southern Ocean (south of 30°S), divided by sector: Indian (bold), Atlantic (thin), and Pacific (dotted). Positive values mean cooling and a transfer to greater densities. Two examples of Ekman pumping are shown (dashed), from COADS and Hellerman and Rosenstein.

similar in structure to other ship-based climatologies, although biases exist between different climatologies. The model-based fluxes from ECMWF give very different results, however. The nature of these differences and ways to improve the estimates needs further study. The freshwater flux varies more dramatically between different climatologies, and is further complicated by freshwater fluxes associated with freezing and melting of sea ice. For now, we consider only the air-sea flux of heat. Ekman transports were calculated from the COADS and Hellerman and Rosenstein wind stress climatologies.

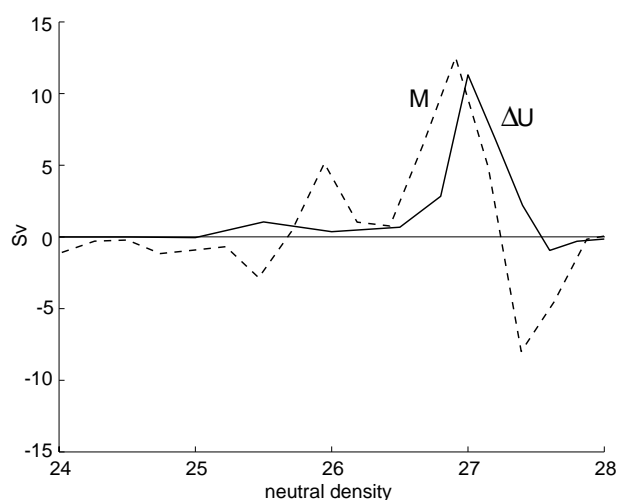


Figure 2. The derivative (centred difference) of Indian Ocean sector transformation,  $M$ , is displayed with geostrophic volume transport difference between a section south of Australia and one south of Africa, showing the augmentation of transport in mode water density classes across the Indian Ocean.

We integrate the heat flux over isopycnal outcrops and calculate the cross-isopycnal flux driven by this buoyancy source, which we call transformation,  $F_{\text{air-sea}}$ . The derivative of  $F_{\text{air-sea}}$  with respect to buoyancy gives the formation,  $M$ .

The shape of the annual average transformation curve (Fig. 1) reflects the cooling of warm water carried poleward by the western boundary currents of the subtropical gyres, heating at slightly higher latitudes (densities), followed by weak cooling again at the highest latitudes (densities). In each basin, cooling of low density water and warming of higher density water tend to converge mass in the density range of SAMW, with the transition from cooling to warming occurring at greater density as one moves east from the Atlantic. Taylor et al. (1978) noted a similar pattern in surface heat flux which they related to the transition from Ekman suction to pumping. This pattern is quite different from that over subtropical and subpolar gyres typical of northern hemisphere basins, but leads to exactly the same effect: a convergence into mode water density classes

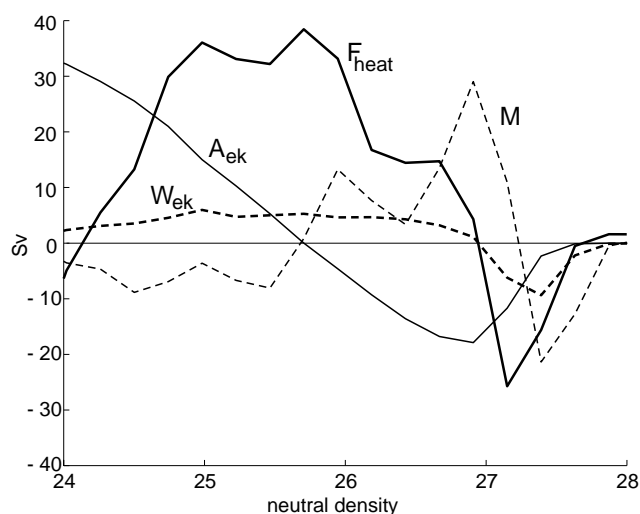


Figure 3. The full transformation curve for the Southern Ocean ( $F_{\text{heat}}$ ) and the Ekman transport ( $A_{\text{ek}}$ ) are displayed together with their derivatives formation ( $M$ ) and pumping ( $W_{\text{ek}}$ ).

driven by air-sea fluxes. Interestingly, a coupled climate model shows a similar pattern (E. Guilyardi, pers. comm.). All three sectors of the Southern Ocean contribute, with a tendency to form water masses in successively greater density classes from west to east. The dominant contributor is the Indian Ocean, with about 25 Sv converging between 26.5 and 27.3 (neutral density is slightly greater than sigma-0 at the surface).

Geostrophic transport calculations from an inverse model of the circulation south of 20°S show an excess of about 15 Sv leaving the Indian Ocean south of Australia over that entering the basin south of Africa in the SAMW density range (Fig. 2). This suggests that roughly half of the mode water formed in the Indian Ocean is exported to the Pacific, while half recirculates within the Indian subtropical gyre. Comparing the two curves in Fig. 2, it is the less dense mode waters which recirculate.

To determine if the amount of intermediate water being transformed is the same as the Ekman transport, Fig. 3 shows both  $F_{\text{heat}}$  and its derivative  $M$ , together with the Ekman transport and its derivative ( $W_{\text{ek}}$ ). In these climatologies, the two do not agree; in fact the concordance of heat flux and Ekman *pumping* means that heat flux and Ekman *transport* have different structures. Note that these conclusions hold up under various adjustments to try to resolve better the annual cycle, for instance by fixing wintertime sea-surface conditions. So while Ekman transport brings something like  $20 \times 10^6 \text{ m}^3 \text{ s}^{-1}$  north at 27, its divergence over mode water is relatively weak compared to the mass source that the heat flux can provide. Thus, an eddy or geostrophic transport divergence ( $dA_{\text{eddy}}/db$  or  $dA_{\text{geost}}/db$ ) is needed to compensate for the mismatch.

If in an approximately two-dimensional ocean the geostrophic term cancels out, the mismatch would be attributed to eddy transport. The eddy transport can only be from warm to cold (slumping), and would need to have a

magnitude of about 20 Sv to account for the difference between Ekman transport and heat flux-driven formation for densities less than 27. At higher density, the transformation is from dense to light water and is of the wrong sign to be explained by eddy transport, so some geostrophic convergence may be needed to make up the difference.

Ekman transport appears at the same order of magnitude as transformation – as expected – and provides the basic flow balancing the surface heat flux. They need not balance exactly, and the relative strength of the two will differ from one climatology to another. Hence, the role forced upon eddy fluxes, for example, will vary as well. Depending on the manner in which these eddy fluxes are parameterised in a model, the interior density field and potential vorticity will have to adjust to provide this role.

The main messages from this diagnostic of surface fluxes are that:

- (1) The air-sea heat flux distribution south of 30°S is connected to the circulation of the gyres and Ekman transport and leads to a convergence of mass in mode water density classes, as in other oceans.
- (2) Formation calculations may give some insight into the role that eddy fluxes play in the thermohaline circulation.
- (3) The Indian Ocean is the primary source of SAMW, half of which recirculates within the basin and half of which is exported to the Pacific.
- (4) The combination of air-sea fluxes with geostrophic estimates of flow is necessary to approach a description of the large-scale role of mixing processes presently operating in the ocean. Improvements in flux climatologies should therefore be a high priority for accurate climate modelling.

## References

- Marshall, D., 1997: Subduction of water masses in an eddying ocean. *J. Mar. Res.*, 55, 201–222.
- Tandon, A., and C. Garrett, 1997: Water mass formation from thermodynamics: a framework for examining compatibility with dynamics. *Int. WOCE Newsletter No. 28*.
- Taylor, H. W., A. L. Gordon, and E. Molinelli, 1978: Climatic characteristics of the Antarctic Polar Front Zone. *J. Geophys. Res.*, 83, 4572–4578.
- Walén, G., 1982: On the relation between sea-surface heat flow and thermal circulation in the ocean. *Tellus*, 34, 187–195.

## Adjoint Model Compiler

Construction of an ocean model adjoint compiler has been successfully implemented at the Max Planck Institute, Hamburg. The authors, Ralph Giering and Thomas Kaminiski - working within the WHP-SAC, have designed the code for an arbitrary ocean model and demonstrated its performance within the Hamburg LSG model.

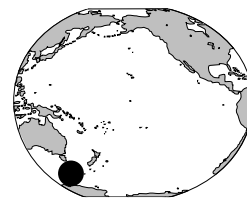
Further information from:

<http://klima47.dkrz.de/giering/tamc/tamc.html>



# The Sub-Antarctic Flux and Dynamics Experiment (SAFDE)

Douglas S. Luther, Department of Oceanography, University of Hawaii, Honolulu, USA and the SAFDE PIs\*: [dluther@foliatus.soest.hawaii.edu](mailto:dluther@foliatus.soest.hawaii.edu)



WOCE initiatives have resulted in a large increase in the number of direct measurements of the Antarctic Circumpolar Current (ACC) and its associated weaker circulation systems. There are now many more hydrographic sections, XBT sections, drifter and float tracks, and moored current and temperature measurements than were available before WOCE began (WOCE, 1997). Despite these in situ observations and the accumulation of satellite sensor measurements of sea height and sea surface temperature, the ~25,000 km long ACC remains one of the most poorly observed ocean currents.

While another call for more in situ observations of the ACC is easy to make, the reality is that logistical and cost barriers are so high that observations in the Southern Ocean will always be sparse in time and space. Advances in our knowledge of ACC dynamics must come through a synergy of models and observations. What this means for observations is that they must focus on measuring quantities, such as non-geostrophic terms of the momentum equations and terms of the vorticity equation, that can provide better discrimination of differing model assumptions and parameterisations.

The Sub-Antarctic Flux and Dynamics Experiment (SAFDE) was designed with this principle in mind, to achieve observations of the ACC south of Tasmania that would permit direct evaluation of the momentum, energy and vorticity budgets. That these budgets differ in different sectors of the Southern Ocean is as obvious as the differing bottom topographies that exert such a great influence on the ACC. The assumption of zonal invariance of the dynamics of the ACC, occasionally necessary for the development of basic dynamical concepts, must certainly be rejected in detail (see, for instance, the analysis of FRAM output by Wells and de Cuevas, 1995). One way that limited area, high-resolution observation programmes such as SAFDE can be employed in the study of the ACC's dynamics over larger regions is through comparison with, and validation of, conclusions based on satellite-derived sea surface heights; and this certainly is one of our goals. But perhaps the greatest value will be achieved when the high resolution observations are used to provide the kind of information that is most useful for discriminating the validity of differing model dynamics. Models validated with such observations would then be expected to more accurately simulate

the flow and variability in other locations of the Southern Ocean.

SAFDE observations alone are insufficient for satisfactory model validation, but prudent experiments like SAFDE, as well as thoughtful analyses of surface drifter velocities and altimeter-derived velocity components at cross-over points, will take us a long way toward that goal. A good example of a comparison of higher moment statistics derived both from a numerical model of the Southern Ocean and from various altimeter, drifter and current meter datasets can be found in Wilkin and Morrow (1994).

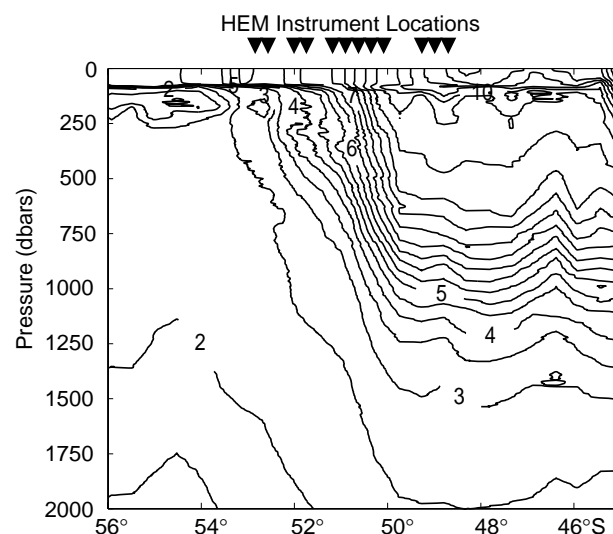


Figure 2. Section of temperature along the WOCE SR3 line in March, 1993, truncated in latitude and depth to emphasise the SAF (isotherms in °C). The locations of the horizontal electrometers (the middle row of instruments in Fig. 1) are shown to indicate the positioning of the SAFDE array relative to the SAF.

SAFDE has achieved multi-year observations of currents and temperatures in both a small current meter mooring array with a diameter of ~70 km, and along a SSW-NNE section perpendicular to the expected mean axis of the ACC at the Sub-Antarctic Front (SAF). The experiment lasted two years, from April 1995, through March 1997. The measured variables are coherent horizontally and vertically in broad, sub-inertial frequency bands. The rarity of such horizontally coherent observations, required for estimating momentum budgets, etc., is revealed by noting that when SAFDE was proposed six years ago only three locations in the ACC had been sampled with moored current meters for as long as one year, and only one location for as long as two years, with the horizontally coherent records all being no more than about a year long.

\*SAFDE PIs (alphabetically)

Alan D. Chave, Woods Hole Oceanographic Institution, USA  
John A. Church, CSIRO Marine Laboratories, Australia  
Jean H. Filloux, Scripps Institution of Oceanography, USA  
Douglas S. Luther, Univ. of Hawaii at Manoa, USA  
James G. Richman, Oregon State University, USA  
Stephen R. Rintoul, CSIRO Marine Laboratories, Australia  
D. Randolph Watts, University of Rhode Island, USA



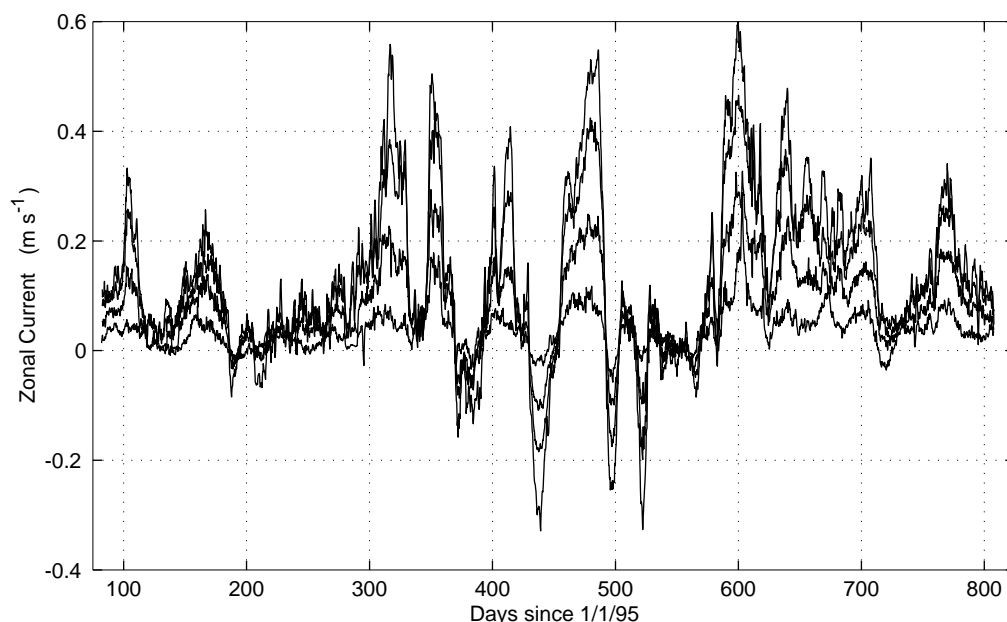


Figure 3. Zonal currents from the eastern mooring (easternmost circle in Fig. 1) at depths of 300 m, 600 m, 1000 m, and 2000 m. The 300 m current is the most energetic, then 600 m and so forth.

## Array description

Fig. 1 (page 22) displays the SAFDE array overlaid on Smith and Sandwell (1994) topography. The current associated with the SAF, containing the large majority of the ACC transport at this longitude, flows from the west at about 49.5°S on the north side of the Southeast Indian Ridge. After the current crosses the 140°E fracture zone into deeper water its mean position tends toward the east-southeast (e.g., Gille, 1994) though it executes large meanders as predicted by McCartney (1976). The SAFDE array was oriented along a SSW-NNE line overlapping the WOCE SR3 repeat hydrography track that was designed to be perpendicular to the approximate mean axis of the SAF. Fig. 2 shows the locations of the horizontal electrometers (the middle row of symbols in Fig. 1) relative to the position of the SAF, as observed in March 1993, by S. Rintoul along the WOCE SR3 line.

At the centre of the array, 9 sub-surface, nearly full-depth moorings were deployed as a local dynamics array (LDA). Of these, 4 complete moorings and 3 partial moorings were recovered. Three of the complete moorings (indicated by circles that are overlaid by IES triangles in Fig. 1) were situated along the SSW-NNE SR3 track, and the last complete mooring was to the east. Fig. 3 displays the zonal current from the four current meter depths (300 m, 600 m, 1000 m and 2000 m) on the easternmost mooring (easternmost circle in Fig. 1). The high vertical coherence characteristic of currents at other locations along the ACC (e.g., Sciremammano et al., 1980; Bryden and Heath, 1985) is clearly evident here as well.

The three full moorings along SR3 are at the same locations as three moorings deployed by S. Rintoul from March 1993, through January 1995. This earlier experiment had a fourth mooring off to the west. Therefore, the combined

experiments have yielded compact arrays of four moorings at nearly identical locations for a duration of almost four years, with measurements of currents and temperatures at 4 depths (at least).

The three partial moorings recovered in March 1997, yielded 2000 m current and temperature records at the locations of the diamond and two small circles in Fig. 1, two to the west of the line of 3 full moorings and one to the east. Therefore, at the 2000 m level, there are 7 two-year records of currents and temperatures.

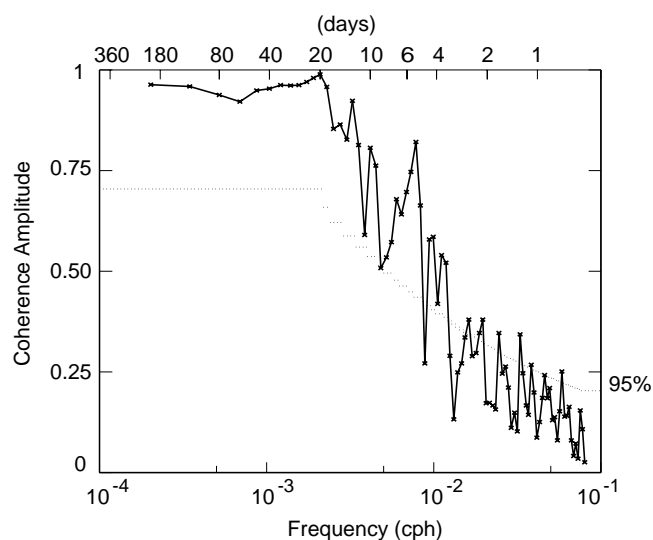


Figure 4. Coherence amplitude between zonal current measured at 2000 m by a moored current meter and conductivity-weighted, vertically-averaged zonal current measured by a horizontal electrometer near the mooring (both instruments are indicated by the diamond in Fig. 1). The 95% level of no significance is provided.

The most novel aspect of SAFDE was the deployment of a suite of horizontal electrometers (HEMs) and inverted echo sounders (IESs) to obtain time series of the vertically-averaged horizontal water velocity, of the temperature structure, and of the dynamic height structure. Seventeen electrometers were deployed with fifteen recovered, yielding 13 complete records at the locations shown in Fig. 1. The HEMs measure the horizontal electric fields (HEFs) which are theoretically related to the conductivity-weighted, vertically-averaged horizontal water velocity (Sanford, 1971; Chave and Luther, 1990). For those readers unfamiliar with the published empirical demonstrations of the relationship between HEFs and water velocity (e.g., Luther et al., 1991), Fig. 4 displays the coherence between zonal current from a 2000 m current meter and the HEF-derived vertically-averaged zonal current from a nearby HEM (the instruments are indicated by the diamond in Fig. 1). The coherence is high at periods longer than 4 days, and would be higher if the single current meter record could be replaced with vertically-averaged current measured by a full mooring. The high coherence in Fig. 4 is actually another demonstration of the high vertical coherence of fluctuations in the ACC. The low coherence at periods shorter than 4 days is due to the existence of strong electric fields generated in the ionosphere; see Luther et al., 1991, for a simple demonstration of the spectral structure of the ionospheric fields.

The conductivity weighting noted above means that the HEF is not a pure measure of vertically-averaged water velocity. Where both the vertical shear of the horizontal currents is large and the conductivity varies strongly with depth, as in the Gulf Stream for instance, the conductivity correction can be up to 25%. At mid- to high-latitudes, conductivity varies weakly with depth, resulting in a small

correction (Chave and Luther, 1990). In the SAF we expect the conductivity correction to be only a few percent. Even so, where the IES data are available the conductivity correction can be directly estimated and removed from the HEF measurement to yield vertically-averaged water velocity.

The IESs measure acoustic travel times from the seafloor to the surface and back. Watts and Rossby (1977) showed that variations in the travel times are dominated by the largest vertical scales (lowest baroclinic mode) of temperature perturbations. Where there is high vertical coherence of the temperature perturbations, irrespective of modal content, each travel time can define almost uniquely a particular profile of temperature. If, in addition, dynamic height variability is dominated by temperature fluctuations, each travel time can also define almost uniquely a particular profile of dynamic height. To make this analysis work there must be high vertical coherence of velocity and temperature fluctuations, a condition known to be met in the ACC as noted above, and there must be sufficient CTD data to fully map the range of measured travel times onto particular profiles of temperature or dynamic height, a condition met south of Tasmania due to the many repeat hydrographic sections conducted by S. Rintoul and collaborators over the past six years.

Of the eighteen IESs deployed in SAFDE, all were recovered and all yielded complete records. Where the IESs surround the HEMs, dynamic heights from the IESs will be used to get top-to-bottom shears that will be combined with vertically-averaged water velocities from the HEFs (after applying the IES-derived conductivity correction) to yield absolute profiles of water velocity as a function of time over a 225 km span of the SAF. These measurements will have many uses, such as providing sections of momentum and heat fluxes, providing information about frontal location and structure for proper analysis of the LDA mooring data, and validating the interpretation of satellite measurements of kinetic energy and momentum flux.

Two of the HEM-IES absolute velocity profile time series exist within the LDA, at locations where moorings were either lost or only partially recovered. Sub-sampling these profiles at the depths of the current meters on the 4 complete moorings of the LDA will produce a full two-dimensional array of six observation sites at 4 depths, thus permitting calculation of higher-order momentum, energy and vorticity equation terms that require estimation of horizontal gradients and divergences of fluxes, etc.

To demonstrate that the horizontal spacing within the array has yielded good horizontal coherence, a requirement for calculation of momentum budget terms, etc., Fig. 5 displays vertically-averaged water speeds derived from the five central HEMs (centred on the diamond in Fig. 1). Besides the obvious coherence, the data show remarkable variability, with speeds occasionally exceeding 30 cm/s. The IES records are even more coherent.

At low frequencies we expect to be able to use the entire HEM array from 48.7°S to 52.8°S to calculate the

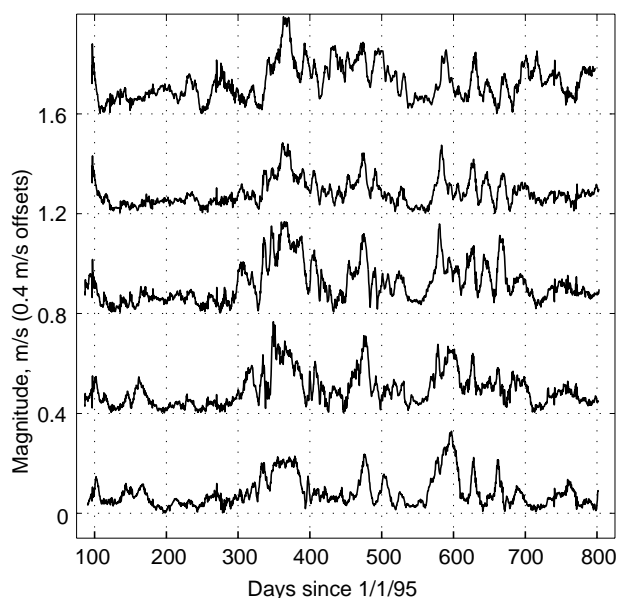


Figure 5. Conductivity-weighted, vertically-averaged horizontal water speed measured by the five HEMs nearest the centre of the SAFDE array (indicated by the 4 stars surrounding the diamond in Fig. 1).

total transport and its variability through this ~450 km section, despite the gaps due to lost data or instruments (Fig. 1). The relationship of this barotropic transport to the baroclinic transport observed along SR3, and the effect of the barotropic variability on property fluxes through this section will be examined.

## References

- Bryden, H. L., and R. A. Heath, 1985: Energetic eddies at the northern edge of the Antarctic Circumpolar Current in the Southwest Pacific. *Prog. Oceanogr.*, 14, 65–87.
- Chave, A. D., and D. S. Luther, 1990: Low-frequency, motionally induced electromagnetic fields in the ocean, 1, Theory. *J. Geophys. Res.*, 95, 7185–7200.
- Gille, S. T., 1994: Mean sea surface height of the Antarctic Circumpolar Current from Geosat data: Method and application. *J. Geophys. Res.*, 99, 18,255–18,273.
- Luther, D. S., J. H. Filloux, and A. D. Chave, 1991: Low-frequency, motionally induced electromagnetic fields in the ocean, 2, Electric field and Eulerian current comparison from BEMPEX. *J. Geophys. Res.*, 96, 12,797–12,814.
- McCartney, M. S., 1976: The interaction of zonal currents with topography with applications to the Southern Ocean. *Deep-Sea Res.*, 23, 413–427.
- Sanford, T. B., 1971: Motionally-induced electric and magnetic fields in the sea. *J. Geophys. Res.*, 76, 3476–3492.
- Sciremammano, F., Jr., R. D. Pillsbury, W. D. Nowlin, Jr., and T. Whitworth, III, 1980: Spatial scales of temperature and flow in Drake Passage. *J. Geophys. Res.*, 85, 4015–4028.
- Smith, W. H. F., and D. T. Sandwell, 1994: Bathymetric prediction from dense satellite altimetry and sparse shipboard bathymetry. *J. Geophys. Res.*, 99, 21803–21824.
- Watts, D. R., and H. T. Rossby, 1977: Measuring dynamic heights with inverted echo sounders: Results from MODE. *J. Phys. Oceanogr.*, 7, 345–358.
- Wells, N. C., and B. A. de Cuevas, 1995: Depth-integrated vorticity budget of the Southern Ocean from a General Circulation Model. *J. Phys. Oceanogr.*, 25, 2569–2582.
- Wilkin, J. L., and R. A. Morrow, 1994: Eddy kinetic energy and momentum flux in the Southern Ocean: Comparison of a global eddy-resolving model with altimeter, drifter, and current-meter data. *J. Geophys. Res.*, 99, 7903–7916.
- WOCE IPO, 1997: WOCE Data Guide 1997. WOCE Report No. 150/97, March 1997, Southampton, UK.

## WOCE Helps to Assess the Quality of Historical Hydrographic Data: A New Validated Data Set for the Southern Hemisphere

*Victor Gouretski and Kai Jancke, WHP Special Analysis Centre, Hamburg, Germany. gouretski@bsh.d400.de*



The WHP Special Analysis Centre in Hamburg was established to perform hydrographic data analysis and synthesis functions, including the generation of basin scale consistent data sets, which combine both WOCE and pre-WOCE data. As the analysis stage of WOCE is coming SAC continues its effort to arrive on a World Ocean climatology based on the WOCE data. Because of large spatial separation between the WOCE lines we use historical hydrography to produce a first-guess field for the objective interpolation of the WOCE data. High quality standards as set for the WOCE hydrographic programme have guaranteed a major advance in the observational hydrographic data base for the Global Ocean. For the first time a world-wide reference net to validate the quality of historical hydrographic data is provided.

### Data

SAC has prepared a new validated data set for the Southern Hemisphere including a total of 65,000 hydrographic stations (Fig. 1). Most of the data came from the World Ocean Atlas CD-ROM (1994). Southern Ocean Data Base of the Alfred Wegener Institut in Bremerhaven contributed with 332 profiles. The current version of the combined data set includes 893 stations from the WOCE lines in Pacific and we will include other WOCE data in the nearest future. We used only bottle and low-resolution CTD casts obtained over depths greater than 200 m with up to six parameters given at observed levels: temperature, salinity, oxygen, silicate, nitrate and phosphate.

### Validation method

Previous studies for the South Pacific (Gouretski and Jancke, 1996) revealed a very inhomogeneous quality of the historical hydrographic data often with large systematic offsets between the cruises. In validating the Southern Hemisphere data we use the experimental fact that relations between parameters in the deep ocean are locally relatively stable (Saunders, 1986). Here we validate the data by comparing individual observations with the statistics of the neutral density-parameter relationships of a local station ensemble. The size of the validation boxes was chosen to be in the latitude and longitude directions respectively and guaranteed typically about 50–150 stations for each local ensemble. In order to diminish the influence of data which are largely in error the original data have been ordered by cruise and the validation procedure was applied to the data three times each time rejecting profiles and cruises with percentages of rejected observations higher than a prescribed limit. Following percentages of the observations were rejected by our validation procedure: 15% for density (T or/and S rejected), 18% for oxygen, 24% for silicate, 36% for nitrate and 30% for phosphate.

### Objective interpolation

The validated data set was used as input for the objective interpolation algorithm. In a deviation from the World Ocean Atlas (WOA) climatology and following Lozier et al. (1995) we interpolate our data on density surfaces (we

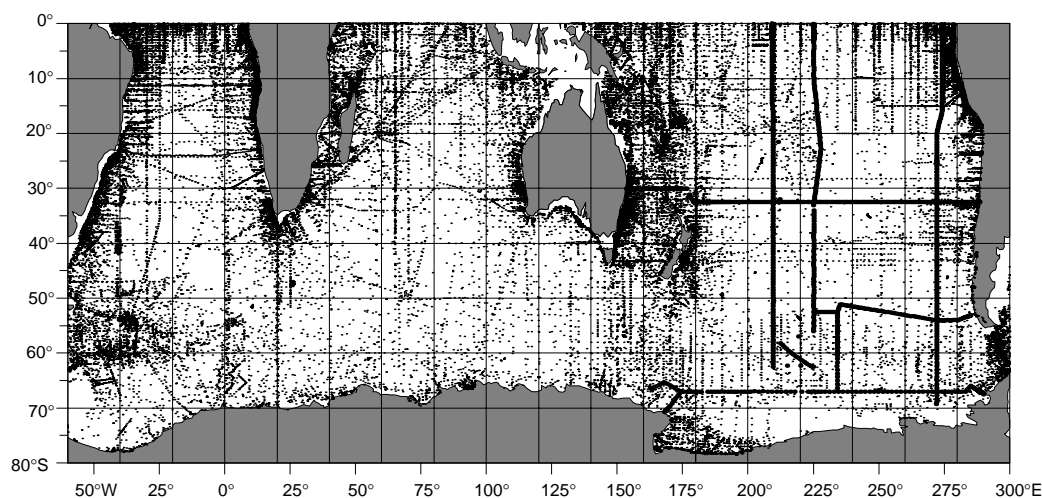


Figure 1. Locations of hydrographic stations used in this study. WOCE stations are shown with large dots.

used neutral density). This approach does not introduce artificial water masses and preserves relatively strong gradients even when a large decorrelation scale is used (we modelled spatial correlations by a gaussian function with a decorrelation scale of 500 km). For each grid point, an individual set of neutral surfaces was selected as determined by the mean vertical thermohaline structure at a grid point. The number of neutral surfaces was taken twice the number of standard depths to minimise errors during the interpolation from the neutral surfaces back to the standard depths. No additional smoothing was performed on the gridded data. Error bars can be estimated.

Fig. 2 shows property distribution maps for the neutral density surface  $\gamma_n = 28.00$ . This surface lies within the

upper part of the deep salinity maximum, which represents a warm and saline North Atlantic Deep water modified on its way from the South Atlantic. The salinity decreases from 34.74 at 50°E to 34.70 in the Drake Passage with a corresponding temperature drop from 2.1 to 1.8°C. Fig. 2 also gives the dynamic topography at 300 m referenced to a horizontal surface of no motion at 2000 m. Our climatology successfully resolves the quasi-zonal

Antarctic Circumpolar Current, cyclonic Weddell and Ross gyres to the south and anticyclonic gyres to the north. In a deviation from the WOA climatology it also resolves to a certain degree the Brazil, Agulhas and East Australian boundary currents. A more detailed comparison between the WOA and SAC climatology was made for the South Pacific. The main differences are mostly due to the erroneous or biased observations present in the WOA profile data set. Differences due to the isopycnal (SAC) and isobaric (WOA) methods of averaging are most prominent within the ACC and boundary currents. Our comparison also indicates, that zonal averages used as first-guess fields for the WOA objective analysis seem to introduce artificial local extrema in the data poor areas. The SAC Southern Hemisphere

Table 1. Offsets for the WOCE South Pacific cruises (See Fig. 3) (Offset standard deviations are given in parenthesis).

Cruise 1 SSW Batch	Cruise 2 SSW Batch	Cross-over point	Number of profile pairs	SSW diff.* $10^{-3}$	Parameter offsets: Cruise 2 – Cruise 1				
					Salinity	Oxygen [ml/l]	Silicate [	Nitrate mmol/kg	Phosphate ]
P17E-P19S P120	P19C P120	A	10	0.0	-0.0001 (0.0017)	-0.016 (0.027)	0.62 (1.30)	0.082 (0.212)	0.017 (0.013)
P6 P116	P19C P120	B	23	-2.3	0.0008 (0.0010)	-0.010 (0.017)	-1.44 (0.73)	-0.620 (0.166)	-0.061 (0.019)
S4 P108	P17E-P19S P120	C,D	26	-2.6	0.0033 (0.0004)	-0.039 (0.012)	0.88 (2.02)	0.372 (0.350)	0.006 (0.012)
P16A-P17A P120	P17E-P19S P120	E	15	0.0	0.0002 (0.0022)	-0.049 (0.043)	0.98 (1.21)	-0.310 (0.148)	0.060 (0.012)
P16S-P17S P108,P114	P6 P116	G,F	12	-0.3,-0.6	0.0027 (0.0019)	-0.004 (0.015)	-0.15 (0.62)	0.998 (0.189)	0.067 (0.023)
P16C P114	P16S-P17S P114	H	7	0.0	-0.0035 (0.0013)	0.012 (0.010)	0.94 (1.06)	-0.515 (0.229)	0.025 (0.016)
P17C P114	P16S-P17S P114	I	3	0.0	0.0001 (0.0009)	0.018 (0.031)	1.14 (1.96)	-0.555 (0.415)	-0.003 (0.041)
P16A-P17A P120	P16S-P17s P114	F	8	2.9	-0.0028 (0.0016)	-0.007 (0.020)	2.32 (1.70)	0.051 (0.244)	0.027 (0.024)

\*SSW batch differences according to Aoyama and Joyce (1996)



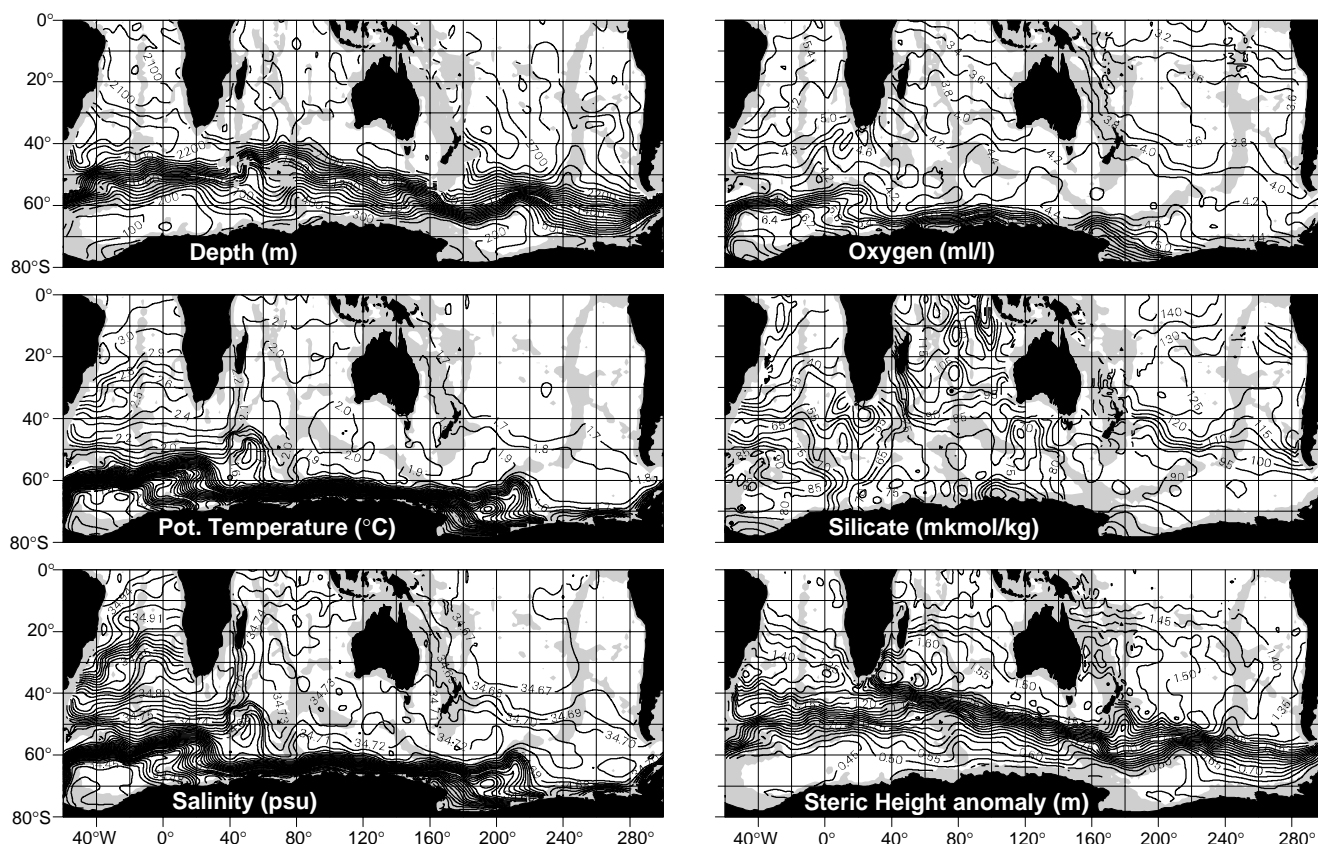


Figure 2. Property distribution on the neutral surface  $\gamma_n = 28.00$  and steric height anomaly for the layer 300–2000 metres.

gridded fields are available on the SAC WWW server.

### Inter-cruise offsets

An important step in assessing the quality of the historical data was to determine inter-cruise offsets. Two main assumptions are made: (1) deep water potential temperature-parameter relationships are stable, (2) errors in temperature measurements are negligible. The offset estimation is done by comparing locally individual profile observations with the reference (WOCE) data in the potential temperature-parameter space. Only observations below 1000 m and with temperature lower than 2.5°C are considered. Both conditions guarantee that the offsets are calculated within the most voluminous and stable water masses: Circumpolar Deep water and South Pacific Deep Water.

Our reference (WOCE) data subset consists of 8 cruises worked within a 5-year period 1991–1994 (Fig. 3). Systematic offsets were reported for some WOCE cruises earlier by Aoyama and Joyce (1996). We determined offsets between the WOCE cruises at nine intersection points and adjusted WOCE data (arbitrarily) to the data from the meridional line P19C. A high degree of consistency of the WOCE data is demonstrated by Table 1. Inter-cruise offsets are significantly bigger than measurement accuracies required by WOCE in four cases for salinity (S4 vs P17E–P19S and P16S–P17S vs P6, P16C and P16A–P17A correspondingly) and in four cases for nitrates (P6 vs P17E–P19S, P16S–P17S vs P6, P16C and P17C correspondingly).

The causes for the offsets were not investigated in this study. We note here that differences in the Standard Sea Water batches may result in systematic salinity offsets of the order (Aoyama and Joyce, 1996). In three cases (P17E–P19S vs P19C, P16A–P17A vs P17E–P19S and P17C vs

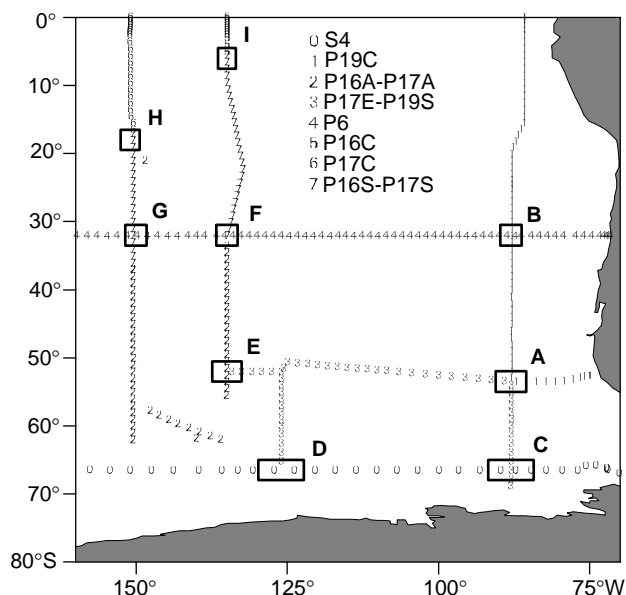


Figure 3. Locations of the WOCE South Pacific hydrographic sections and crossover points where the inter-cruise offsets were determined (for clarity not all stations are shown).

P16S–P17S) the same batches were used and inter-cruise salinity differences are small and insignificant. In three cases (S4 vs P17E–P19S, P16S–P17S vs P6 and P16A–P17A vs P16S–P17S) the inter-cruise differences decrease, when correcting for SSW differences. Correction for the SSW batch difference would change the salinity offset P6 vs P19C from 0.0008 to 0.0015, with the magnitude still

within the accuracy requirement. In one case a relatively high salinity difference (–0.0035) between P16C and P16S–P17S can not be explained from the SSW batch difference.

The adjusted WOCE data were used as a reference to infer offsets for the historical cruises in the South Pacific. Table 2 gives offsets for two parameters, nitrates and phosphates. The number of cruises available does not

Table 2. Phosphate and nitrate inter-cruise offsets (mkmol/kg) of historical South Pacific cruises relative to the WOCE data.

Ship		Country	Date	Offsets:			
				Phosphates		Nitrates	
				Mean	St_err	Mean	St_err
1	Carnegie	USA	290206–290330	-0.69	0.07	-	
2	Burton Island	USA	600129–600415	-0.56	0.08	-	
3	Gascoyne	Australia	600318–600418	-0.55	0.04	-	
4	Gascoyne	Australia	650204–650402	-0.45	0.03	-	
5	Gascoyne	Australia	651030–651127	-0.42	0.02	-	
6	Professor Zubov	USSR	860113–860127	-0.36	0.02	-	
7	Gascoyne	Australia	640803–640811	-0.32	0.02	-	
8	Gascoyne	Australia	640113–640205	-0.31	0.01	-	
9	Professor Zubov	USSR	860211–860224	-0.29	0.02	-	
10	Discovery II	UK	360128–360215	-0.28	0.11	-	
11	Eltanin	USA	631013–631129	-0.28	0.09	1.28	1.14
12	Hakuho-Maru	Japan	681205–690201	-0.24	0.13	1.87	0.53
13	Discovery II	UK	301123–310114	-0.20	0.07	-	
14	Coriolis	France	641222–650127	-0.17	0.04	-2.88	0.29
15	Horizon	USA	600929–601203	-0.16	0.12	2.70	1.32
16	Discovery II	UK	501005–501128	-0.15	0.03	-	
17	Eltanin	USA	650714–650824	-0.13	0.03	0.20	0.68
18	Eltanin	USA	661003–661031	-0.11	0.04	-0.61	0.42
19	Eltanin	USA	641011–641122	-0.11	0.04	-0.23	0.27
20	Eltanin	USA	640802–640908	-0.10	0.02	-0.03	0.13
21	Eltanin	USA	650923–651107	-0.06	0.02	0.97	0.71
22	Eltanin	USA	631228–640201	-0.06	0.02	-0.66	0.79
23	Professor Vizeze	USSR	851223–860212	-0.05	0.02	-	
24	Melville	USA	731222–740526	-0.04	0.01	1.32	0.16
25	Unknown	Australia	820918–821027	-0.04	0.01	-	
26	Eltanin	USA	650325–650430	-0.03	0.02	-0.20	0.11
27	T. Washington	USA	710113–710214	-0.02	0.00	2.81	0.05
28	Northwind	USA	720203–720220	-0.02	0.01	0.41	0.08
29	Hudson	Canada	700427–700520	-0.01	0.03	2.57	0.56
30	Eltanin	USA	640519–640629	0.00	0.02	-0.12	0.15
31	Ob	USSR	580311–580613	0.00	0.04	-	
32	Eltanin	USA	670312–670515	0.03	0.02	0.79	0.19
33	Eltanin	USA	651207–660105	0.04	0.04	-6.39	2.84
34	T. Washington	USA	690121–690410	0.04	0.02	2.24	0.15
35	T. G. Thompson	USA	760201–760405	0.07	0.01	-	
36	Hakuho-Maru	Japan	711207–720212	0.10	0.02	0.23	0.11
37	Melville	USA	750221–750330	0.13	0.01	-	
38	Capitan Canepa	Argentina	590806–590823	0.13	0.04	-	
39	Islas Orcadas	Argentina	750118–750222	0.13	0.02	-	
40	Unknown	Australia	780721–780816	0.14	0.02	-	
41	Yaquina	USA	711017–711202	0.15	0.06	0.51	0.23
42	Eltanin	USA	670604–670731	0.21	0.02	0.35	0.18
43	Hudson	Canada	700131–700214	0.26	0.09	-0.66	0.79
44	Discovery II	UK	331214–340129	0.27	0.03	-	
45	Discovery II	UK	320901–321003	0.31	0.05	-	
46	Discovery II	UK	510522–510627	0.34	0.02	-	
47	Discovery II	UK	380114–380314	0.36	0.01	-	
48	Discovery II	UK	341027–341117	0.45	0.01	-	
49	Capitan Canepa	Argentina	580318–580407	0.53	0.11	-	
50	Discovery II	UK	340223–340315	0.65	0.03	-	
51	Dana	Denmark	280918–281218	-	-	-2.39	1.81

seem sufficient to reliably infer any time trends in the offset distributions, since usually no independent measurements (obtained by another ship in the same geographical locale and during the same time period) are available. In general, high scattering of the individual profile offsets indicates a low data quality. According to Table 2 some cruises have nutrient offsets large enough to seriously distort climatological nutrient distributions. Silicate distribution (Fig. 2) is more patchy in the Atlantic and Indian Oceans compared to the South Pacific and is explained by inter-cruise offsets which have not yet been determined for those two basins. We expect to continue this work in the South Atlantic and Indian Ocean as the WOCE data becomes available to us.

## Estimates of Diapycnal Mixing Using LADCP and CTD Data from I8S

Kurt L. Polzin, Woods Hole Oceanographic Institute, USA and Eric Firing, School of Ocean and Earth Sciences and Technology, University of Hawaii, USA  
kpolzin@whoi.edu

Recent fine- and microstructure measurements in the South Atlantic show that the abyssal ocean supports an enhanced internal wavefield and heightened turbulent mixing above rough topography (Polzin et al., 1997). In contrast, internal waves are at background levels and mixing is weak above smooth topography. The enhanced mixing noted above rough topography appears to be sufficient to close the abyssal heat budget of the Brazil Basin. While it is tempting to argue that one can diagnose the level of mixing from bathymetric roughness, it is too soon to generalise from such limited measurements about how the abyssal heat budget of the world ocean may be closed. A more general survey to examine the issue of elevated mixing in the abyssal ocean is called for.

Numerous full-water-depth lowered ADCP (LADCP) profiles of relative velocity have been collected coincident with CTD profiles along WOCE hydrographic lines. The velocity profiles, in principle, resolve oceanic currents having vertical wavelengths from full water depth down to about 50 m. These data afford the opportunity to investigate the spatial characteristics of the finescale internal wavefield. Application of finescale parameterisations to the LADCP and CTD data permit corresponding estimates of the turbulent dissipation rate ( $\epsilon$ ) and diapycnal eddy diffusivity ( $K_p$ ) (Henyey et al., 1986; Gregg, 1989; Polzin et al., 1995) resulting from internal wave breaking.

The rationale for applying finescale parameterisations to LADCP data is that the WOCE data set affords greater coverage of the world ocean than has been (or likely will be) obtained using dedicated fine- and microstructure instruments. Topographic variability, barotropic tidal flows and mesoscale eddy velocities are expected to be important variables in determining the energy and characteristics of the abyssal internal wavefield and, in turn, the intensity of turbulent mixing in the abyssal ocean. Lowered ADCP data

## References

- Aoyama, M., and T. Joyce, 1996: WHP property comparisons from crossing lines in North Pacific. In: 1996 WOCE Pacific Workshop. Abstracts, p.1, Newport Beach, CA (unpublished manuscript).
- Gouretski, V.V., and K. Jancke, 1996: A new hydrographic data set for the South Pacific: synthesis of WOCE and historical data. WOCE Report No. 143/96 (unpublished manuscript).
- Lozier, M. S., W. B. Owens and R. Curry, 1995: The Climatology of the North Atlantic. *Progr. Oceanogr.*, 36, p.1–44.
- Olbers, D., V. V. Gouretski, G. Seiß, and J. Schröter, 1992: Hydrographic Atlas of the Southern Ocean. AWI, Bremerhaven.
- Saunders P.M., 1986: The accuracy of measurements of salinity, oxygen and temperature in the deep ocean. *Journal of Physical Oceanography*, 16, p.189–195.
- World Ocean Atlas CD-ROM (1996) NOAA, Washington, DC.



have sampled abyssal waters over a wide variety of topographic and flow regimes. A global finescale internal wave survey and parameterisation study utilising the LADCP data would give great insight into which geographic/oceanographic regimes are the most important. We present below a preliminary estimate of diapycnal mixing along I8S, which crosses the Antarctic Circumpolar Current (ACC) in region of particularly strong eddy energy and topographic influence.

## Finescale parameterisation

Internal waves interact with each other and, on average, result in the transport of energy to smaller spatial scales. The intent of a finescale parameterisation is to estimate this average energy flux in terms of the properties of the finescale internal wavefield, where finescale denotes vertical wavelengths of 10's to 100's of metres. The resulting energy flux to smaller scales is equated with the rate of dissipation of turbulent kinetic energy,  $\epsilon$ . One such parameterisation is given by:

$$\epsilon = \epsilon_0 \frac{f}{f_0} \frac{N^2}{N_0^2} E^2. \quad (1)$$

where  $\epsilon_0 = 7.8 \times 10^{10} \text{ W / kg}$ ,  $f$  is the Coriolis parameter,  $f_0$  corresponds to  $30^\circ$  latitude,  $N$  is the buoyancy frequency with  $N_0 = 3 \text{ cph}$ , and  $E$  is the average shear spectral density (normalised to the GM76 [Garrett and Munk, 1975, as modified by Cairns and Williams, 1976] model, i.e.  $E = 1$  for GM) for vertical wavenumbers ( $m$ ) smaller than a cut-off value,  $m_c$ , defined as

$$\int_0^{m_c} S_z dm = 0.7 N^2 \quad (2)$$



with  $S_z$  the vertical wavenumber shear spectral density. The diapycnal diffusivity is given by

$$K_p = \Gamma \frac{\varepsilon}{N^2} = 0.07 \times 10^{-4} \frac{f}{f_0} E^2 \text{ m}^2 \text{ s}^{-1}, \quad (2)$$

where the mixing efficiency  $G = 0.25$ .

Equations (1) and (3) are simplified versions of a parameterisation presented in Polzin et al. (1995), which accurately predicts the dissipation rate to within a factor of  $\pm 2$  for both GM and non-GM internal wavefields. The nature of the simplification is that the frequency content of the internal wavefield has been assumed to be adequately represented by the GM model. As a result, diffusivity results presented below may be biased high by as much as a factor of three if the wavefield is more inertial than GM due to wave/mean flow interactions producing critical layers.

Note also that the LADCP does not, in general, resolve the bandwidth of vertical wavenumber space ( $0 < m < m_c$ ) required by the parameterisation. The cut-off value  $m_c$  corresponds to 10 metre vertical wavelengths for the GM spectrum. Wavelengths greater than 100 m appear to be unaffected by the spatial averaging inherent in the LADCP system while motions having wavelengths smaller than 50 m are damped and noise begins to dominate. In addition, there are possible errors induced by the beam separation for vertical wavelengths smaller than 100 m. We are currently conducting an intercomparison study between LADCP and expendable current profiler (XCP) velocity profiles in order to define the transfer function and noise characteristics of the LADCP. In this preliminary study, the spectral level parameter in the model ( $E$ ) was estimated by comparing the average spectral density at vertical wavelengths larger than 100 m with the spectral density in the GM76 model. While this methodology is clearly an approximation given the above description of  $E$ , the large values of  $K_p$  inferred below result from large spectral levels which in turn imply relatively large cut-off wavelengths ( $1/m_c > 50 \text{ m}$ ). As the observed spectra are typically white, we believe the resulting uncertainty in large diffusivity estimates ( $K_p > 1 \times 10^{-4} \text{ m}^2 \text{ s}^{-1}$ ) for any given depth bin to be  $\pm$  a factor of three with a possible bias of a factor of three.

## Results

Preliminary estimates of diapycnal diffusivity (3) were made using LADCP and CTD data from the I8S section. That section extends from 30°S, 90°E on the Broken Plateau to 64°S, 82°E south of the Kerguelen Plateau, fig. 1. Two groups of 12 profiles centred about 35° and 55°S were examined. The 35°S stations are within the subtropical gyre of the Indian Ocean and the 55°S stations are poleward of the Antarctic Polar Front. The northernmost profile of the first group and the southernmost profile of the second are adjacent to, but not on the sloping flanks of ridges which rise above 1500 m depth.

At 35°S the shear spectra are within a factor of two of

GM levels to 3000 m and exhibit significant enhancement at depth. The model estimate of the vertical diffusivity is less than  $0.2 \times 10^{-4} \text{ m}^2 \text{ s}^{-1}$  for depths shallower than 3000 m, fig. 2, and approaches  $1 \times 10^{-4} \text{ m}^2 \text{ s}^{-1}$  at the bottom. The results from 55°S, while not unanticipated, are quite remarkable, fig. 2. Below 1000 m, the average vertical diffusivity is  $4.4 \times 10^{-4} \text{ m}^2 \text{ s}^{-1}$ , forty times larger than the estimate for a GM wavefield. The enhancement decays towards GM levels above 1000 m. The enhanced diffusivity corresponds to a factor of 5–7 enhancement of the shear spectral levels above the GM model. Depth-integrated dissipation rates are 4.6 and  $0.95 \text{ m W / m}^2$  for 55° and 35°S, respectively. The corresponding value for the GM wavefield is  $0.8 \text{ m W / m}^2$ .

## Discussion

We believe the inference of large depth-averaged diffusivities within the ACC to be robust for the following reasons. First, there was an obvious signature of vertical phase propagation in the depth range 1600–3850 m: the

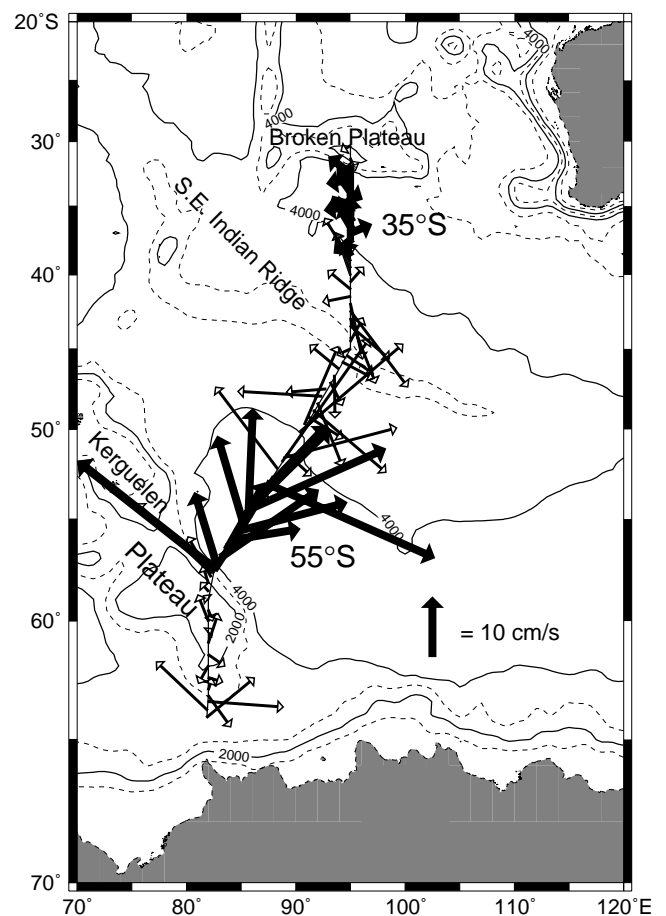


Figure 1. Bathymetry and depth-averaged current vectors along the I8S section line. The analysis focuses upon two groups of 12 profiles, one centred about 35°S and the other centred about 55°S. These stations are denoted with bold current vectors. The bathymetric contour interval is 1000 m, with solid contours every 2000 m.



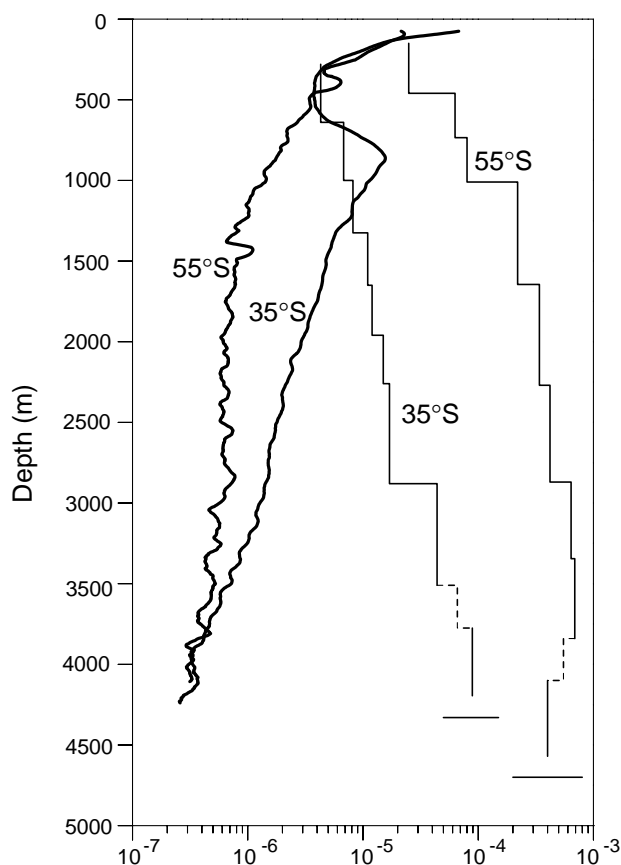


Figure 2. Vertical profiles of  $N^2$  ( $s^{-2}$ ) (thick lines) and  $K_p$  ( $m^2/s$ ) (thin lines) for two groups of twelve stations, one at  $35^\circ S$  and the other at  $55^\circ S$ . The dashed lines represent regions where no data are available; the model diffusivity estimate has been interpolated through these regions. Similarly, no data are available in the bottom-most 130 m of each profile. The horizontal lines at the bottom of the diffusivity profiles represent the average bottom depth in each case. Shear spectra for the two groups were computed using a transform interval, and averaged over depth bins of 320 or 640 m.

clockwise spectra were on average a factor of three larger than the counter-clockwise spectra. Clockwise phase rotation with depth of the velocity (or shear) vector implies upward energy propagation in the southern hemisphere. This signature implies the parameterisation estimates are not dominated by noise. Secondly, although the diffusivity may be on average 40 times the GM value, estimates of the depth-integrated dissipation rate differ by only a factor of 5 between  $35^\circ S$  and  $55^\circ S$ . The similarity in the depth-integrated dissipation rate and disparity in depth-averaged diffusivity are associated with the low depth-averaged  $N^2$  in the Southern Ocean. Since the depth-averaged dissipation is equal to the energy flux into the internal wavefield in a one-dimensional (vertical) balance, the heightened diffusivities inferred at  $55^\circ S$  do not imply unreasonably large energy sources to maintain the wavefield. Third, the vertical profile of vertical diffusivity corresponds quite well with that inferred by Olbers (1989) from an inverse model of the

ACC based upon the Gordon atlas.

The data suggest a much stronger bottom boundary source of internal wave energy at  $55^\circ S$  than at  $35^\circ S$ . In general, both internal tide and internal lee-wave generation (Bell, 1975) represent possible additional energy sources for the small-scale internal wavefield. The barotropic tidal flows which one can infer from Kantha (1995) do not appear to vary significantly between  $35^\circ$  and  $55^\circ S$  and thus the signal of enhanced mixing inferred at  $55^\circ S$  is not likely to be associated with the generation of an internal tide having small vertical scales, as appears to be the case in the Brazil Basin (Polzin et al., 1997). Also, the small-scale bottom topography (Smith and Sandwell 1994), which is the proximate cause of enhanced mixing in the eastern portion of the Brazil Basin, does not appear to differ significantly between  $35^\circ$  and  $55^\circ S$ . The big differences between these latitudes are the stratification (Fig. 2) and the currents (Fig. 1). The ACC and associated mesoscale eddies near  $55^\circ S$  have strong deep velocities. Depth-averaging the LADCP profiles from 3000 m to the bottom and then calculating the rms speed for each of the two profile groups used in this study, we find 18.7 cm/s at  $55^\circ S$  compared to only 3.6 cm/s at  $35^\circ S$ . Our leading candidate to explain the enhanced small-scale shear field and turbulent mixing inferred from the model at  $55^\circ S$  is the generation of internal lee-waves as the mesoscale currents flow over small horizontal scale bottom topography.

If lee-wave processes are responsible for the heightened dissipations and diapycnal diffusivities at  $55^\circ S$ , the role of internal waves needs to be considered in the dynamics and energetics of the ACC. Depth-integrated dissipation rates associated with lee-wave generation at the bottom boundary (Bell, 1975) are typically an order of magnitude greater than that produced by boundary layer stresses ( $\rho C_D U^3$  with  $C_D = 3 \times 10^{-3}$ ). This implies that, if there is significant small-scale topographic roughness, the energy within the mesoscale eddy field is dissipated by internal wave generation rather than in Ekman layers. To the degree that the eddy energy associated with baroclinic instability of the Circumpolar Current is dissipated by lee wave generation, it stands to reason that the net downward flux of eastward momentum appears as a net upward flux of eastward momentum within the internal lee-wave field, and the dissipation of these internal waves in the interior of the fluid implies significant stress divergences at mid-depth. In an Ekman type balance, these stress divergences would support a weak ageostrophic poleward flow having a large vertical scale. Defining the strength of such a circulation begs the question of how large the net downward flux of eastward momentum associated with baroclinic instability is in relation to the zonal wind stress. In addition, a significant fraction of the meridional buoyancy flux associated with baroclinic instability may occur by diapycnal processes within the stratified interior as opposed to being accomplished via air-sea interactions (Tandon and Garrett, 1996). Finally, we wish to strike a cautionary note: the mesoscale eddy field exhibits a great deal of variability along the path of the ACC and it is not clear at this time

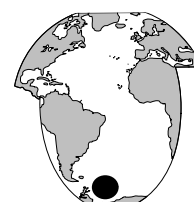
whether the 55°S diffusivity profile in Fig. 2 is representative of the zonal average at that latitude.

## References

- Bell, T. H., 1975: Topographically-generated internal waves in the open ocean. *J. Geophys. Res.*, 80, 320–327.
- Cairns, J. L., and G. O. Williams, 1976: Internal wave observations from a midwater float, 2. *J. Geophys. Res.*, 81, 1943–1950.
- Garrett, C. J. R., and W. H. Munk, 1975: Space-time scales of internal waves: A progress report. *J. Geophys. Res.*, 80, 291–297.
- Gregg, M. C., 1989: Scaling turbulent dissipation in the thermocline. *J. Geophys. Res.*, 94, 9686–9698.
- Henye, F. S., J. Wright, and S. M. Flate, 1986: Energy and action flow through the internal wavefield: An eikonal approach. *J. Geophys. Res.*, 91, 8487–8495.
- Kantha, L. H., 1995: Barotropic tides in the global oceans from a nonlinear tidal model assimilating altimetric tides, 1. Model description and results. *J. Geophys. Res.*, 100, 25283–25308.
- Smith, W. H. F., and D. T. Sandwell, Bathymetric prediction from dense altimetry and sparse shipboard bathymetry. *J. Geophys. Res.*, 99, 21803–21824, 1994.
- Olbers, D., 1989: Diffusion parameterizations for the climatological circulation of the North Atlantic and the Southern Ocean. Parameterization of Small-Scale Processes, Proc. 'Aha Huliko' a Hawaiian Winter Workshop, Hawaiian Institute of Geophysics, 181–204.
- Polzin, K. L., J. M. Toole, and R. W. Schmitt, 1995: Finescale parameterizations of turbulent dissipation. *J. Phys. Oceanogr.*, 25, 306–328.
- Polzin, K. L., J. M. Toole, J. R. Ledwell, and R. W. Schmitt, 1997: Spatial variability of turbulent mixing in the abyssal ocean. *Science*, 276, 93–96.
- Tandon, A. and C. Garrett, 1996: On a recent parameterization of mesoscale eddies. *J. Phys. Oceanogr.*, 26, 406–411.

## Norwegian Physical Oceanographic Activities in the Weddell Sea

*Ole Anders Nøst, Norwegian Polar Institute, Tromsø, Norway. ole@tromso.npolar.no*



The Norwegian oceanographic activities in the Weddell Sea have focused on the southern Weddell Sea continental shelf for the past 20 years. Some results from this work are published by Foldvik and Gammelsrød (1988), Gammelsrød et al., 1994, and Nøst and Foldvik (1994). This focus will now be changed as the Norwegian Research Council has developed a revised science-plan for Antarctic research. The oceanographic research under this revised science-plan will concentrate on the area from the coastal zone along Dronning Maud Land and northwards across the Weddell Gyre. The Dronning Maud Land area is the sector between 20°W and 45°E (see Fig. 1). Projects in the southern shelf regions may also be supported, however, during the period from 1997 to 2002 there will be no Norwegian oceanographic cruises into the southernmost regions.

The revised science-plan for Antarctic research gives us the opportunity to study the shelf/deep ocean system of the Weddell Sea as a whole. Projects which have already started that fit into the revised science-plan deal with shelf and slope processes and interaction between ice shelves and ocean along the Dronning Maud Land coast, and a project studying the properties of the Weddell Gyre surface mixed layer. We are conducting combined observational and modelling studies and one of our future goals is to develop a coastal zone model for the Weddell Sea.

This letter briefly outlines recent and ongoing Norwegian programmes in the Weddell Sea, and describes the future plans for the research under the revised science-plan. Fig. 1 shows the locations mentioned in the text.

### Recent and ongoing work

Nøst and Østerhus (in press) analysed CTD data from along the Filchner Ronne Ice Front covering the period from 1980

to 1993. It is known from the work of Markus (1996) that the grounded icebergs have changed the sea ice conditions in front of the Filchner Ice Shelf as the icebergs act as a barrier to the westward sea ice drift. This has resulted in increased sea ice concentrations and decreased sea ice production near the Filchner Ice Shelf. Nøst and Østerhus (in press) have shown that this change in sea ice production with a subsequent decrease in brine release to the ocean has resulted in cooler and fresher water masses in the Filchner Depression. This freshening and cooling is most probably caused by a cessation of the drainage of High Salinity Shelf Water (HSSW) from the Berkner Shelf into the Filchner Depression caused by the effects of the icebergs.

Haugan (submitted) has investigated the effect of sea ice production on the barotropic circulation. In areas of steady sea ice formation the sea ice is continuously removed, as in a coastal polynya where the sea ice is removed by the wind. This mechanism removes mass from the area and in a quasigeostrophic model the effect of this will be similar to the effect of an Ekman pumping term, as it will result in a vertical velocity at the surface which equals the sea ice production rate. Haugan found that the sea ice production in the southern Weddell Sea is comparable to the Ekman pumping in the same region. Most coupled sea ice ocean models ignore the exchange of mass between the sea ice cover and the ocean.

Østerhus and Orheim (1994) collected oceanographic measurements close to the grounding line beneath the Fimbul Ice Shelf. Time series of temperature, salinity and currents were obtained for periods of 2 to 16 months. The measuring site is located about 150 km from the ice shelf front, however, warm events lasting a few days were observed indicating an active exchange with the open ocean.

Østerhus is also participating in a project in col-

laboration with the British Antarctic Survey and Alfred Wegener Institute where the goal is to drill through the Filchner Ronne Ice Shelf and collect oceanographic measurements from beneath the ice shelf.

The research under the revised science-plan got off to a flying start in the 1996/97 field season when very heavy ice conditions allowed no access into the southern shelf regions. Preliminary results from a high resolution CTD survey and modelling of the coastal current at the coast between 15° and 20°W show that the onshore Ekman transport is important in forming the coastal current (see Fig. 2, page 24). This result was also obtained by Sverdrup (1953). Fig. 2b shows model results using the S-Coordinate Rutgers University Model version 3.0 (SCRUM 3.0).

The model set-up has periodic boundary conditions and only 4 gridpoints along shore. This allows no variations along shore and the across-shelf transport is mostly due to surface and bottom Ekman transport. As can be seen in Fig. 2 the model and observations have several discrepancies. By varying the wind field according to climatological data as well as adding tides to provide more mixing energy, several experiments will be done with the 2-D model before extending to a 3-D model. Hopefully, this will lead to increased understanding of the dynamics of the Antarctic Coastal Current.

In the 1997/98 field season we are participating in a Swedish cruise to the Weddell Sea. The plan for this cruise is to study the surface mixed layer in the Weddell Gyre along the Greenwich meridian from the coast to the polar front. As the coastal current water masses seem to be formed by surface water downwelling at the coast, the formation of the surface water is probably an important first step in the process of forming shelf waters.

## Plans for future activities

In the activities under the revised science plan we will mostly study processes on the shelf and continental slope and ice shelf-ocean interaction. In these problems we have experience to build upon and there is also a large amount of historical data from the shelf regions collected during earlier Norwegian expeditions.

We wish to understand the process of Low Salinity Shelf Water (LSSW) formation along the Dronning Maud Land coast as well as the dynamics of the coastal current which transport the LSSW into the southern Weddell Sea. In addition, we wish to understand the mechanisms for bringing Warm Deep Water into contact with the base of the ice shelves, as this is important for glacial melting. To

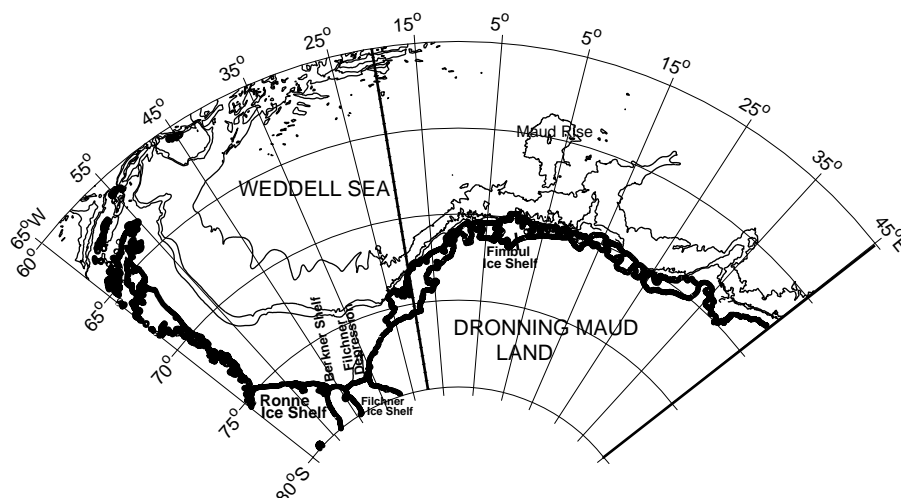


*Figure 1. Map of the Weddell Sea (contours from GEBCO 97). The hatched lines along the 20°W and 45°E meridians mark the borders of the Dronning Maud Line sector. Norwegian oceanographic research will concentrate on activities within this sector.*

do this, we must plan field experiments on the shelf and slope regions, as well as continue the sub-ice shelf measurements done by Østerhus and Orheim (1994). In addition we must develop suitable models that can deal with shelf and slope processes, sub-ice shelf processes and processes at the boundary between open ocean and ice shelf cavities. The ongoing modelling and observations of the coastal current, the observations done by Østerhus and Orheim (1994), and the 1997/98 cruise are a start towards the goal of understanding the coastal zone processes along Dronning Maud Land.

## References

- Foldvik, A., and T. Gammelsrød, 1988: Notes on Southern Ocean Hydrography, sea-ice and bottom water formation. *Palaeogeogr., Palaeoclimatol., Palaeoecol.*, 67, 3–17.
- Gammelsrød, T., A. Foldvik, O. A. Nøst, Ø. Skagseth, L. G. Anderson, E. Fogelquist, K. Olsson, T. Tanhua, E. P. Jones, and S. Østerhus, 1994: Distribution of water masses on the continental shelf in the southern Weddell Sea, in "The polar oceans and their role in shaping the global environment". AGU Geophysical Monograph 84.
- Haugan, P., submitted: Effects of sea ice freezing on ocean circulation in the Weddell Sea. Notes and Correspondence. *J. Phys. Oceanogr.*
- Nøst, O. A., and A. Foldvik, 1994: A model of ice shelf-ocean interaction with application to the Filchner-Ronne and the Ross Ice shelves. *J. Geophys. Res.*, 99, 14243–14254.
- Nøst, O. A., and S. Østerhus, in press: Impact of grounded icebergs on the hydrographic conditions near the Filchner Ice Shelf, Antarctica. Antarctic Research Series, S. Jacobs, ed.
- Markus, T., 1996: The effect of the grounded tabular icebergs in front of the Berkner Island on the Weddell Sea ice drift as seen from satellite passive microwave sensors, *IGARSS'96*, 1791–1793.
- Sverdrup, H. U., 1953: The currents off the coast of Queen Maud Land. *Nor. Geogr. Tidsskr.*, 14, 139–249.
- Østerhus, S., and O. Orheim, 1994: Oceanographic and glaciologic investigations through Jutulgryta, Fimbulisen, in the 1991/92 season. *Norsk Polarinstitutt Meddelelser No. 124*, 21–28.



## Note on Copyright

Permission to use any scientific material (text as well as figures) published in the International WOCE Newsletter should be obtained from the authors.

WOCE is a component of the World Climate Research Programme (WCRP), which was established by WMO and ICSU, and is carried out in association with IOC and SCOR. The scientific planning and development of WOCE is under the guidance of the Scientific Steering Group for WOCE, assisted by the WOCE International Project Office.

The International WOCE Newsletter is edited by Roberta Boscolo (roberta.boscolo@soc.soton.ac.uk) at the WOCE IPO at Southampton Oceanography Centre, Empress Dock, Southampton, SO14 3ZH, UK, Tel: 44-1703-596789, Fax: 44-1703-596204, e-mail: woceipo@soc.soton.ac.uk,

<http://www.soc.soton.ac.uk/OTHERS/woceipo/ip.html>

We hope that colleagues will see this Newsletter as a means of reporting work in progress related to the Goals of WOCE as described in the Scientific Plan.

The editor will be pleased to send copies of the Newsletter to institutes and research scientists with an interest in WOCE or related research.